Magnetic anisotropy and magnetic after-effect in ferromagnetic strained $LaCoO_3$ thin films

Zur Erlangung des akademischen Grades eines
DOKTORS DER NATURWISSENSCHAFTEN
von der Fakultät für Physik der Universität (TH)
Karlsruhe

genehmigte

DISSERTATION

von

Erhan Arac (M.Sc.)
aus Samsun (Türkei)

Tag der mündlichen Prüfung: 6. November 2009
Hauptberichter: Prof. Dr. H.v. Löhneysen
Mitberichter: Prof. Dr. W. Wulfhekel

Abstract

This thesis is dedicated to the study of the magnetic properties of epitaxial $LaCoO_3$ (LCO) thin films, such as the magnetic anisotropy and the time dependence of the magnetization, where the magnetic moment and ferromagnetic order are induced by epitaxial strain. To this purpose, the magnitude of the epitaxial strain was varied by the growth of thin films on (001) oriented $SrLaAlO_4$ (SLAO), $SrLaGaO_4$ (SLGO), $(LaAlO_3)_{0.3}(Sr_2AlTaO_6)_{0.7}$ (LSAT) and $SrTiO_3$ (STO) single crystal substrates by pulsed laser deposition (PLD) while the orientation of the strain was changed by the growth on (001), (110) and (111) oriented LSAT substrates. A new home-made magneto-optical Kerr effect (MOKE) and Kerr microscope measuring system for magnetization measurements in a temperature range from 4.2 K to 500 K was designed and realized including the necessary control and measuring software.

The Curie temperature, T_c, and the effective magnetic moment, μ_{eff}, increases with increasing lattice parameter, a, and mean lattice parameter, $< a >$, respectively. Furthermore, a coupling between the coercive field, H_c, and the strain state was extracted. Films with the lower epitaxial strain (LCO/SLGO and LCO/SLAO) exhibited significantly larger H_c with respect to the more heavily strained films (LCO/LSAT and LCO/STO). The remnant magnetization of the films was found to increase with increasing strain.

The magnetic anisotropy of strained (001), (110), and (111) oriented LCO films were investigated by MOKE, superconducting quantum interference device (SQUID) and cantilever torque magnetometry. The magnetocrystalline and magnetoelastic anisotropy constants $K_1 \approx$-1.2x10^4 erg/cm^3, $B_1 \approx$-8.7x10^7 erg/cm^3 and $B_2 \approx$4.3x10^7 erg/cm^3 were determined. The weak biaxial in-plane anisotropy with $< 110 >$ easy axis was observed for (001) oriented films, and explained by means of a small magnetocrystalline anisotropy ($K_1 < 0$). On the other hand, a strong anisotropy between the film plane and the c axis direction was observed in (001) oriented films. This was attributed to the large B_1 favoring in-plane magnetization due to its negative sign. The dominant role of the magnetic anisotropy over the other anisotropies was revealed. A uniaxial in-plane anisotropy was observed for (110) oriented films, which was found to be caused by the magnetoelastic anisotropy. Interestingly, a trend to spin reorientation toward out-of-plane direction was deduced for (110) oriented films. After all, it was proved that strain can be used as a control parameter to change the magnetic anisotropy in epitaxial LCO thin films.

The influence of the strain on the time dependence of the magnetization was studied as well. An apparent energy barrier distribution in epitaxial LCO thin films was found. Moreover, we have shown that the distribution function, $f(\Delta E)$, can be described by a log-normal function. In addition, we demonstrated the influence of strain on the shape of $f(\Delta E)$. It was revealed that strain leads to a decrease of the width of the distribution function, σ. The magnetic viscosity, S_0 was found to increase with strain.

Contents

Chapter 1

Introduction

$3d$ transition metal oxides present a rich variety of magnetic states coupled with transport and structural properties as a result of coexisting spin, orbital and lattice degrees of freedom [1]. For these materials with perovskite structure ABO_3 the role of the BO_6 surrounding the transition-metal ion B octahedra is of great importance for the magnetic and conduction properties, because the BO_6 octahedra are central to the exchange mechanism. $LaCoO_3$ (LCO) is a perovskite oxide material that has been intensively studied over five decades mainly because of the different thermally driven spin states. Bulk LCO is diamagnetic with low-spin ground state (LS) ($t_{2g}^6 e_g^0, S = 0$). Above 100 K it undergoes a transition to higher spin states. However, the nature of the transition is still under debate [2–8]. In particular, two distinct higher spin states have been proposed, the intermediate spin state (IS) ($t_{2g}^5 e_g^1, S = 1$) [8–10], and the high spin state (HS) ($t_{2g}^4 e_g^2, S = 2$) [5, 11–13]. The possibility of multi-spin states origins from a delicate interplay between the crystal-field splitting, Δ_{CF}, and the inter-atomic exchange interaction, J_{EX} (Hund's rule coupling). The temperature dependence of the transition is brought about by the dependence of the crystal field splitting on the bond-length [14] which in turn changes with temperature. This naturally suggests epitaxial strain as an alternate handle to tune the spin state transition and therefore change the magnetism.

Recently, LCO has attracted renewed interest due to the observation of a ferromagnetic (FM) order in epitaxially strained thin films. Fuchs $et al.$ [15] have grown epitaxial LCO thin films on LSAT substrates, which shows ferromagnetic transition below T_c=85 K. The existence of either long- or short-range ferromagnetic order has been reported for various types of LCO samples [16–20]. The origin of the ferromagnetism is still under investigation. However, recent works strongly indicate that the ferromagnetic state in the strained LCO films is caused by structural distortion [21–26]. These results suggest a study of transport and magnetic properties of LCO in dependence on strain. Most interestingly, one can think about tuning the magnetic properties of LCO thin films in a controlled way by epitaxial strain, which would be also very interesting with respect to applications.

Strain-engineered thin film devices with tunable physical properties have significant impact on both technology and material science [27,28]. In particular, the emergence of new electric and magnetic properties can be realized with desired tunability of the strain modification [29,30]. In recent times there has been a resurgence of interest in $3d$ metal oxides with the specific aim of controlling their properties with external parameters such as strain and electrical field. Several works have been addressed to study the modification of physical properties introduced by epitaxial strain [31–35]. Moreover, in the past years, fabrication methods of thin oxide films with very high quality have been developed. The use of techniques such as sputtering, molecular beam epitaxy (MBE) and pulsed laser deposition (PLD), enabled the fabrication of high-quality transition metal oxide thin films on different substrates with varying strain.

Among the magnetic properties of metal oxide thin films, magnetic anisotropy is an intriguing subject from a fundamental and technological point of view. Since modern thin film magnetic devices such as magnetic recording media, heads and sensors are getting thinner and smaller to enhance recording density and sensitivity, it is important to know and control magnetic anisotropy, particularly, controlling the easy-axis of magnetization. Magnetic anisotropy in epitaxial thin films is determined by the balance between the magnetocrystalline energy, and both magnetostatic and magnetoelastic energy. As the magnetoelastic anisotropy is related to strain, it is one of the most easily controllable factors. The strong sensitivity of the magnetic anisotropy to the epitaxial strain has already been observed in several systems, and it is known that magnetoelastic anisotropy is more than an order of magnitude larger than magnetocrystalline anisotropy in transition metal oxides [36–40]. This suggests that strain may be used to tailor the magnetic anisotropy in epitaxial LCO thin films.

The time dependence of the magnetization is a well-known phenomenon observed in many systems, and arises from the thermal activation of magnetization changes over energy barriers. The nature of barriers can arise from anisotropy, or from domain wall pinning or nucleation mechanism, but in general, there is always a distribution of such barriers [41]. The rate of the magnetization change is known as magnetic viscosity, S, and is directly related to the value of energy barrier distribution. Magnetic viscosity measurements have been proposed as a method of understanding the magnetization reversal in hard magnetic materials [42]. There have been several works revealing the influence of external parameters on the time dependence of the magnetization [43–47]. To our knowledge, there is no work reported on the effect of strain on the time dependence of magnetization in $3d$ metal oxide thin films.

The main aim of this thesis is to study the exceptional magnetic properties of epitaxial LCO thin films grown by pulsed laser deposition on different single crystalline substrates. These epitaxial LCO films show many interesting magnetic properties such as magnetization and magnetic anisotropy depending on the change in strain state when different substrates are used. Strain can be used to control physical parameters such as lattice parameter and bonding angles to tune the magnetic anisotropy and the time dependence of the magnetization. To this purpose a home-made magneto optical Kerr effect (MOKE) magnetometer and Kerr microscope have been constructed. Using these apparatuses a detailed study of the magnetic anisotropy and magnetization reversal, that are very sensitive towards strain was conducted.

Chapter 2

Fundamentals

A description of the different fundamental properties of $LaCoO_3$ (LCO) is presented in this chapter. Theoretical background of magnetic anisotropy and time dependence of the magnetism is explained. The existing models for the time dependence of magnetization are reviewed.

2.1 Perovskites

Oxides of ABO_3 composition (A= alkali, alkaline earth or rare earth and B=3d, 4d transition metal in general) constitute a large family of metal oxides of current interest to solid state and materials chemistry [48–51]. Among the several structure types exhibited by ABO_3 oxides, the perovskite structure is probably the most well known and widely investigated. One description of the ideal perovskite structure is to consider corner linked BO_6 octahedra with interstitial A cations surrounded by twelve oxide ions. In idealized cubic perovskite, A-O and B-O bond distances are equal and perfectly matched. Most perovskite structures are distorted and do not have cubic symmetry. Common distortions such as cation displacements within the octahedra and tilting of the octahedra are related to the radius size of the A and B cations. The Goldschmidt tolerance factor, $t = (r_A + r_O)/\sqrt{2}(r_B + r_O)$, can be used as a measure of the degree of distortion of a perovskite-like structure from ideal cubic. Therefore, the closer to cubic, the closer the value of the tolerance factor is to unity [52]. Stable structures that have values approximately $0.78 < t < 1.05$ are considered in the perovskite family. When $t \leq 0.9$ perovskite will be orthorhombic, and for $0.9 < t < 1$ rhombohedral, while it will have tetragonal symmetry for $t > 1$.

2.2 Survey of $LaCoO_3$

Cobaltates have recently received intense interest, both experimentally and theoretically. A large number of interactions in this mixed-valent family of compounds (such as Hund's rule coupling, double exchange and crystal field) compete on a similar energy

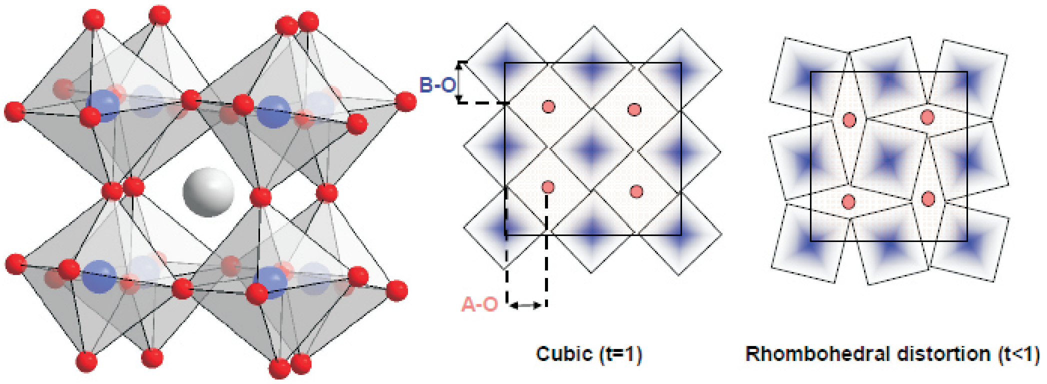

Figure 2.1: The crystal structure of $LaCoO_3$ ($R\bar{3}c$) with a Co-O-Co bond angle of 163° and a Co-O bond length of 1.93Å (left), the rotation of the oxygen octahedra from the ideal cubic structure (middle) to rhombohedral distorted structure from top view (right).

scale and lead to a rich landscape of mutually competing phases, many with unusual macroscopic properties [53]. In this respect, cobaltates are somewhat similar to manganites and also cuprates but do show their own unique flavor such as the fact that often two or three spin states are nearly degenerate.

2.2.1 Crystal structure

Bulk $LaCoO_3$ (LCO) shows a rhombohedral distorted perovskite structure with Co-O bond distance of about 1.93Å and a Co-O-Co angle of 163 ° as shown in Fig. 2.1. The rotation of the oxygen octahedra around the [111] axis allows for a smaller unit cell, resulting in a smaller tolerance factor, t=0.97 [54]. Since the deviation of the tolerance factor from the ideal cubic structure is small, the structure can still be regarded as a pseudo-cubic structure, which results for LCO in a pseudo-cubic lattice parameter of a=3.826 Å.

2.2.2 Electronic structure

$LaCoO_3$, having a Co $3d^6$ electronic configuration, shows an interesting electronic structure with three possible spin states, namely low (LS) $t_{2g}^6 e_g^0$ (S=0) for $T \leq 35$ K, intermediate (IS) $t_{2g}^5 e_g^1$ (S=1) mainly for $35\text{K} \leq T \leq 100$ K and high spin states (HS) $t_{2g}^4 e_g^2$ (S=2) mainly for $T > 100$ K. This results from a delicate interplay between the crystal-field splitting, Δ_{CF}, and the intra-atomic exchange interaction, J_{EX} (Hund's rule coupling).

Hund's rule coupling

The combination of total angular quantum numbers which are found to minimize the energy can be estimated using Hund's rules [1]. These three empirical rules are listed in order of decreasing importance [55]:

1. Arrange the electronic configuration so as to maximize the spin S. In this way the Coulomb energy is minimized because of the Pauli exclusion principle, which prevents electrons with parallel spins being in the same place, and this reduces Coulomb repulsion between the electrons.

2. The next step is, given the wave function determined by the first rule, to maximize L. This also minimizes the energy and can be visualized by imagining that electrons in orbits rotating in the same direction can avoid each other more effectively and therefore reduce the Coulomb repulsion.

3. Finally, the value of J is found using $J =\mid L - S \mid$ if the shell is less than half full and $J =\mid L + S \mid$ if it is more than half full. This third rule arises from an attempt to minimize the spin-orbit energy. [2]

Domination of the Hund's rule coupling usually leads to a high spin configuration.

Crystal-field splitting

The crystal field is the electric field exerted by neighboring atoms in a crystal. The ligand field theory, which is essentially an extension of molecular orbital theory, establishes the role of d orbitals on the central ion and their overlap with surrounding ions (ligands). The size and the nature of crystal field effects depend crucially on the symmetry of the local environment. Considering an octahedron, the crystal field arises mainly from electrostatic repulsion from negatively charged electrons in the oxygen orbitals. The d orbitals fall into two classes, the t_{2g} orbitals which point *between* the x, y and z axes (these are the d_{xy}, d_{xz} and d_{yz} orbitals) and the e_g orbitals which point *along* these axes (the d_{z^2} and the $d_{x^2-y^2}$ orbitals), which are shown in Fig. 2.2. It is clear that t_{2g} orbitals have less overlap with the p orbital of the neighboring oxygen atoms than the e_g orbitals and hence a lower electrostatic energy. Consequently, the three orbitals d_{xy}, d_{xz}, d_{yz} will be lowered in energy, but d_{z^2} and $d_{x^2-y^2}$ will be raised in energy. The $3d$ states, therefore, split into the sixfold degenerate t_{2g} and the the fourfold degenerate e_g levels. The splitting is known as the crystal field splitting, Δ_{CF}, shown in Fig. 2.3. The domination of Δ_{CF} usually leads to a low spin configuration.

---

[1] Hund's rules are only applicable to the ground state configuration, and do not imply anything about the ordering of levels above the lowest level. They also assume that there is only one subshell which is filled partially.

[2] One should note that the third rule is only applicable in certain circumstances. In many systems, transition metal oxides being good examples, the spin-orbit energies are not as significant as some other energy terms such as the crystal field so that Hund's third rule is disobeyed. However, for rare earth ions Hund's third rule works very well.

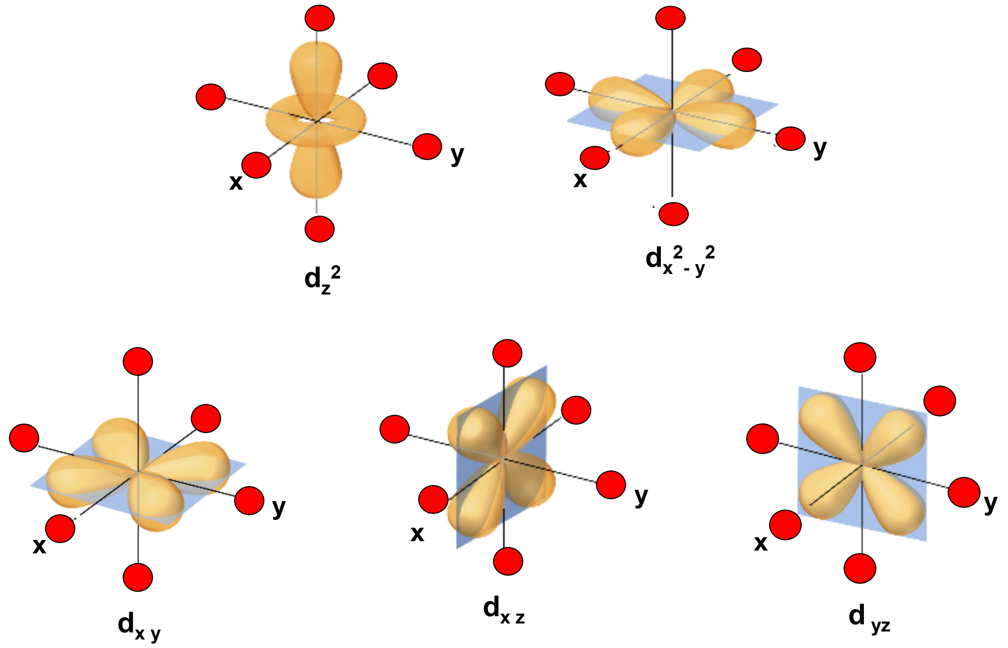

Figure 2.2: The $3d$ orbitals of Co^{3+} ion located in the oxygen (red) octahedral environment. The d_{z^2} and $d_{x^2-y^2}$ levels are grouped together and called the e_g levels. The d_{xy}, d_{xz} and d_{yz} levels are grouped together and called the t_{2g} levels. The electrostatic interaction between electrons of the t_{2g} orbitals and the surrounding oxygen electrons is less than that of e_g orbitals. Thus, the t_{2g} levels are lowered in energy with respect to the e_g levels.

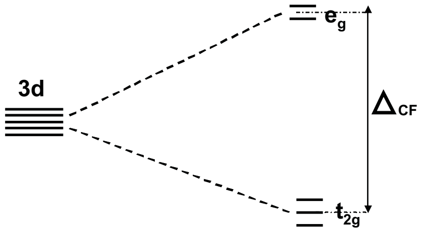

Figure 2.3: The splitting of the $3d$ levels due to the crystal field in an octahedral environment.

Spin states

The $3d^6$ electrons can now, respective to the strength of the crystal field-splitting Δ_{CF} in comparison to the exchange-interaction J_{EX}, be distributed in three ways shown in Fig. 2.4. For $\Delta_{CF}>3J_{EX}$ (strong-field case) all six electrons reside in the

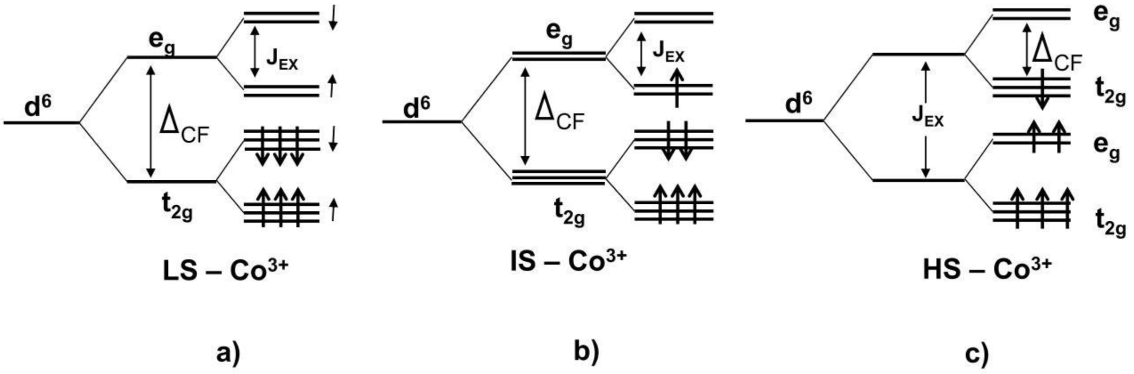

Figure 2.4: Schematic diagram of the spin state of trivalent Co ions: a) low-spin (LS) Co^{3+} ion ($\Delta_{CF} \gg J_{EX}$); b) intermediate-spin (IS) Co^{3+} ion; c) high-spin (HS) Co^{3+} ion with $J_{EX} \gg \Delta_{CF}$, where J_{EX} is the intra-atomic exchange energy and Δ_{CF} is the crystal field energy.

t_{2g} levels. This state has a total spin of $S = 0$ and is denoted as low-spin state ($t_{2g}^6 e_g^0$). For $2J_{EX} < \Delta_{CF} < 3J_{EX}$, first, the three spin-degenerate t_{2g} orbitals are filled with one electron each. Minimization of the total energy is possible when one electron is placed in the e_g level and the remaining two in the t_{2g} levels, requiring that the latter have opposite spin. This state of total spin S=1 ($t_{2g}^5 e_g^1$) is called intermediate spin state (IS). Finally, when $J_{EX} > \Delta_{CF}$ (weak-field case) all spin-up level are occupied first and the last electron populates a spin-down t_{2g} orbital, resulting in a total spin of S=2 ($t_{2g}^4 e_g^2$) which is called the high-spin state (HS). Recent experiments [56] have provided strong evidence that bulk Co^{3+} ions are in their non-magnetic low-spin state at the lowest temperature, but change to a primarily intermediate-spin state in the temperature range 35 K<T<100 K [8] and further to a mixture of IS and high-spin states in the interval 300 K<T<600 K. On the other hand, the existence of IS has been questioned recently on the basis of x-ray absorption spectroscopy and magnetic circular dichroism [5]. The crossover between spin states is due to the subtle balance between the crystal-field splitting, Δ_{CF}, and exchange-interaction, J_{EX}. Since Δ_{CF} is found to be very sensitive to the variation of the Co-O bond length, r, ($\Delta_{CF} \propto r^{-5}$) [14], the subtle balance between Δ_{CF} and J_{EX} can easily be influenced by, e.g., hole or electron doping, and chemical or external pressure [57, 58].

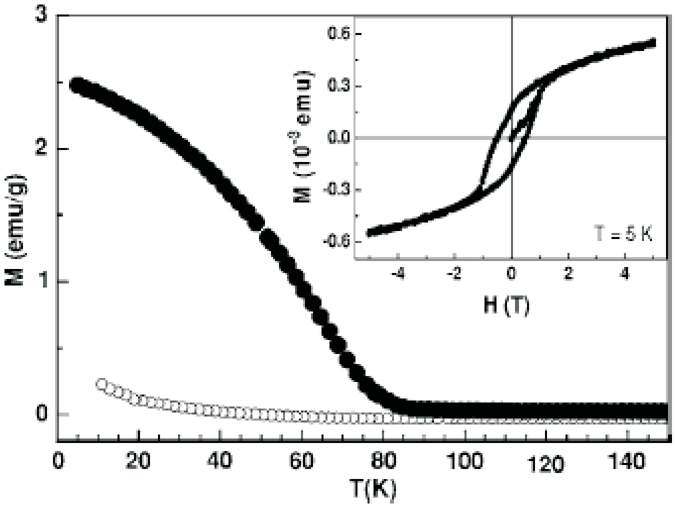

Figure 2.5: Field-cooled magnetization of polycrystalline (○) and epitaxial (●) $LaCoO_3$ films (d = 200 nm) on LSAT in an applied field of $\mu_0 H$=20 mT. The inset shows the magnetic moment of epitaxial $LaCoO_3$ at T= 5 K as a function of the applied field. Taken from [15].

2.2.3 Magnetism

Despite the nonmagnetic LS ground state of $LaCoO_3$ there are various reports on the existence of either long- or short-range ferromagnetic (FM) order [17–19, 59, 60]. For instance, Menyuk *et al.* [17] have attributed a hysteresis in the magnetization at 1.9 K to the existence of small isolated magnetic regions dispersed in a nonmagnetic matrix. Androulakis *et al.* [19] reported on two FM phases, one with a T_c <10 K and the other with 20 K< T_c <100 K. They suggest that these are caused by the presence of Co^{4+} ions associated with La^{3+} vacancies. Yan *et al.* [18] have found a FM component with a T_c ≈85 K and argued that the coordination of surface Co^{3+} ions is capable of stabilizing higher spin states, most probably IS state, and suggest a FM coupling of surface atoms.

A prime motivation this work was the observation by Fuchs *et al.* [15] of FM order in strained epitaxial LCO thin films on LSAT below T_c=85 K, whilst polycrystalline films did not exhibit any ferromagnetic order as shown in Fig. 2.5. Given the fact that their epitaxial films have pseudo-tetragonal structure in contrast to the bulk-like rhombohedral structure of polycrystalline films, they discussed the effect of the structural distortion on the ferromagnetic state. As a viable scenario for the observed FM behavior they suggested a strain-induced FM order: The tensile strain in epitaxial LCO films on LSAT leads to a decrease of Δ_{CF}, which stabilizes the IS and HS states due to the fact that Δ_{CF} rapidly decreases with increase of the Co-O bond length. In bulk LCO the IS state is Jahn-Teller (JT) active, and a cooperative JT distortion lifts the degeneracy of the e_g levels. However, the JT distortion might be strongly suppressed in the epitaxially strained films, where tensile stress exerted by the substrate may lead to a relief of JT strain. Therefore, the splitting of the e_g orbitals due to JT effect may also be suppressed. Under those assumptions, the superexchange interaction gives rise to FM ordering according to the Goodenough-Kanamori-Anderson rules [61–

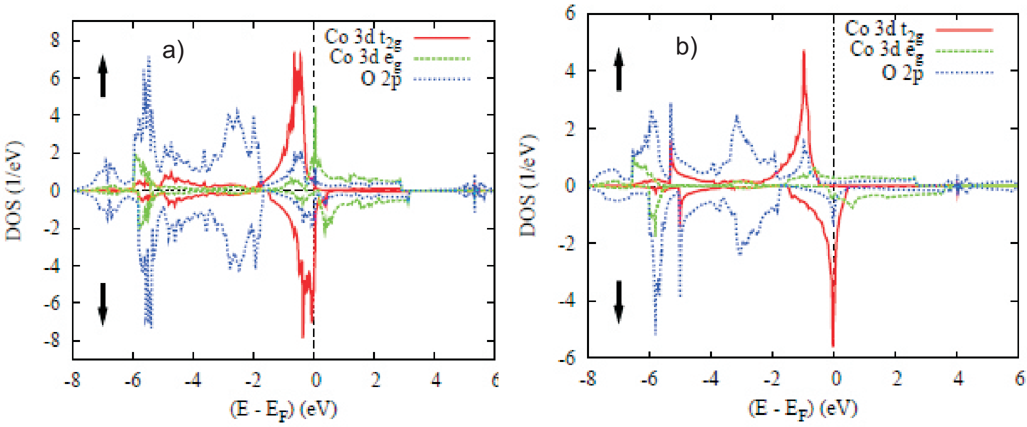

Figure 2.6: a) (Color line) Partial densities of states (DOS) of a rhombohedral ferromagnetic $LaCoO_3$. b) (Color line) Partial densities of states (DOS) of hypothetical simple cubic ferromagnetic $LaCoO_3$.

63]. Zhou *et al.* [21] also reported on FM order of LCO nanoparticles below 85 K. The experimental results support the assumption that a reduced Jahn-Teller distortion may play a crucial role in the stabilization of the FM state. In a very recent work, Herklotz *et al.* [22] observed a reversible strain effect on the ferromagnetic state of LCO grown epitaxially on piezoelectric substrates. These results indicate that the FM state of strained LCO films is caused by a structural distortion. LDA calculations from Eyert *et al.* [64] demonstrated that the tendency to long-range order is significantly influenced by the symmetry. They have calculated that partial densities of states (DOS) of t_{2g} levels near the Fermi energy (E_F), shown in Fig.2.6, increases for the simple cubic ferromagnetic $LaCoO_3$ in comparison to rhombohedral symmetry, and FM ground state lower in energy for cubic LCO in contrast to rhombohedral LCO.

2.3 Magnetic anisotropy

Magnetic anisotropy means that magnetization prefers a certain orientation. The various contributions to the magnetic anisotropy can be classified according to their physical origin. We distinguish between magnetic anisotropy due to spin-orbit coupling (SOC) and magnetic anisotropy of dipolar origin. The former includes magnetocrystalline and magnetoelastic anisotropy; the latter is responsible for shape anisotropy. In the following, a short overview of the electronic origin of magnetic anisotropy is given. The individual anisotropy contributions are discussed. The correlation between lattice strain and magnetic anisotropy is reviewed.

2.3.1 Magnetocrystalline anisotropy

Magnetocrystalline anisotropy is a direct consequence of spin-orbit coupling. Crystalline anisotropy can be thought of as a torque which tends to align the magnetization

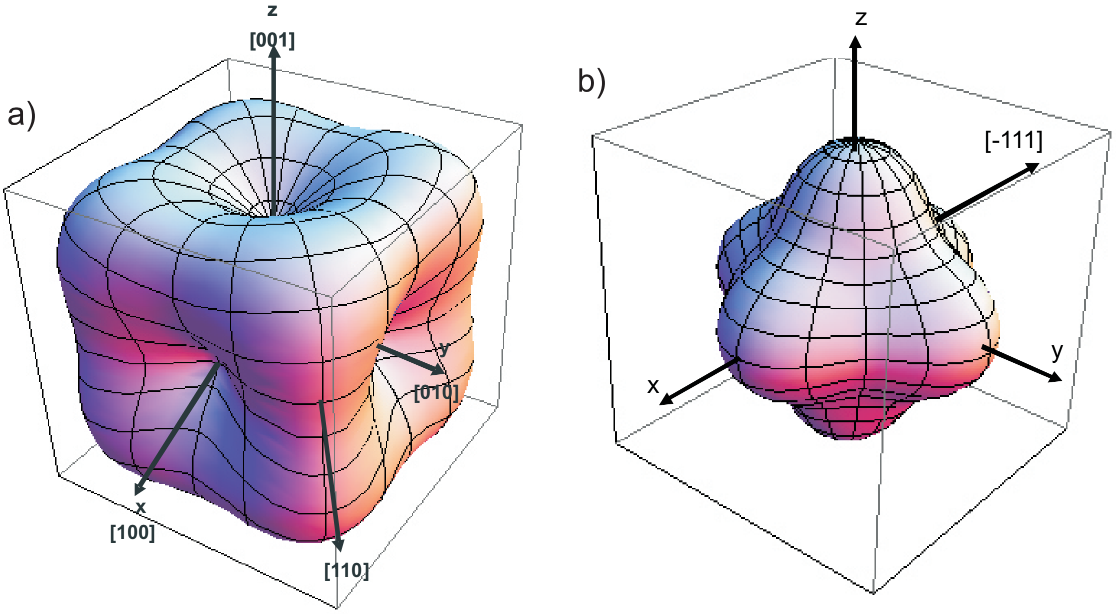

Figure 2.7: a) The calculated anisotropy energy for $K_1 > 0$, typical for a cubic system. The energy minima are along the $< 100 >$ direction, which are referred to as easy axes. b) The anisotropy energy for $K_1 < 0$, typical for a cubic system. The location of the energy minima changed, the easy axes are now along the $< 111 >$ direction.

to a certain direction within the crystal. The preferred direction for the magnetization is called the easy axis. In bulk samples the orbital moment is quenched, and the contribution of the orbital moment to the total magnetic moment is small. This means that the magnetism of bulk crystals is largely due to the spin moment. The orbital moment of $3d$ electron in transition metals and compounds is tightly fixed to the crystal lattice and can be oriented very little in an external field [65]. The electron spin, however, is only weakly coupled to the orbital moment via the spin-orbit coupling, and the energy of the system depends on the relative orientation between the magnetization (spin orientation) and crystal axes. This is known as the magnetocrystalline contribution to the anisotropy. Perturbation theory suggests that the magnitude of the lowest-order anisotropy constant K_1 scales as $K_1 \sim \xi^4/W^3$ for a cubic system. The spin-orbit coupling constant ξ is of the order of 50-100 meV for $3d$ elements, and the $3d$ band width, W, is of the order of a few eV. The associated crystalline anisotropy energy density for cubic symmetry is given by:

$$E_c = K_1(\alpha_1^2\alpha_2^2 + \alpha_2^2\alpha_3^2 + \alpha_3^2\alpha_1^2) + K_2\alpha_1^2\alpha_2^2\alpha_3^2 + ... \tag{2.1}$$

where K_1, K_2 are anisotropy constants, and the α's are direction cosines between magnetization vector and crystal coordinate system (see Appendix). Generally, the second order term, K_2, is neglected as it is much smaller than K_1. For $K_1 > 0$, which is typical for a cubic system like bcc Fe, the energy minima are along the $< 001 >$ directions, making them the magnetically easy axes. The case for $K_1 < 0$ causes the energy minima located along the $< 111 >$ axes, which is the case for fcc Ni. This is illustrated in Fig. 2.7 for cubic symmetry.

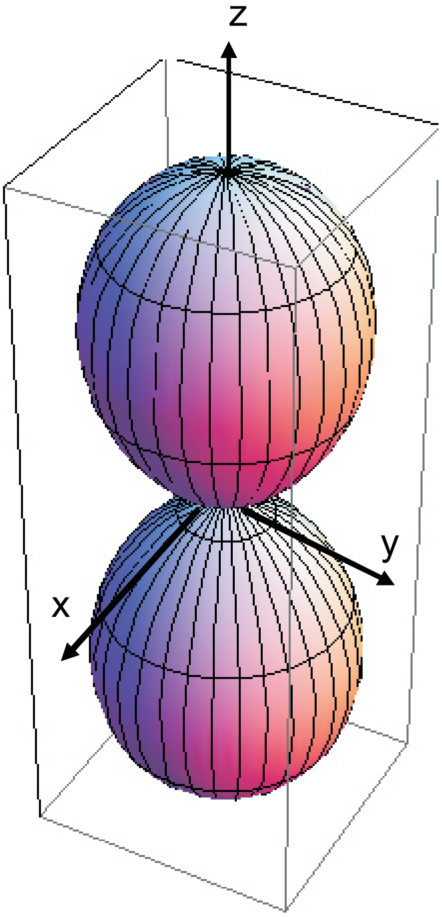

Figure 2.8: The calculated anisotropy energy caused by the shape of the film. The energy shows minima in the x-y film plane, which favors in-plane magnetization for a quadratic film plane.

2.3.2 Magnetic dipolar anisotropy (shape anisotropy)

Among the most important sources of the magnetic anisotropy in thin films is the long-range magnetic dipolar interaction. The shape effect of the dipolar interaction in ellipsoidal ferromagnetic samples can be described via an isotropic demagnetizing field, H_d, given by H_d=-NM. Here M is the magnetization vector and N is the shape-dependent demagnetizing tensor. For a thin film, all tensor elements are zero except for the direction perpendicular to the layer: $N^{\perp} = 1$. Since the dipolar energy can be expressed as

$$E_d = -\frac{\mu_0}{2V}\int M \cdot H_d \, dv \tag{2.2}$$

where μ_0 is the magnetic field constant and the integration is performed over the volume V of the sample, it results in an anisotropy energy contribution, the so-called shape anisotropy, per unit volume of a film of:

$$E_d = \frac{1}{2}\mu_0 M_s^2 \alpha_3^2 \tag{2.3}$$

Here the magnetization is assumed to be uniform with a magnitude equal to the saturation magnetization M_s. According to this expression, the contribution favors an in-plane orientation for the magnetization shown in Fig. 2.8.

2.3.3 Magnetoelastic anisotropy

The coupling between magnetism and lattice strain is a well-known experimental fact, known as magnetostriction for bulk samples [66]. The sample dimensions change if the direction of the magnetization is altered resulting in the minimization of the total energy of the system. Conversely, strain in a ferromagnet may alter the direction of the magnetization. The underlying principle of the so-called magnetoelastic coupling can be described as the strain dependence of the magnetic anisotropy energy density [67]. This coupling between the lattice strain and magnetic anisotropy is decisive for the magnetic properties of epitaxially strained thin films. The magnetoelastic anisotropy originates from spin-orbit coupling. For instance, the energetically degenerate $3d$ levels of a free atom split into two groups, e_g ($d_{z^2}, d_{x^2-y^2}$ orbitals, electron density large along the cubic axes) and t_{2g} (d_{xy}, d_{xz}, d_{yz} orbitals, electron density large between the cubic axes), in the presence of an octohedral crystal field. The energy separation and relative positioning of the e_g and t_{2g} levels depend on the symmetry of the atomic arrangement [55], and a tetragonal distortion lifts the degeneracy of these levels [68]. Thus, a change of symmetry, induced by strain, may lead to the change of the relative occupancy of the different d orbitals, which in turn leads to a change of the magnetic anisotropy via spin-orbit coupling.

Magnetoelastic coupling contributes to the energy density of the film via a term proportional to the strain, ϵ_i, and magnetoelastic coupling coefficient, B_i. The magnetoelastic anisotropy energy density for cubic symmetry is given by [69]

$$E_{me} = B_1(\epsilon_1\alpha_1^2 + \epsilon_2\alpha_2^2 + \epsilon_3\alpha_3^2) + 2B_2(\epsilon_{12}\alpha_1\alpha_2 + \epsilon_{23}\alpha_2\alpha_3 + \epsilon_{31}\alpha_3\alpha_1) + ... \tag{2.4}$$

The film strains are denoted by ϵ_{ij}, where the Voigt-notation has been applied [70], and magnetoelastic coupling coefficients are given by B_i. Both direction cosines α_i and strain ϵ_{ij} are given in a cubic crystal system, which in general does not coincide with the film's coordinate system in general. This requires appropriate tensor transformations for orientations other than cubic (100). The necessary transformation is given as an example for cubic (110) and (111) planes in Appendix A. The magnetoelastic coupling coefficient is a measure of the strain-dependent terms in the magnetic anisotropy energy density. The magnetostriction coefficient, λ, and the magnetoelastic coupling coefficient, B, are directly related to each other by elastic constants. They have opposite signs, as shown formally following:

$$B = -\lambda C_{ij} \tag{2.5}$$

where C_{ij} represents a tensor of elastic constants. B depends on temperature, composition, and, in thin films, on thickness. In Fig. 2.9, the magnetoelastic energy is illustrated for in-plane tensile strained ($\epsilon_1 = \epsilon_2 = -\epsilon_3 = \epsilon, \epsilon_{12} = \epsilon_{13} = \epsilon_{23} = 0$) cubic (100) oriented films for $B_1 < 0$ and $B_1 > 0$. Obviously, a tensile strain induces uniaxial

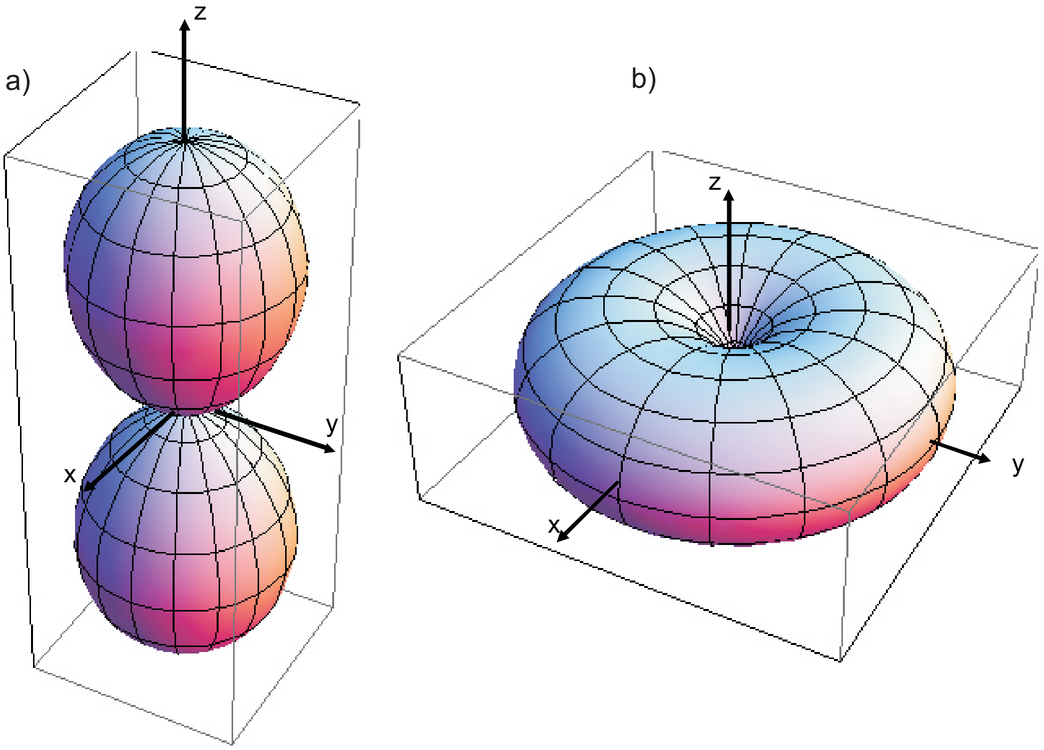

$B_1<0$ $B_1>0$

Figure 2.9: The anisotropy energy caused by an isotropic tensile strain in the film plane for different sign of the magnetoelastic coefficient B_1. a) The uniaxial anisotropy with hard axis along the z direction and easy axis on the x-y plane caused by $B_1 < 0$. b) The uniaxial anisotropy with easy axis along the z direction caused by $B_1 > 0$

anisotropy, and direction of the easy and hard axes depends on the sign of B_1. A negative B_1 value causes the easy axis aligned in the $x - y$ plane while a positive B_1 favors the magnetization along the z axis.

The total effective anisotropy energy in a thin film is a sum of the individual energy terms. The surface/interface anisotropy becomes dominant only in ultrathin films (several atomic layers), and can be therefore neglected in our studies where the film thickness is usually larger than 100 monolayers. Thus, we can write the total anisotropy energy density as follows:

$$\begin{aligned} E_a &= E_{mc} + E_d + E_{me} \\ &= K_1(\alpha_1^2\alpha_2^2 + \alpha_2^2\alpha_3^2 + \alpha_3^2\alpha_1^2) + \frac{1}{2}\mu_0 M_s^2\alpha_3^2 + B_1(\epsilon_1\alpha_1^2 + \epsilon_2\alpha_2^2 + \epsilon_3\alpha_3^2) \\ &+ 2B_2(\epsilon_{12}\alpha_1\alpha_2 + \epsilon_{23}\alpha 2\alpha 3 + \epsilon_{31}\alpha_3\alpha_1) \end{aligned} \tag{2.6}$$

According to Eq. (2.6), the equilibrium orientation of M in a magnetic material is determined by the competition of magnetocrystalline, magnetoelastic and shape anisotropies. The sign and magnitude of K_1 and B_i as well as of ϵ_{ij} become decisive to govern the total anisotropy of the magnetic thin film.

2.4 Models for the time dependence of magnetization

The time dependence of magnetization, the so-called magnetic after-effect, is a rather complicated phenomenon. Many models have been proposed based on phenomenological studies and first principles calculations. The magnetic after-effect which characterizes the fact that a magnetic field suddenly applied/removed to/from a ferromagnetic substance at time t_0, induces a change in the magnetization that begins a time t_i very close to t_0, but which may continue for a very long time beyond t_i. In magnetic materials the time dependence effects arise due to finite relaxation time τ required for the magnetization vector to rotate minima between two energy separated by an energy barrier. The origin of the energy barrier is a material property and its magnitude depends on experimental conditions such as magnetic field, which governs the probability of thermally activated transitions. Almost any phenomenology shows that the probability of a transition (or inverse relaxation time) is given by

$$\tau^{-1} = f_0 \exp(-\Delta E/kT) \tag{2.7}$$

where f_0 is the attempt frequency, which depends on the properties of the material, it is of the order $10^8 - 10^{12}$ s^{-1}. ΔE is the energy barrier height, which is a function of the applied field and kT (k is Boltzmann constant) [41]. If the energy barriers are identical, following the theory of Néel [71], the time dependence of the magnetization after previous saturation is given by

$$M(t) = M(0) \exp(-t/\tau) \tag{2.8}$$

There have been several different time dependencies of the magnetization observed. Chamberlin [72] summarized the time dependence of the magnetization in terms of different mathematical expressions as is described in the following.

2.4.1 Curie-von Schweidler power law

A power law is predicted by scaling theories for domain growth and internal dynamics [73]. Calculations based on the Sherrington-Kirkpatrick mean-field model for spin-glasses suggest that the magnetization decays algebraically as

$$M(t) = M_0\, t^{-\zeta},\ \ \zeta > 0. \tag{2.9}$$

Sinha *et al.* [74] found that in spin-glasses such as ν-FeNiCr alloys $M(t)$ fits well to the power-law decay. Ulrich *et al.* [75] studied the magnetic relaxation of single-domain particles below the blocking temperature. They found that for all particle densities the relaxation decay followed a power law. They used Monte-Carlo simulations to study the influence of the dipolar interactions and polydispersion on the magnetic relaxation of single-domain FM particles below the blocking temperature, and simulations predicted power-law behavior for internal dynamics.

2.4.2 Stretched exponential

The most popular empirical expression for characterizing disordered materials is the Kohlrausch-Williams-Watt stretched exponential:

$$M(t) = M_0 \exp\left(-(t/\tau)^{\beta}\right), \quad 0 < \beta < 1, \tag{2.10}$$

It has also been observed in a variety of complex materials and systems such as supercooled fluids, spin glasses, molecular systems, glassy soft matter etc. [76, 77]. Chamberlin *et al.* [78] studied the time decay of the thermo-remanent magnetization in $Cu_{1-x}Mn_x$ and $Ag_{1-x}Mn_x$ spin glasses. They found it to be a stretched exponential function.

2.4.3 Fatuzzo model

Fatuzzo [79] has elaborated thin film relaxation associated with the nucleation and growth of domains. The magnetization is initially saturated along an easy axis, and then the external field is applied in opposite direction. As a consequence, the magnetization relaxes and reverses its direction. In this model, magnetization reversal occurs first by nucleation of domains with the rate of R, where each domain assumed to be circularly shaped with initial radius r_c can grow with a radial velocity v. The time dependence is described by [80]:

$$M(t) = M_0 \mathrm{exp}\left(-\left(Rt/\tau\left(k\right)\right)^{\beta(k)}\right) \tag{2.11}$$

where $k = v/Rr_c$ is the ratio between the rates of the two processes involved, domain nucleation and domain wall propagation. The shape of the relaxation curves can be characterized with a proper value of k. By fitting experimental data to equation 2.11 the characteristic of nucleation and domain growth can be readily obtained. It turns out that nucleation will govern the reversal process for low value of k ($k \to 0$), conversely, for large values of k domain propagation will be predominant [81].

2.4.4 Logarithmic decay and energy barrier distribution

For magnetic after effects, logarithmic time dependence $M(t) \propto log(t)$ is a popular description. This model takes the distribution of the energy barriers, ΔE, into account. The distribution of energy barriers is fundamental of all systems. In real systems there is always a distribution of relaxation times brought about by a distribution of ΔE which can arise from the differences in the local anisotropy, domain wall pinning, defects etc. The distribution function of the energy barriers in real systems, $f(\Delta E)$, has generally the form of a Gaussian-like function. For instance, for non-interacting fine particles and grains, a log-normal [3] distribution function of energy barriers is found in general [82–84]. El-Hilo [41] *et al.* theoretically predicted the time dependent

---

[3] A log-normal distribution function can be considered as Gaussian function with a logarithmic tail

behavior of a particulate recording medium assuming that the system holds a log-normal distribution of the energy barriers, and experimental results were consistent with the predictions. Recently, a log-normal distribution function of the energy barriers in GePt/FePt films was reported [85]. Moreover, in some systems, presence of the Γ and Gaussian distribution functions of energy barriers were reported [78, 86].

Linear law and magnetic viscosity

Chantrell *et al.* [72] gave a phenomenological theory based on the intrinsic energy barrier to explain the form of the time dependence of the magnetization. By following the treatment given by Ref. [72], a general form of Eq. 2.8 by taking the distribution of the energy barriers into account is written as:

$$M(t) = B + A \int_0^{\infty} e^{-t/\tau(y)}\, f(y)\, dy, \tag{2.12}$$

where $B = M(\infty)$ and $A = M(t = 0) - M(\infty)$ are time-independent constants. $f(y)$ is the distribution of energy barriers, and $y = \Delta E/\Delta E_m$ is the reduced energy barrier relative to the average barrier ΔE_m of the system. $\tau(y) = \tau_0 \exp(\alpha y)$ is the relaxation time and $\alpha = \Delta E_m/kT$. The change in the values of α can arise from temperature changes or magnetic field changes. In order to understand the physical interpretation of the role of the energy barrier distribution, it is useful to simplify the integral in Eq. 2.12 using the critical energy barrier of activation, ΔE_c. This critical barrier can be defined in such a way that activation over barriers lower than ΔE_c happens so quickly that $e^{-t/\tau(y<y_c)} \simeq 0$. With $e^{-t/\tau} \simeq 1$ for $y > y_c$ Eq. 2.12 becomes

$$M(t) = B + A - A \int_0^{y_c(t)} f(y)\, dy, \tag{2.13}$$

where $y_c = \Delta E_c/\Delta E_m$ is the reduced critical barrier for reversal and is given using Eq. 2.8 by

$$y_c = \frac{1}{\alpha} \ln(t/\tau) \tag{2.14}$$

According to Eq. 2.13 the time dependent behavior is most sensitive to two parameters which characterize the relevant distribution of energy barriers for the system, i.e., the average energy barrier of the system ΔE_m and the width of the distribution, σ. Assuming a constant distribution function, $f(y)$=constant, Eq. 2.13 can be written as:

$$M(t) = M_0 + S(H_r, T) \ln(t) \tag{2.15}$$

which is known as a linear law, where $S = A/\alpha$ is a time-independent constant. This law implies that the variation of $M(t)$ vs $\ln(t)$ is linear due to the fact that $f(y_c)$ does not change around the critical barrier over the range of time examined. In other words, for a system that exhibits wide range of energy barriers (large σ), the magnetization time decay follows a $\ln(t)$ behavior resulting from the superposition of many exponential decays with different magnetic relaxation times, and consequently for a wide distribution of energy barriers, a $\ln(t)$ law is a good approximation. Here S is called the “magnetic viscosity“, which is a function of the applied reverse field, H_r, and the temperature, T. M_0 is a constant for a given measuring field. The magnetic viscosity coefficient, S, is the rate of the change of the magnetization. Larger S implies larger change in the magnetization during the observation time. S is expected to reach a peak value near the coercive field, H_c, where the rate of the change of the moment with time reaches a maximum.

Origin of the nonlinear ln(t) behavior and the $S - f(\Delta E_c)$ relation

As discussed above $\ln(t)$ behavior is only the case for a very special distribution function of energy barriers: $f(y)$ is constant. However, in reality, only a few magnetic systems have a constant distribution function. For a system with a non-constant distribution function, non-linearity arises in the time dependence of magnetization ($M(t)$ vs $\ln(t)$). This behavior can be seen by considering a non-constant $f(y)$ in the integral in Eq. 2.13. According to Eq. 2.13 the rate of the change of $M(t)$ with $\ln(t)$ is given now by

$$\frac{\partial M(t)}{\partial \ln(t)} = -\frac{A}{\alpha} f(y_c). \tag{2.16}$$

This result predicts that a non-linearity will arise in the variation of $M(t)$ vs ln(t) due to significant variation of $f(y_c)$ during the time dependent process. An analytical expression of Eq. 2.13 can be derived by representing the behavior of $f(y)$ around y_c using a series expansion

$$M(t) = M_0 - A \sum_{n=0} f^n(y_c) \left(\frac{\Delta \ln(t)}{\alpha} \right)^{n+1} \tag{2.17}$$

where Δ $\ln(t)$=$\ln(t/t_0)$ and t_0 is the initial time of measurement. $f^n(y_c)$ is the nth differential of the distribution function, which characterizes its curvature at y_c. It can be noticed that, according to Eq. 2.17, the origin of the non-linear behavior in the ln(t) law arises from the higher differentials of the distribution function, and in the case $f(y)$ constant, all the non-linear coefficients vanish, and hence, $M(t)$ will follow a ln(t) law. Following Eq. 2.17, for systems which exhibit non-linear behavior, the time dependence of the data can be interpreted by fitting the variation of $M(t)$ versus ln(t) to a polynomial. The zero coefficient of the polynomial will be $S(H_r, T)_{t=t_0}$.

$$\begin{aligned} \frac{M(t) - M_0}{\ln(t)} &= S_0 + S_1 \ln(t/t_0) + ..., \\ S_0 &= \frac{A}{\alpha} f(y_c) \\ S_1 &= 2\frac{A}{\alpha^2} f^1(y_c) \end{aligned} \tag{2.18}$$

This result indicates that the value of $S(H_r, T)$ is directly related to the behavior of the distribution function around the critical barrier above which thermal activation is taking place.

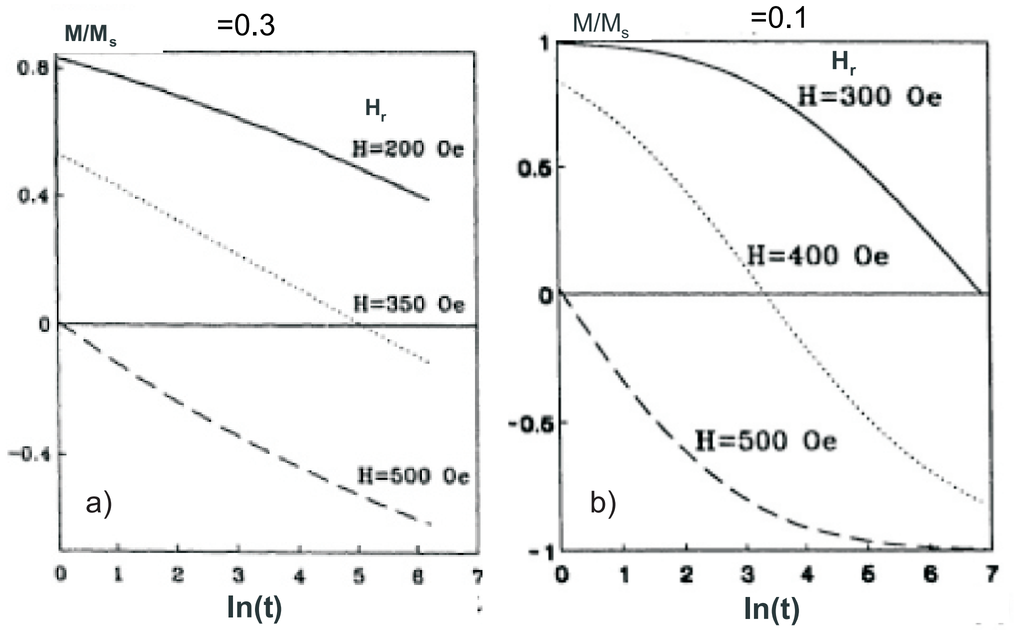

Figure 2.10: The calculated variation of the reduced magnetization with $ln(t)$ for a log-normal distribution of energy barriers for $\sigma = 0.3$ (a), and $\sigma = 0.31$ (b) for the different applied reverse fields. Notice that non-linearity in the variation of the magnetization increases for the system with $\sigma = 0.1$, with respect to that of $\sigma = 0.3$. $M(t)$ versus $ln(t)$ is concave downwards, upwards for $H_r < H_c$ and $H_r > H_c$, respectively. A crossover shows up for $H_r \approx H_c$. Taken from [82].

Effect of the width of the distribution on the time dependent behavior

Non-linear behavior in the $\ln(t)$ law of the time dependence of the magnetization is governed by the distribution of energy barriers. In their pioneering theoretical work, El-Hilo *et al.* [82] performed numerical calculations on the time-dependent magnetization of a magnetic system exhibiting a log-normal distribution function, $f(y) = (1/\sqrt{2\pi}\sigma y)exp(-[\ln(y)])^2/2\sigma^2)$, of the energy barriers. They found that the magnitude of the non-linear terms in the series expansion (Eq. 2.17) depends on the width of the distribution, i.e., $|S_n| \propto (1/\sigma^2)^n$. The magnitude of the non-linear terms increases when the width of the distribution, σ, becomes narrower. In other words, non-linearity in the variation of $M(t)$ vs $\ln(t)$ increases as the width of the distribution function, σ, decreases. Furthermore, for systems with a narrow distribution of energy barriers, they predicted the variation of the magnetization $M(t)$ with $\ln(t)$ to be concave downwards if the applied field, H_r, is smaller than the coercive field, H_c, whereas concave upwards behavior is predicted if $H_r > H_c$. For $H_r \approx H_c$ the variation of $M(t)$ with $\ln(t)$ is initially concave downwards while it is concave upwards at the end of the variation. A linear behavior is predicted for a relatively large value of σ. Fig.2.10 shows the calculated variation of magnetization for different values of σ, after El-Hilo *et al.* [82].

Chapter 3

Experimental Methods

This chapter covers the experimental techniques used in this work. The sample preparation and characterization methods of $LaCoO_3$ (LCO) thin films are presented in the first section. An experimental procedure to tune the epitaxial strain in the films is explained in the second section. The last section presents the theoretical background of the magneto-optical Kerr effect (MOKE) and the realization of a home-made magneto-optical measurement set-up, which is used to measure the MOKE hysteresis curves and to visualize the magnetic domain structure of the thin films.

3.1 Film preparation and characterization

3.1.1 Film preparation

In this work, epitaxial $LaCoO_3$ thin films with different strain were grown by pulsed laser deposition (PLD). Epitaxy refers depositing a single-crystalline film on a single-crystalline substrate. If a crystalline film is grown on a substrate of the same material, it is called homoepitaxy, while in heteroepitaxy, a crystalline film grows on a crystalline substrate of different material. The PLD technique is particularly suitable for the deposition of transition-metal-oxide (TMO) thin films, since these materials show usually a strong absorption in the UV range (e.g., in the energy range of the used excimer laser). In this method, the deposition parameters, such as substrate temperature, oxygen partial pressure, laser fluence and deposition rate, R, are varied in order to optimize the crystalline quality of the films. Furthermore, by selecting different, suitable substrate materials with different lattice parameters, the strain in the epitaxial film can be varied. The substrate temperature T_s plays a very important role in the growth process of the films. It provides kinetic energy to the atoms moving on the substrate surface. On the other hand, a very high T_s can lead to the evaporation of the deposited materials: since the different constituents have different vapor pressures, a high substrate temperature can cause the selective evaporation of those that have high vapor pressure resulting in a composition of the film deviating from the desired one. Of course the temperature should be kept constant over the entire deposition process. Another important parameter is the oxygen partial pressure in the deposition chamber,

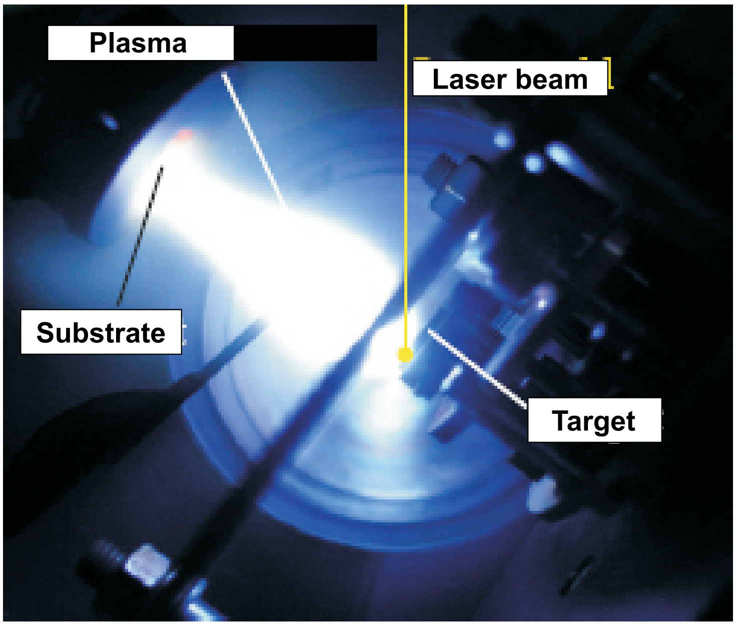

Figure 3.1: Picture of the PLD chamber used for the growth of the films. The target is hit by the excimer laser pulses. The resulting plasma is directed to the substrate.

which is ultimately responsible for the oxygen content of the sample. Fig. 3.2 shows a ternary phase diagram of La-Co-O containing compounds under thermal equilibrium at 1100°C.

As decreasing O_2 pressure more reduced perovskite-like phases of $La_{1+n}Co_nO_{3n+1}$ are formed. It is non trivial to determine the oxygen content of thin films. Therefore, the presence of the desired phase has to be confirmed indirectly. For the deposition of the samples used in this work, stoichiometric polycrystalline pellets prepared by the *sol-gel-method* are used. These pellets, also called *target*, are hit by the high-energy laser pulses. Due to the absorption of the light and subsequent heating, the material is ionized by explosion-like evaporation. The plasma plume consisting of ions of the target material is directed onto the substrate. A photograph of the PLD chamber is presented in Fig. 3.1. The details of the thin-film deposition can be found in Ref. [88]. The samples were optimized with respect to their structural properties, such as phase purity, crystallinity, mosaic spread and magnetic properties, such as ferromagnetic transition temperature, T_c, and magnetic moment. The optimized deposition parameters are as follows: T_s=650°C, $P(O_2)$=0.3 mbar, E=2.5 J/cm^2, R=0.5 Å/shot.

3.1.2 Structural characterization

The phase purity, crystallinity, mosaic spread and lattice parameters of the films were investigated by means of XRD using a 2-circle diffractometer in Bragg-Brentano geometry with CuK_α-radiation (λ=1.54056Å) equipped with a Ge monochromator. By this technique it is possible to draw conclusions about the epitaxy, the distance of the

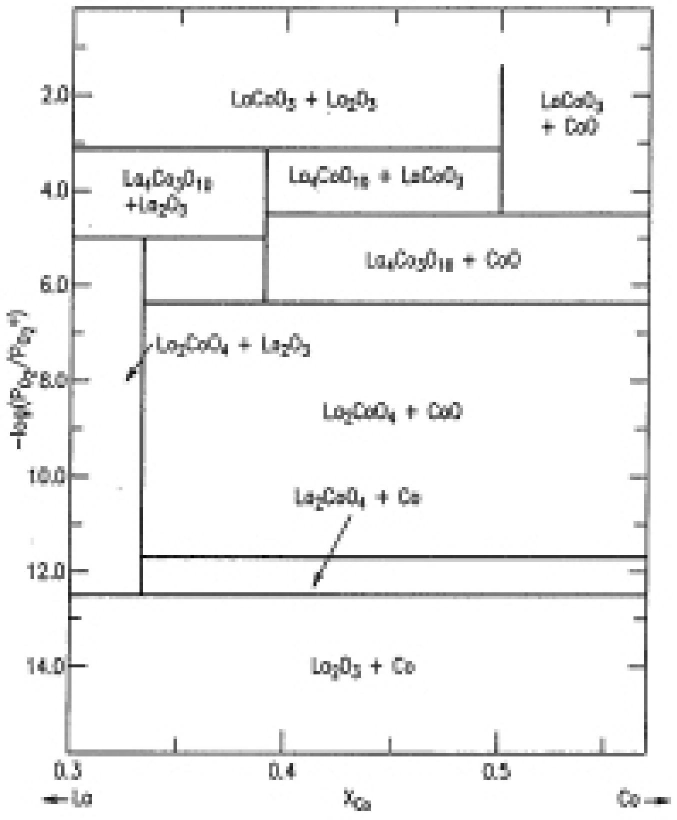

Figure 3.2: Ternary phase diagram of La-Co-O at 1100°. Different phases for different partial oxygen pressure,$P(O_2)$, and La/Co ratio are present. The decrease of the $P(O_2)$ leads to formation of $La_{1+n}Co_nO_{3n+1}$(taken from Ref. [87]).

lattice planes and the purity of the films. For the samples studied in this work the diffraction vector coincides with the normal direction of the substrate. For the so-called Θ-2Θ scans the detector is moved with the double step size (2Θ) of the sample step size (Θ). The distance d_{hkl} is determined with the aid of the Bragg equation. For systems with cubic or orthorhombic unit cells the relation between the lattice parameters a, b, c and the d_{hkl} is given by $d_{hkl} = [(h/a)^2 + (k/b)^2 + (l/c)^2]^{-\frac{1}{2}}$. In the special case of (001) oriented films only (00l) reflexes with $1 < l < 4$ are measured. By using the equation $d_{hkl} = c/l$ the lattice parameter can be calculated. In order to determine the in-plane lattice parameters of the samples, a 4-circle X-ray diffractometer is used, where asymmetric Bragg-reflections can be detected. The measure of the quality of the epitaxy is the mosaic spread of the crystallites, which can be determined by means of an ω-scan, or a so-called rocking curve. By this, the detector is adjusted to a fixed angle 2Θ, while the angle ω is varied. The full width at half maximum (FWHM) is a parameter indicating the mosaic spread of the film. We show a $\Theta - 2\Theta$ scan of a (001) oriented LCO film grown on LSAT substrate in Fig. 3.3a, which demonstrates (001) oriented growth and purity. The performed rocking curve revealed the mosaic spread with $\Delta\omega \approx 0.05$. The measured c lattice parameter is equal to 3.78Å. In Fig. 3.3b we show

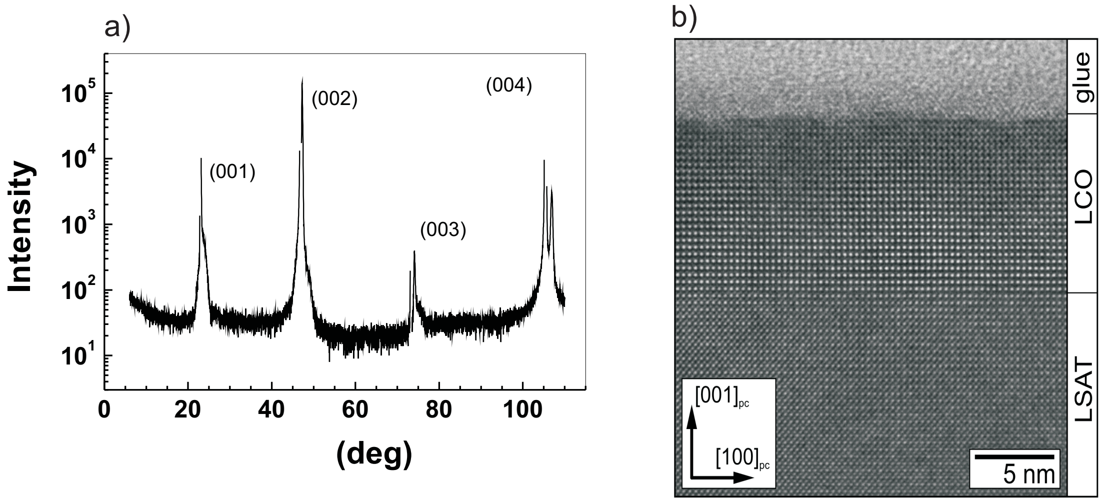

Figure 3.3: a) A $\Theta-2\Theta$ scan of a 50 nm thick (001) oriented LCO/LSAT film, and extracted values are: $\Delta\omega \approx 0.05$,c$\approx$3.78Å. b) A cross-section TEM image of a 10 nm thick film.

also a cross-sectional TEM image taken at Laboratorium für Elektronenmikroskopie (LEM) , where it can be seen that the film has high interface quality.

Thickness determination

A wet-chemical process is applied to prepare the films for thickness measurements. Half of the film is covered by a resistant lacquer, and subsequently the sample is immersed in dilute hydrochloric acid. The part of the film which is not covered by lacquer is etched away, and afterwards the lacquer is removed by dissolving it in acetone. The obtained step is investigated by a profilometer with a resolution up to 10 nm (Dektak 3) to deduce the thickness of the film. Since the film thickness is proportional to the number of laser shots during the deposition, one can determine the deposited thickness per shot, i.e, the deposition rate, R.

3.2 Tuning of strain

The high sensitivity of the magnetization of LCO to strain motivates the present work. It has been shown that different possible spin states of the perovskite LCO [8, 56] are very sensitive to variations of the Co-O bond length and the Co-O-Co bonding angle because of the subtle balance between the crystal field splitting, Δ_{CF}, and the intra-atomic exchange energy, J_{EX} [14]. An increase of the Co-O bond length leads to, for example, a decrease of Δ_{CF} and thus can cause an increased population of higher spin states. A promising way to change the Co-O bonding length is the heteroepitaxial growth of LCO thin films on different single-crystal substrate materials. Different in-plane lattice parameters of the substrates affect the epitaxial strain and thus may affect the bonding lengths and bonding angles of the film material, which,

Table 3.1: In-plane lattice parameters of the used substrate materials, a_s, and the corresponding lattice mismatch, $\epsilon = (a_s - a_b)/a_b$, to $LaCoO_3$ at room temperature. a_b corresponds to the pseudocubic bulk lattice parameter of LCO, and a_b=3.82Å.

Substrate	Orientation	Abbreviation	a_s(Å)	ϵ(%)
$SrLaAlO_4$	(001)	SLAO	3.75	-1.31
$LaAlO_3$	(001)	LAO	3.78	-0.52
$SrLaGaO_4$	(001)	SLGO	3.84	$+1.05$
$(LaAlO_3)_{0.3}(Sr_2AlTaO_6)_{0.7}$	(001)/(110)/(111)	LSAT	3.87	$+1.84$
$SrTiO_3$	(001)	STO	3.90	$+2.63$

in turn, changes the magnetic properties. For that reason, we have investigated epitaxial growth of LCO on various substrates. Beside the prerequisites for epitaxial growth such as chemical stability, the approximate lattice matching and the matching of the thermal expansion coefficient, we additionally required the feasibility of a 'cube on cube growth' of LCO on the substrate material, i.e., a-axes and b-axes of the substrate and LCO film material are parallel to each other. Furthermore, because of the pseudo-cubic structure of perovskites the substrate material should have a square-shaped surface cell. We have chosen the following suitable and commercially available substrate materials: (001) oriented $SrLaAlO_4$ (SLAO), $LaAlO_3$ (LAO), $SrLaGaO_4$ (SLGO), $(LaAlO_3)_{0.3}(Sr_2AlTaO_6)_{0.7}$ (LSAT), and $SrTiO_3$ (STO). The in-plane lattice parameters, a_s and b_s, of the substrate materials and the corresponding lattice mismatch to bulk LCO, $\epsilon = (a_s - a_b)/a_b$ (b=bulk), where a_b=3.82Å is the pseudo-cubic bulk lattice parameter of LCO [24], are listed in Table 3.1. The lattice mismatch ranges from $\epsilon = -1.31\%$ for SLAO to $\epsilon = +2.63\%$ for STO. It indicates that, in principle, we can grow tensile and compressive strained epitaxial films. For tensile strain, the in-plane film lattice parameter, a_f, is larger than that of bulk, a_b, whereas in the case of compressive strain $a_f < a_b$. The growth parameters were adopted from a previous optimization of LCO on LSAT [15].

It is well known that strain relaxes in heteroepitaxial systems with increasing thickness, generally by misfit dislocations [89, 90]. However, below the so called critical film thickness, the film growth is coherent and pseudomorphic with respect to the surface structure of the substrate. Therefore, the film thickness was adjusted with respect to the critical thickness, in order to achieve nearly homogeneously strained films. In Fig. 3.4 rocking curves for two LCO films grown on LSAT with different thicknesses, $t = 15$nm and $t = 50$nm are shown. For the central part of the peak at $\omega \approx 23.6°$ the [001] film direction is exactly parallel to the [001] direction of the substrate so that the narrow part can be attributed to the pseudomorphic part of the film. The broadened part of the peak is likely due to a partial relaxation of the film. Our group has shown that strain in epitaxial LCO films, up to a thickness of $t \leq 100$ nm, is predominantly relieved elastically by nanotwinning [24]. An integration of the decomposed rocking curves allows us to estimate the volume fraction of the strained pseudomorphic part of the film, which is proportional to the area of the central peak, and that of the relaxed part, which is proportional to the area of the broadened peak. The volume fraction of

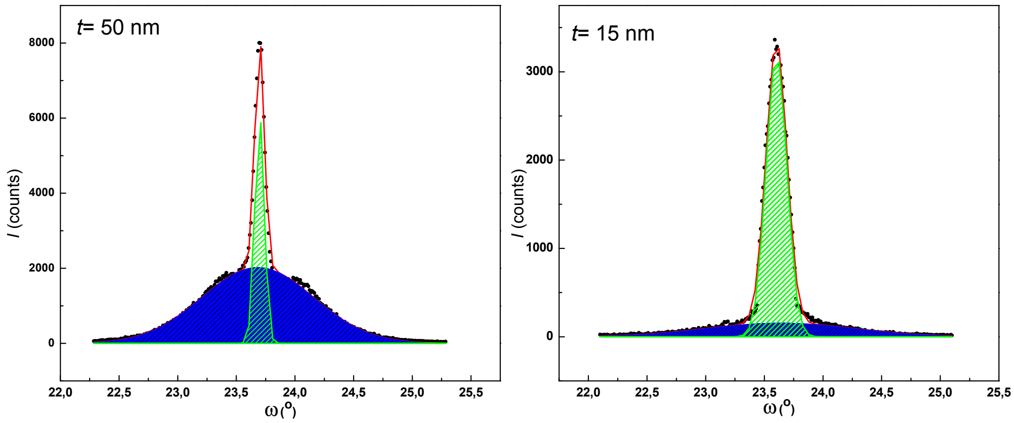

Figure 3.4: Rocking curves of a thin (t=50 nm) and a thinner (t=15 nm) LCO film grown on LSAT substrate The central part of the peak (dashed green) is caused by the pseudomorphic fraction of the LCO film, while the broadened part (dashed blue) is due to the partially relaxed part of the film. The volume fraction of the pseudomorphic grown part is about 75% for the thinner film. It drops to 20% for the thicker one.

the pseudomorphic part is 75% for the 15 nm thick film, while it is only 20% for the 50 nm thick film. Thus, the thickness of an epitaxial thin film with optimum strain homogeneity should be kept around 10 nm. Since the structural relaxation of the film is only small in the very beginning of strain relaxation, i.e., just above t_{cr}, we have grown the films with a thickness of about 25 nm, in order to increase the magnetic volume. Single-phase (001)-oriented 25 nm thick LCO films were grown successfully on all the substrate materials. All films showed a cube-on-cube growth on the single-crystal substrates. In Fig. 3.5, the lattice parameters and the cube root of the unit-cell volume, $V^{1/3} = (a \times b \times c)^{1/3}$, of the LCO films are displayed as a function of the in-plane lattice parameter a_s of the substrate material. As expected for an epitaxially tensile strained film, the in-plane lattice parameter a increases and the out-of-plane lattice parameter c decreases with increasing a_s, resulting in a pseudo-tetragonal structure. The tetragonal distortion, $\Delta = |a - c|/|a + c|$, is largest for the films on STO and LAO, i.e., 2.6% and 2.3%, respectively, and nearly negligible for the films on SLAO. However, deviations from nearly linear dependence of a and c on a_s are clearly present for films grown on SLAO and to some extent for films on STO. Films grown on SLAO seem to be strongly relaxed with a pseudo-cubic structure and the lattice parameters of $a \approx b \approx c \approx 3.82$Å. The reason for this relaxation is likely the high negative lattice mismatch ϵ. Moreover, growth on STO substrates results in the formation of macroscopic cracks in the films after deposition. The cracking is likely caused by structural relaxation and the relief of the tensile strain because of the large mismatch of $\epsilon = +2.63\%$. The unit-cell volume increases by about 3% with increasing a_s within the measured strain range. The elastic properties of the LCO films are shown in more detail in Fig. 3.6, where the out-of-plane lattice strain, $\epsilon_{zz} = (c - a_b)/a_b$, versus the in-plane strain, $\epsilon_{xx} = (a - a_b)/a_b$, is shown.

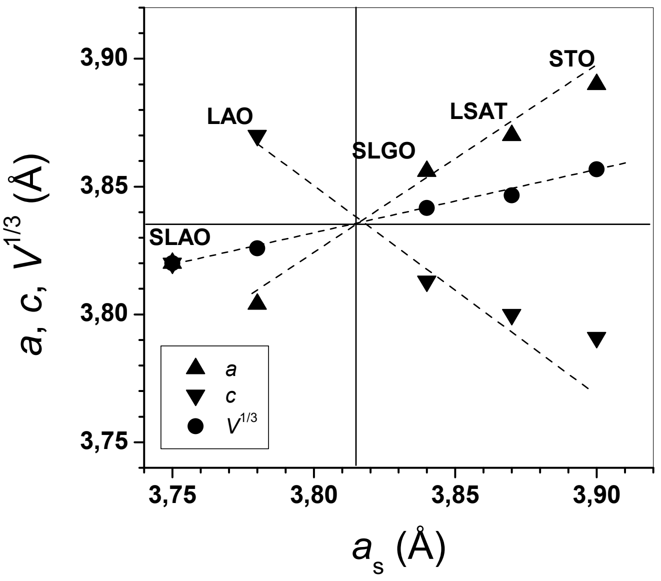

Figure 3.5: Lattice parameter a (up-triangles) and c (down-triangles) and the cube root of the unit-cell volume $V^{1/3}$ (circles) of the LCO films as a function of the lattice parameter a_s of the corresponding substrate material at room temperature. The dashed lines are guides to eye.

A linear fit to the data results in a slope of $\epsilon_{xx}/\epsilon_{zz} \approx -1$, yielding the Poisson ratio:

$$\nu = \frac{1}{1 - 2\frac{\epsilon_{xx}}{\epsilon_{zz}}} = \frac{1}{3} \tag{3.1}$$

The extracted value of $\nu \approx 1/3$ has been observed previously for epitaxially strained films of hole doped cobaltates [91], and for the manganites as well [92].

The nearly linear relation between ϵ_{xx} and ϵ_{zz} indicates an elastic coupling of the film to the substrate and therefore the possibility to tune the strain-dependent magnetic properties of epitaxial LCO films.

3.3 MOKE magnetometry and Kerr microscopy

3.3.1 Magneto-optical Kerr effect

In general, the magneto-optical Kerr effect (MOKE) is the change of polarization or ellipticity of a light beam reflected from a magnetic surface. The measured quantity, e.g., the rotation of the polarization, is a linear function of the magnetization of the magnetic material. Besides the Kerr effect [93, 94] the Faraday [95], the Voigt [96] and Cotton-Mutton effect [97] are counted to magneto-optical phenomena. Although all effects describe the change of the polarization or ellipticity of light, when it interacts with magnetic matter, they are named differently depending on the trajectory of

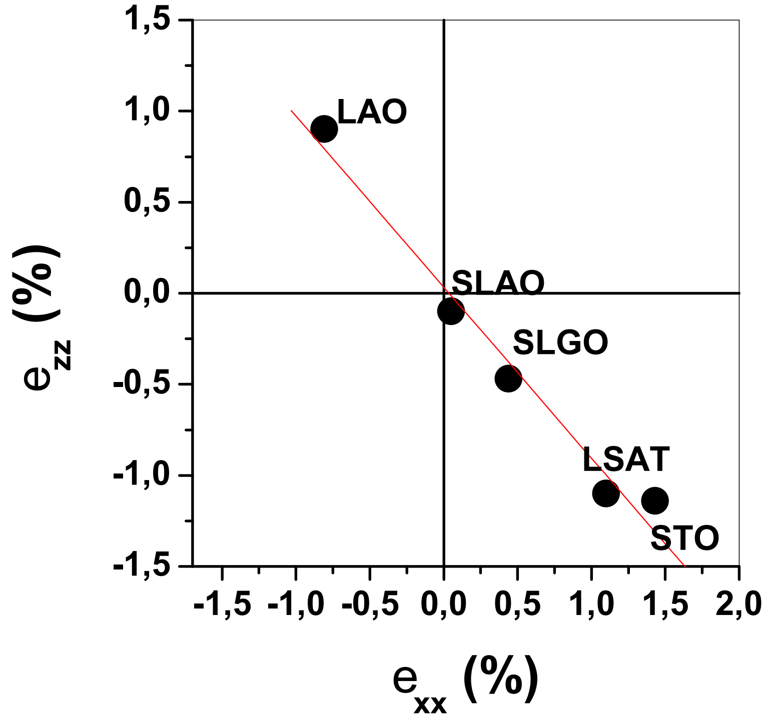

Figure 3.6: Out-of-plane lattice strain ϵ_{zz} versus in-plane lattice strain ϵ_{xx}. The solid line is a linear fit to the data points and reflects $\epsilon_{zz} \approx -\epsilon_{xx}$ which results in a Poisson ratio of $\nu \approx 1/3$.

the incident light and its direction with respect to the magnetization vector M of the sample. In particular, the Faraday and Voigt effect describe the change of the polarization/ellipticity of linearly polarized light when passing through a transparent medium. In the Faraday effect, the propagation of light is parallel to the external field H. To a first approximation, the Faraday effect is proportional to magnetization M. In the case of the Voigt effect, the direction of the magnetization vector is perpendicular to the propagation direction, and the effect is proportional M^2. The microscopic theory of the magneto-optical Kerr effect involves quantum theory. Hulme [98] proposed the first quantum description of the magneto-optical effect. He pointed out that the spin-orbit interaction that couples the electron spin to its motion is responsible for the large Faraday rotation in the ferromagnets. For example, the magnetic moment of ferromagnetic Fe, Co or Ni is caused by the splitting of the spin-up and spin-down subbands of the 3d bands. An incoming polarized light wave interacts through its electric field with the electrons, and changes their orbital momentum. Because of the spin-orbit interaction this results in an interaction between the electric field of the light wave and the magnetization. The incoming electromagnetic wave can be split into left- and right-handed circular eigenmodes, which have different quantum-mechanical probabilities to excite spin-up or spin-down electrons near the Fermi level. The excited electrons

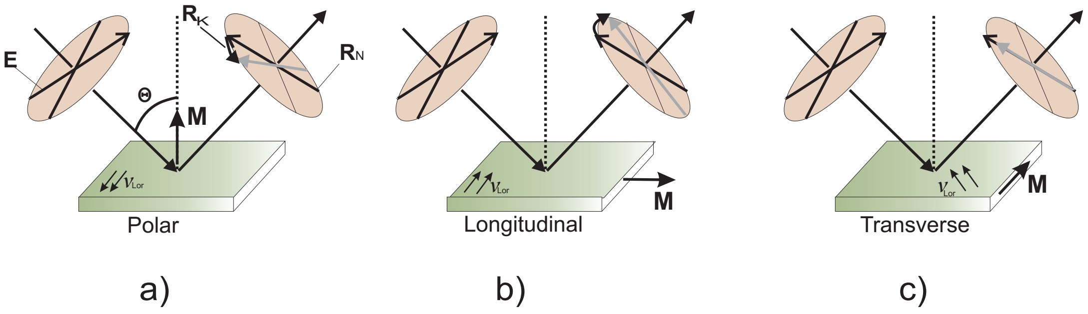

Figure 3.7: The polar (a), the longitudinal (b) and the transverse (c) magneto-optical Kerr effect. R_N is the regularly reflected electric field amplitude. The magneto-optical amplitude R_K can be conceived of as being generated by the Lorentz motion v_{Lor}.

will emit electromagnetic waves with different circular polarization depending on the their spin state. Thus, calculation of the magneto-optical effects from first principles is a complicated task [99–102]. The macroscopic description of the Kerr effect can be comprehended considering the Lorentz force on oscillating electrons in the presence of a magnetic field. Compared to the quantum-mechanical description, the classical description is quite simple and useful for both understanding and mathematical calculations. The simplest description of MOKE is to consider a Lorentz-Drude model of a metallic film. The incident light wave causes the electrons in the metal to oscillate parallel to the plane of polarization. In the absence of any magnetization the reflected light is polarized in the same plane as the incident light, this is the regular component with an amplitude R_N. If a magnetization is thought to be acting on the oscillating electrons like an internal magnetic field, the electrons exhibit a second motion due to the Lorentz force. This second component is perpendicular to both the direction of the magnetization and the primary motion. The second component generates a second amplitude called the Kerr amplitude, R_K, for reflection. The superposition of R_N with R_K leads to a magnetization-dependent rotation of incident polarization plane. Moreover, if the two amplitudes are not in phase, ellipticity is introduced to the reflected light. In this framework one can understand easily three general geometries of the magneto-optical Kerr effect, which are displayed in Fig. 3.7.

a) In the polar geometry the magnetization is perpendicular to the reflecting surface plane. This effect is strongest for perpendicular incidence, since the Kerr amplitude is proportional to the cosine of incident angle and shows a maximum at $\Theta = 0$. In addition, the effect is independent on the direction of the polarization for $\Theta_0 = 0$.

b) In the longitudinal configuration the magnetization is parallel to plane of incidence and reflecting surface plane.The Kerr amplitude vanishes for $\Theta_0 = 0$ and is proportional to the sine of the incident angle, $R_K \approx \sin\Theta_0$.

c) For the transverse configuration the magnetization is oriented perpendicular to the plane of incidence and parallel to the surface. For polarized light a Kerr amplitude will be generated in the direction of the regularly reflected beam, causing only an amplitude variation of the light, but no Kerr rotation.

The three cases can be combined to yield a formula of the Kerr effect for an arbitrary magnetization and polarization of the electromagnetic wave.

3.3.2 Mathematical description of the Kerr effect

The classical description of the Kerr effect is based on an analysis of the dielectric properties of the medium, specifically the dielectric and conductivity tensors. They depend on the magnetic field and/or magnetic state of the material and it is precisely their character that gives rise to magneto-optical effects. The present approach relates the Kerr rotation and the Kerr ellipticity to the dielectric tensor. The goal of the electro-magnetic treatment is to generalize the magneto-optical Fresnel reflection coefficients. We will consider a situation depicted in Fig. 3.8: A linearly polarized wave is incident on the surface of a magnetic material under the angle Θ_0. When a beam of light is incident from a non-magnetic medium 0 to a magnetic medium 1, having an arbitrary direction of the magnetization as shown in Fig. 3.8, the dielectric tensor ϵ can be generalized using Euler's equation as follows [103, 104]:

$$\epsilon = \epsilon_{xx} \begin{pmatrix} 1 & -iQm_z & iQm_y \\ iQm_z & 1 & -iQm_x \\ -iQm_y & iQm_x & 1 \end{pmatrix} \tag{3.2}$$

Here, m_i are the components of the magnetization vector $\mathbf{M}$ and the material constant Q is the magneto-optical constant, also called Voigt constant. Solving the Maxwell equations for the above dielectric tensor, the magneto-optical Fresnel reflection matrix can be given as follows [104]:

$$\hat{\mathfrak{R}} = \begin{pmatrix} \tilde{r}_{pp} & \tilde{r}_{ps} \\ \tilde{r}_{sp} & \tilde{r}_{ss} \end{pmatrix} \tag{3.3}$$

The reflectivity of any electromagnetic wave is given by the Fresnel coefficients that include all the optical properties of the reflecting material. The coefficients r_{ij} are the ratio of the incident (j) polarized electric field and the reflected (i) polarized electric field, and are given by [103–105]

$$\tilde{r}_{pp} = \frac{n_1 \cos\Theta_0 - n_0 \cos\Theta_1}{n_1 \cos\Theta_0 + n_0 \cos\Theta_1} - \frac{i2n_0 n_1 \cos\Theta_0 \sin\Theta_1 m_x Q}{n_1 \cos\Theta_0 + n_0 \cos\Theta_1} \tag{3.4}$$

$$\tilde{r}_{sp} = \frac{i n_0 n_1 \cos\Theta_0 (m_y \sin\Theta_1 + m_z \cos\Theta_1) Q}{(n_1 \cos\Theta_0 + n_0 \cos\Theta_1)(n_0 \cos\Theta_0 + n_1 \cos\Theta_1) \cos\Theta_1} \tag{3.5}$$

$$\tilde{r}_{ss} = \frac{n_0 \cos\Theta_0 - n_1 \cos\Theta_1}{n_0 \cos\Theta_0 + n_1 \cos\Theta_1} \tag{3.6}$$

$$\tilde{r}_{ps} = -\frac{i n_0 n_1 \cos\Theta_0 (m_y \sin\Theta_1 - m_z \cos\Theta_1) Q}{(n_1 \cos\Theta_0 + n_0 \cos\Theta_1)(n_0 \cos\Theta_0 + n_1 \cos\Theta_1) \cos\Theta_1} \tag{3.7}$$

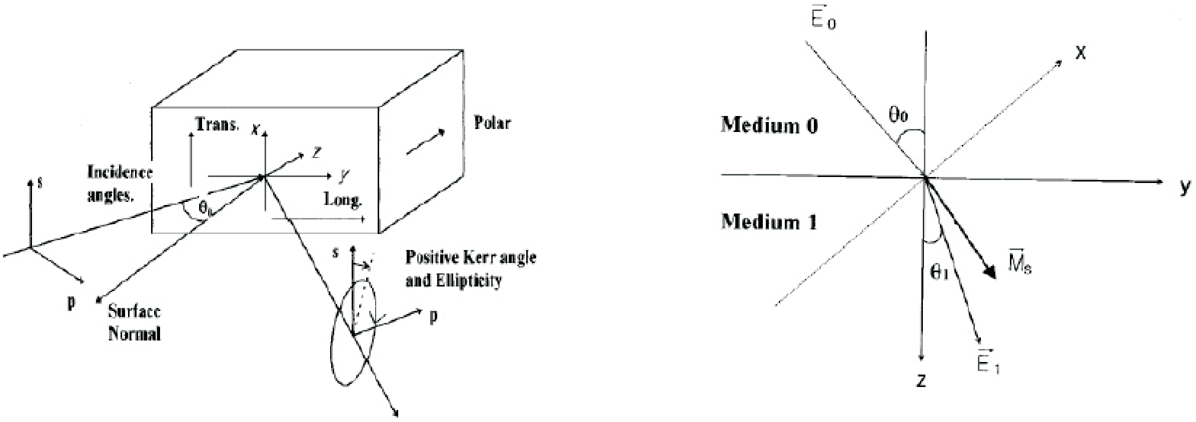

Figure 3.8: Schematic configuration for the polar, longitudinal, and transverse magneto-optical Kerr effects with respect to the coordinate system (left side). Coordinate system of the non-magnetic medium 0 and magnetic medium 1. The direction of the magnetization of medium 1 is arbitrary (right side).

In the above expressions, Θ_0, n_0 and n_1 are the angle of incidence, the refractive index of the non-magnetic medium 0, and that of the magnetic medium 1, respectively. The refractive angle Θ_1 in the magnetic medium 1 is determined by Snell's law. The complex Kerr effects are defined as following:

$$\tilde{\Theta}_K^p = \Theta_K^p + i\epsilon_K^p = \frac{\tilde{r}_{sp}}{\tilde{r}_{pp}} \tag{3.8}$$

$$\tilde{\Theta}_K^s = \Theta_K^s + i\epsilon_K^s = \frac{\tilde{r}_{ps}}{\tilde{r}_{ss}} \tag{3.9}$$

Here Θ_K and ϵ_K are the Kerr rotation and Kerr ellipticity, respectively, and the superscripts denote whether the incoming light is polarized in the p- or s-state. Using the above definitions, simplified formulas for different MOKE geometries can be derived.

In the polar configuration, $m_z = 1$ and $m_y = m_x = 0$. For the p-polarized light wave, by substituting Eqs. 3.4 and 3.5 in Eq. 3.8, the following relation is obtained:

$$\tilde{\Theta}_K^p = \left(\frac{\tilde{r}_{sp}}{\tilde{r}_{pp}}\right) = \frac{i n_0 n_1 \cos\Theta_0 Q}{(n_0\cos\Theta_0 + n_1\cos\Theta_1)(n_1\cos\Theta_0 - n_0\cos\Theta_1)} \tag{3.10}$$

By rearranging the equation and using Snell's law, a simplified expression for the polar MOKE effect can be expressed as :

$$\left(\tilde{\Theta}_K^p\right)^{pol.} = \frac{\cos\Theta_0}{\cos(\Theta_0+\Theta_1)} \cdot \frac{i n_0 n_1 Q}{(n_1^2 - n_0^2)} \tag{3.11}$$

In this expression, the second factor, $in_0n_1Q/(n_1^2 - n_0^2)$, is well-known as the polar Kerr effect for normal incidence [106]. For the oblique incident p-polarized wave, the Kerr effect can be described by a product of two factors. The prefactor, $\cos\Theta_0/[\cos(\Theta_0+\Theta_1)]$, is a simple function of the incident angle and the refractive angle determined by the refractive indices of the media. The second factor contains information about the magneto-optical properties of the medium 1. A similar expression can be derived for the s-polarized wave by following the same procedure:

$$\tilde{\Theta}_K^s = \frac{\tilde{r}_{ps}}{\tilde{r}_{ss}} = \frac{\cos\Theta_0}{\cos(\Theta_0 - \Theta_1)} \cdot \frac{in_0 n_1 Q}{(n_1^2 - n_0^2)} \tag{3.12}$$

The only difference between Eqs. 3.11 and 3.12 is the sign of the argument of the cosine function in the denominator of the prefactor.

In the longitudinal configuration, $m_y = 1$ and $m_x = m_z = 0$. By similar mathematical treatment of Eqs. 3.4-3.7, the complex Kerr effects for the longitudinal geometry can be expressed by

$$\left(\tilde{\Theta}_K^p\right)^{long} = \left(\frac{\tilde{r}_{sp}}{\tilde{r}_{pp}}\right)^{long} = \frac{\cos\Theta_0 \tan\Theta_1}{\cos(\Theta_0 + \Theta_1)} \cdot \frac{in_0 n_1 Q}{(n_1^2 - n_0^2)} \tag{3.13}$$

$$\left(\tilde{\Theta}_K^s\right)^{long} = \left(\frac{\tilde{r}_{ps}}{\tilde{r}_{ss}}\right)^{long} = -\frac{\cos\Theta_0 \tan\Theta_1}{\cos(\Theta_0 - \Theta_1)} \cdot \frac{in_0 n_1 Q}{(n_1^2 - n_0^2)} \tag{3.14}$$

The expressions for the longitudinal Kerr effects are also similar to those of the polar Kerr effects. The only difference between s- and p-polarized waves is again the sign of the argument of the cosine function. Although the expressions above were derived for the cases where the magnetization vector was aligned along certain directions, the Kerr effects in the general case of arbitrary magnetization direction and oblique incidence can be deduced. Since there is no contribution from the perpendicular component of the magnetization to the plane of incidence within first order of Q (transverse MOKE), the contribution for the arbitrary magnetization direction comes from the component parallel to the plane of incidence. Therefore, one can ignore m_x and consider only m_y and m_z.

$$\tilde{\Theta}_K^p = \frac{\tilde{r}_{sp}}{\tilde{r}_{pp}} = \frac{\cos\Theta_0(m_z + m_y \tan\Theta_1)}{\cos(\Theta_0 + \Theta_1)} \cdot \frac{in_0 n_1 Q}{(n_1^2 - n_0^2)} \tag{3.15}$$

$$\tilde{\Theta}_K^s = \frac{\tilde{r}_{ps}}{\tilde{r}_{ss}} = \frac{\cos\Theta_0(m_z - m_y \tan\Theta_1)}{\cos(\Theta_0 - \Theta_1)} \cdot \frac{in_0 n_1 Q}{(n_1^2 - n_0^2)} \tag{3.16}$$

The above equations are valid for a magnetic film whose thickness is comparable to the wavelength in the material, and the MOKE signal is independent of the thickness d_1. On the other hand, if the layer is thin and satisfies the condition $2\pi|n_1|d_1/\lambda \ll 1$, the MOKE signal is a function of d_1, and one has to take into account the reflection from substrate as well. A simplified formula for the case of a ultrathin film with an arbitrary magnetization direction on a non-magnetic substrate as depicted in Fig. 3.9, is given by [1]

$$\tilde{\Theta}_K^p = \frac{\cos\Theta_0}{\cos(\Theta_0 + \Theta_2)} \left(m_y \frac{\sin^2\Theta_1}{\sin\Theta_2} + m_z \cos\Theta_2\right) \frac{4\pi n_0 n_1^2 Q d_1}{\lambda(n_s^2 - n_0^2)} \tag{3.17}$$

---

[1] Different sign conventions are used in the literature. The discussion in this thesis follows the scheme proposed in [107].

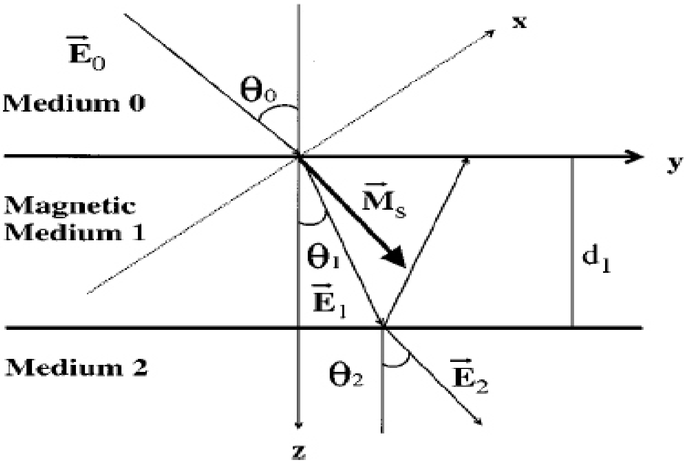

Figure 3.9: The coordinate system of the non-magnetic medium 0, the ultra thin magnetic medium 1, and the non-magnetic medium (substrate) 2. The thickness of the magnetic medium is *d*.

$$\tilde{\Theta}_K^s = \frac{\cos\Theta_0}{\cos(\Theta_0 - \Theta_2)}\left(m_y\frac{\sin^2\Theta_1}{\sin\Theta_2} - m_z\cos\Theta_2\right)\frac{4\pi n_0 n_1^2 Q d_1}{\lambda(n_s^2 - n_0^2)} \tag{3.18}$$

In the present study magnetic films are considered with a typical thickness of d_1 of 30-50 nm, for which the approximation of a thick film turned out to be satisfied. In Fig. 3.10 the Kerr rotation of s-polarized light is plotted for the polar and longitudinal configurations as a function of the incident angle using optical parameters of bulk Fe. The function for the longitudinal case ($m_y = 1$, $m_z = 0$) exhibits a maximum at $\Theta_0 = 55°$ whereas a maximum value is obtained for the polar configuration ($m_z = 1$, $m_y = 0$) at normal incidence, $\Theta_0 = 0°$. In our experimental situation the incident angle of 45° is designed in order to ensure the optimum sensitivity for both configurations. The typical longitudinal Kerr rotation obtained at $\Theta_0 = 45°$ for $LaCoO_3$ is around $\Theta_K^s = 0.03°$. The Kerr effect of LCO might be related to the different optical parameters and weaker magnetization compared to Fe for $\Theta_0 = 45°$.

3.3.3 Measurement set-up for MOKE

All magneto-optical measurements in this work have been performed in the longitudinal and polar MOKE configurations. As has been pointed out in Sec. 3.3.2 this means that the Kerr rotation, Θ_K, or ellipticity, ϵ_K, has to be detected. The signal of the MOKE is to a first-order approximation proportional to the component of the magnetization lying in the intersection of the plane of incidence and the sample surface. In the following the experimental method of this concept will be described. Furthermore, the construction of a Kerr microscope to visualize the magnetic structure of thin films will be introduced. The most common application of MOKE is to measure the hysteresis

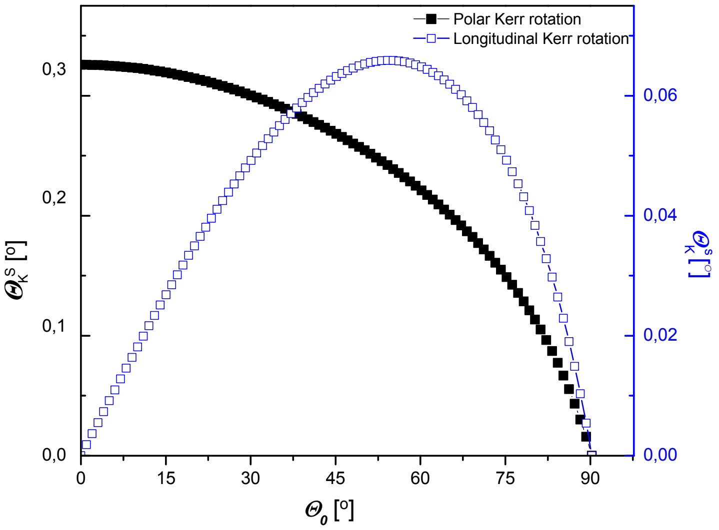

Figure 3.10: Plot of the polar (■) and longitudinal (□) Kerr rotations as a function of the incident angle Θ_0, as described in Eqs. 3.12 and 3.14, respectively, for Fe.

curves of a thin film as a function of the external magnetic field. One can deduce the in-plane and out-of-plane magnetic anisotropy by varying the orientation of the film with respect to the external field [108]. The magneto-optical measurement technique has advantages compared to other techniques probing magnetic properties. It is easy to use, non-destructive, fast and surface-sensitive, and thus suitable for thin and ultrathin films. It is possible to apply MOKE as a probe for the magnetization in thin films with a resolution of 10^{-8} emu. The setup and measurement algorithm is based on the work of Sato [109,110]. The detection scheme we use was previously applied by various other research groups [111–113]. Various techniques can be used to measure the magneto-optical Kerr effect. In this work polarization modulation technique is preferred by applying a photo-elastic modulator.

Mechanical alignment

Fig. 3.11 displays the geometry of the setup, which is mounted on an optical table to suppress external vibrations. A diode laser with a current and temperature controller is used to shine a polarized light at an angle, Θ_0, onto the sample. The sample is placed on the sample holder of the cryostat, which is commercially available and designed for magneto-optical measurement (Rectangular micro-tail He-cryostat, Oxford Instruments). It has four windows for optical access and can be operated between 4.2 K and 500 K. A base pressure of 10^{-6} mbar can be achieved. The cryostat is attached to a y-z translation stage, which enables the cryostat to move in both directions to an accuracy of 1 micrometer. This feature is exploited in the case of sample scanning measurements. The tail of the cryostat is located between the poles of an electromagnet system, which supplies in-plane and out-of-plane magnetic fields, with up to ±400

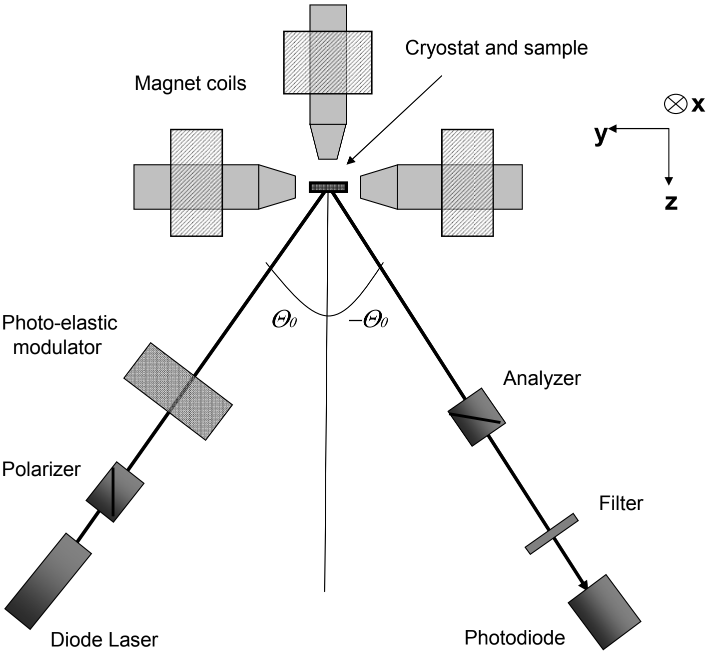

Figure 3.11: Schematic drawing of the MOKE magnetometry to measure polar and longitudinal Kerr effect.

mT for the in-plane geometry and about ±300 mT for the out-of-plane direction at the center of the sample.

Optical path

The light emitted from the diode laser ($\lambda = 658$ nm) is linearly polarized by a Glan-Thompson prism (Newport). The polarization of the laser beam is modulated by means of a photo-elastic modulator (PEM, Hinds I/FS 100) before it is reflected by the sample. A pin hole is also placed in the optical path to vary spot size when it is necessary. The reflected light passes through another Glan-Thompson prism (commonly called analyzer, same type as initial polarizer) prior to a photodiode detector. A band-pass filter blocking the daylight is attached at the entrance of the detector. It is avoided to use additional optical components (e.g., lenses and mirrors) between the polarizer and analyzer, which would introduce depolarization effects causing the decrease of the extinction ratio of polarizers. This effect is shown in Fig. 3.12. It is shown how the existence of the optical components between analyzer and polarizer leads to a deterioration of the extinction ratio. High extinction ratio is necessary to achieve high signal/noise (S/N) ratio, and contrast for MOKE magnetometry and Kerr microscopy, respectively. A photograph of the MOKE set-up is depicted in Fig. 3.13.

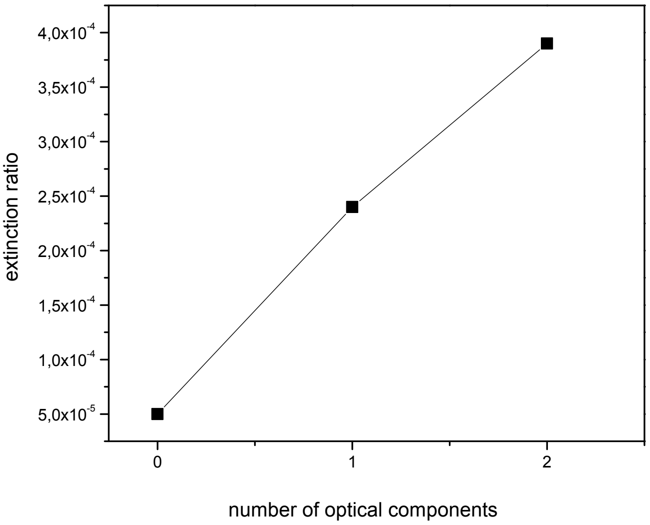

Figure 3.12: Extinction ratio of polarizers for additional optical components (in this case of a lens) placed between the polarizers.The extinction ratio is minumum for the nonexistence of any components between polarizer and analyzer.

Photo-elastic modulation

A photo-elastic modulator (PEM) consists of a birefringent crystal ($CaFe_2$ or, in our case, SiO_2), which is sinusoidally expanded and contracted in one direction by a piezoelectric actuator. Waves traveling parallel to this direction (y-axis) are retarded when the element is expanded, and advanced when it is contracted. Waves traveling orthogonally to that direction are not affected. In this way a relative phase difference, δ, between x and y components of the incident polarized plane wave is added (see Fig. 3.14).

$$\delta = \delta_0 \sin 2\pi f t \tag{3.19}$$

where δ_0 and f are the relative phase amplitude and the modulation frequency, respectively. The modulation frequency is typically 50 kHz. The incorporation of the PEM allows us to use a lock-in technique. This will be explained in the next section.

Measurement technique

The intensity of the reflected light at the detector can be analyzed using Jones-matrix formalism. In this method, every optical element is represented with matrices. A sequence of optical elements is expressed as the product of the representing Jones matrices [114]. By using Jones matrices of the incident light $\mathbf{E}_i = \begin{pmatrix} E_x \\ E_y \end{pmatrix}$, polarizer and analyzer

$$\mathbf{P}{=}\mathbf{A} = \begin{pmatrix} \cos^2 \Phi_{p(A)} & \sin \Phi_{p(A)} \cos \Phi_{p(A)} \\ sin\Phi_{p(A)} \cos \Phi_{p(A)} & \sin^2 \Phi_{p(A)} \end{pmatrix} \tag{3.20}$$

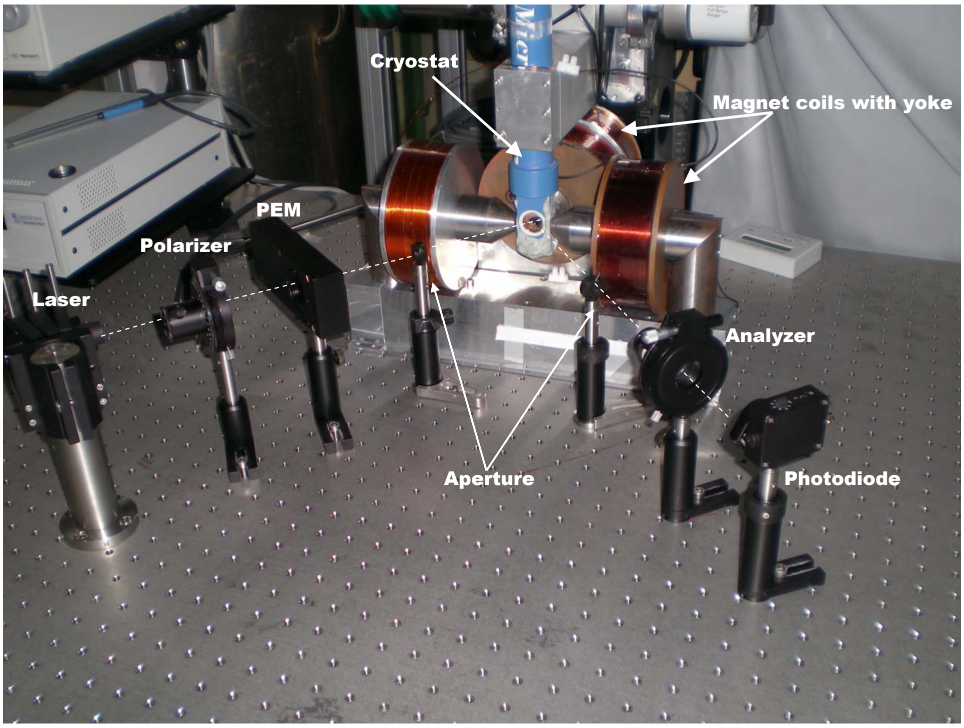

Figure 3.13: Photograph of the sample environment and the optical path of the MOKE magnetometry

with $\Phi_{P(A)}$ being the polarizer and analyzer angle, sample

$$\mathbf{S} = \begin{pmatrix} r_{pp} & r_{sp} \\ r_{ps} & r_{ss} \end{pmatrix} \tag{3.21}$$

and the modulator

$$\mathbf{M} = \begin{pmatrix} 1 & 0 \\ 0 & e^{i\delta} \end{pmatrix} \tag{3.22}$$

the electric field, $\mathbf{E}_f$, at the detector is equal to the product of matrices and given by

$$\mathbf{E}_f = \mathbf{A} \cdot \mathbf{S} \cdot \mathbf{M} \cdot \mathbf{P} \cdot \mathbf{E}_i \tag{3.23}$$

and the detected intensity at the detector for the configuration in Fig. 3.14:

$$I = \left| \begin{pmatrix} 0 & 0 \\ 0 & 1 \end{pmatrix} \begin{pmatrix} r_{pp} & r_{sp} \\ r_{ps} & r_{ss} \end{pmatrix} \begin{pmatrix} 1 & 0 \\ 0 & e^{i\delta} \end{pmatrix} \frac{1}{\sqrt{2}} \begin{pmatrix} 1 \\ 1 \end{pmatrix} \right|^2 \tag{3.24}$$

The intensity of the light at the detector can be written as

$$I = I(0) + I(\omega)\sin\omega t + I(2\omega)\sin 2\omega t + ... \tag{3.25}$$

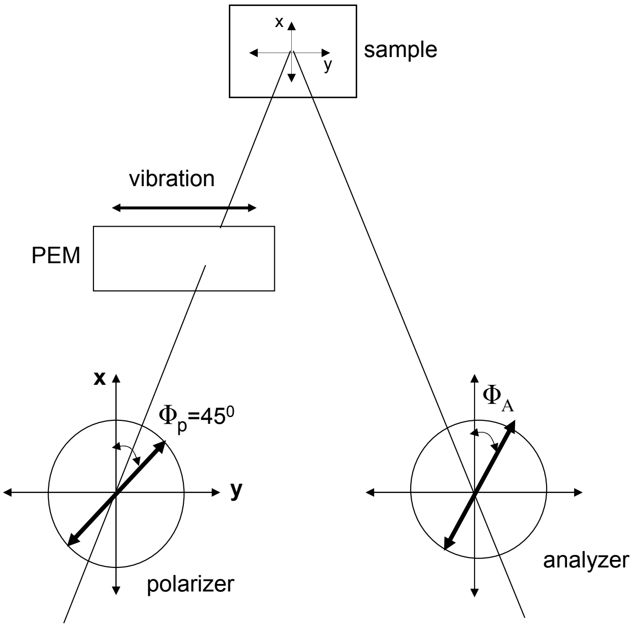

Figure 3.14: A schematic diagram showing the Kerr measurement arrangement with a photo-elastic modulator. The polarizing angle of the polarizer makes an angle $\Phi_p = 45°$ with the x-axis. A phase shift between two orthogonal components of linearly polarized light is caused by a photo-elastic modulator.

where $I(0)$, $I(\omega)$ and $I(2\omega)$ represent the zeroth (dc), first-order and second-order harmonics of the intensity, respectively. When we take the ratio of $I(\omega)/I(0)$ and $I(2\omega)/I(0)$ we obtain:

$$\frac{I(\omega)}{I(0)} = B\frac{4\epsilon_K J_1(\delta_0)}{(1 + J_0(\delta_0)\sin(2\Phi_A + 2\Theta_K))}$$

$$\frac{I(2\omega)}{I(0)} = A\frac{2J_2(\delta_0)\sin(\Phi_A + 2\Theta_K)}{(1 + J_0(\delta_0)\sin(2\Phi_A + 2\Theta_K))} \tag{3.26}$$

Here δ_0 is the phase amplitude introduced by PEM, which can be controlled by the electronic unit of PEM. J_0, J_1 and J_2 are the $0^{th}, 1^{st}$ and 2^{nd} order Bessel functions, respectively. A and B are the calibration constants. By setting $\delta_0 = 137.8°$ the zeroth order Bessel function is eliminated in Eq. 3.26, $J_0(137.8°) = 0$, which otherwise would have added only small contribution to the dc value of the signal. For $\Phi_A = 0°$ and $\sin(2\Theta_K) \approx 2\Theta_K$, it follows:

$$\frac{I(\omega)}{I(0)} = 4BJ_1(\delta_0)\epsilon_K$$

$$\frac{I(2\omega)}{I(0)} = 4AJ_2(\delta_0)\Theta_K \tag{3.27}$$

The first harmonic of the output signal normalized with the dc component is proportional to the Kerr ellipticity, while the normalized second harmonic is proportional to the Kerr rotation:

$$\begin{aligned} \epsilon_K &= \frac{1}{4BJ_1(\delta_0)}\frac{I(\omega)}{I(0)} \\ \Theta_K &= \frac{1}{4AJ_2(\delta_0)}\frac{I(2\omega)}{I(0)} \end{aligned} \tag{3.28}$$

When A and B are known one can determine Kerr rotation and ellipticity by measuring the three components of the intensity after the analyzer. The calibration constants are determined by calibration as described in the next section.

Data acquisition and calibration procedure

The necessary electronic connections and data acquisition scheme are given in Fig. 3.15. The high intensity stability of the laser is achieved by a diode laser driver and temperature controller (Newport, 505B). The temperature of the sample holder is

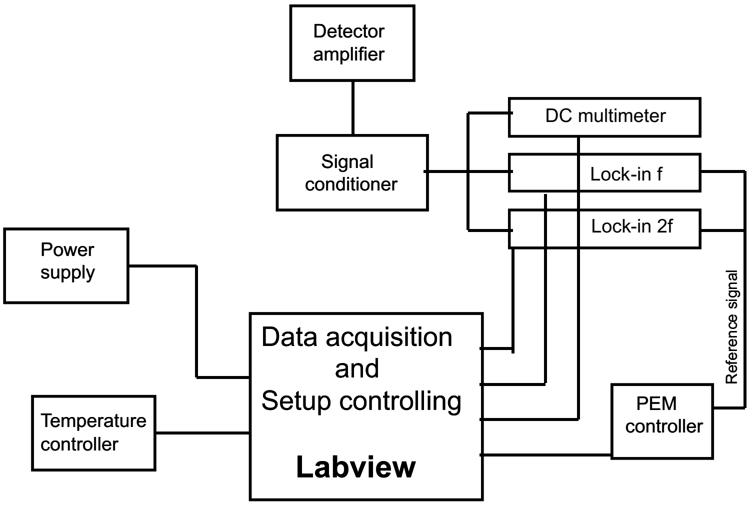

Figure 3.15: Electronic scheme of the MOKE setup. The signal is first amplified at the detector. This signal is fed to a signal conditioner, which is used to separate and amplify the AC and DC components of the signal. By means of lock-in technique the first and second harmonics of the signal are detected and normalized with the DC part. The detected signals are collected by a data acquisition program.

controlled by a temperature controller (Oxford Instruments, ITC 503S). The magnets are powered by a 400 Watt bipolar power supply (Kepco, BOP100-4). The strength and the sweeping rate of the magnetic field as well as the temperature of the cryostat can be varied by the measurement control programmed with Labview 7.0 graphical development system. The reflected light arrives at the Si-amplified detector (Thorlabs, PAD 100A-EC). The most optimized gain and bandwidth parameters of the detector are achieved at 30 dB setting. The detector signal output is connected to the signal conditioning unit (Hinds Instruments, SCU-100). This is a broad-band amplifier. The amplification factor of the DC signal and the AC signal can be set separately. Best results are obtained if the DC signal output of the signal conditioner is regulated to somewhere between 1 and 5V. The AC-signal output is connected to two lock-in amplifiers (Princeton Applied Research, EGG 5209, and Perkin Elmer, 7225), one for the f (ellipticity) and the other for the $2f$ component (rotation). In order to get rid of the laser beam noise and small intensity variations caused by the movement of the reflected beam, the AC signals have to be divided by the DC signals (see Eq. 3.27): the DC output of the signal conditioner is connected to the AUXin1 inputs on the rear side of the lock-in amplifiers. A typical time constant is set to 0.3 s for the conventional hysteresis loop measurements. Both lock-in amplifiers are connected via a GPIB cable to the data acquisition system. In order to measure the Kerr rotation and the Kerr ellipticity quantitatively, the constants of proportionality, A and B, are determined by a calibration procedure. In the case of rotation, calibration is done by rotating the analyzer from $\Phi_A = -2^\circ$ to $+2^\circ$ in steps of 1°, and the response $I(2\omega)/I(0)$ is monitored. A linear fit to measured signal as function of Φ_A yields the calibration factor. An example of calibration is depicted in Fig. 3.16. The calibration factor determination for ellipticity is accomplished in the same manner, but with the addition of a quarter-wave plate after the PEM in the optical path. Before every measurement the analyzer angle is needed to be set to zero ($\Phi_A = 0$) where the output $I(2\omega)/I(0) = 0$. The misalignment of the analyzer angle from the “real zero“ would cause an offset on the hysteresis loop. Further improvement of the S/N ratio can be achieved if one knows the origin of the noise sources. The main noise sources can be classified as electronic noise and “technical noise“. Electronic noise is mainly caused by the quality of the detector and associated amplifiers. It is independent of the light intensity at the detector, and can be minimized by optimized settings of detecting instruments. “Technical noise“ includes the laser output fluctuations, misalignment of the optical path, depolarization effects of optical components, and thermal drifts. Let us call f_{cycle} the acquisition frequency of the complete measurement cycle (hysteresis loop, typical range of 0.1-0.01 Hz) and f_{point} the acquisition frequency of a single data point, which must be below the cutoff frequency $f_{lock-in}$ of the lock-in amplifier (10-100 Hz). To maximize the S/N ratio one should exclude the noise in the range $[f_{cycle}, f_{point}]$ and around the demodulation frequency $2f$ (for Kerr rotation). The noise in the former range can be eliminated by changing data collection time and sweeping rate, while the latter can be improved by the settings of the lock-in amplifier. Moreover, averaging of individual loops is the best way to improve the S/N ratio. In our setup, we obtained an optimum S/N ratio of about 50:1 with a data collection time of 100 s and sweeping time of 0.5 s. The shift of hysteresis loops caused by thermal drifts can be corrected numerically after the data acquisition is completed. To demonstrate the

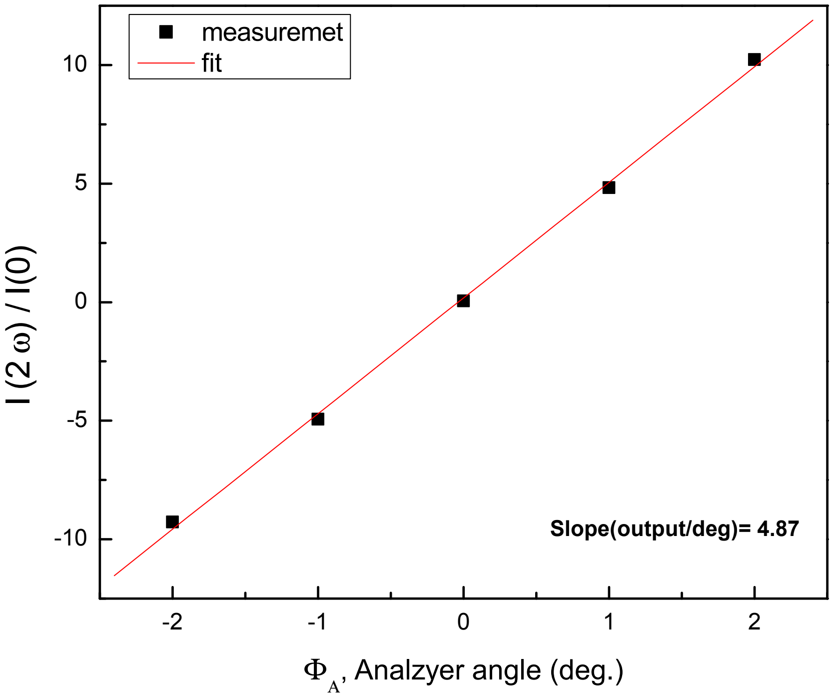

Figure 3.16: Calibration of the Kerr measurement system. The ratio of the second harmonic and the DC component of the detected signal is measured as function of the analyzer angle, around 0°. The slope of the linear fit is used as calibration factor for the Kerr rotation.

functionality of the measurement setup, typical measurements are presented in Fig. 3.17 which shows a Kerr rotation loop for a LCO film on LSAT and a thin (12Å) Co film on Pt. The measured polar Kerr rotation for the Co/Pt sample is higher than the longitudinal Kerr rotation of the LCO/LSAT sample. Furthermore, differences in the coercive field (H_c) and remnant magnetization, M_r, as well as the shape of the magnetization reversal loops are clearly present.

3.3.4 Measurement set-up for Kerr microscopy

Although there are plenty of different magnetic domain imaging techniques, Kerr microscopy still has unbeatable advantages. The method is based on the magneto-optical Kerr effect as described in section 3.3.2. When a linearly polarized light illuminates two domains with opposite magnetization, the Kerr rotation of reflected light will differ in sign for two domains. By means of an analyzer, in an optical microscope, this rotation difference is converted into a (in general weak) domain contrast that can be enhanced by digital image processing [115]. Kerr microscopy is one of the most versatile and flexible imaging techniques.

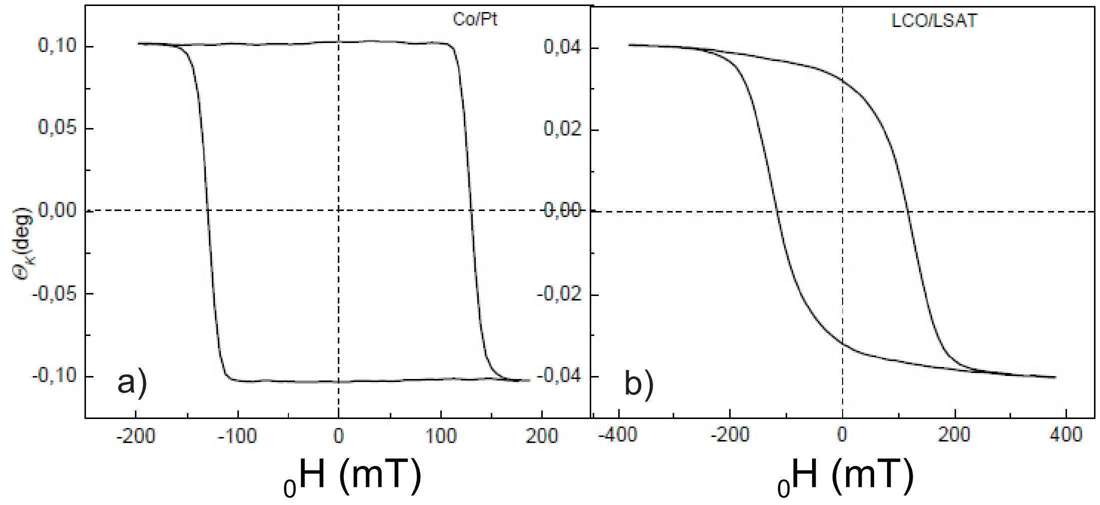

Figure 3.17: Hysteresis loops for two different samples. a) Co(12Å) film on Pt substrate. The measurement was taken at 150 K by applying the external field along the out-of-plane direction (polar configuration). b) $LaCoO_3$ (50nm) thin film on LSAT substrate. The loop was recorded at 55 K with the external field along the in-plane direction (longitudinal configuration).

Illumination path

The scheme of our home-made Kerr microscope is depicted in Fig. 3.18. There are different types of Kerr microscopes realized by different groups, which differ in selection of the light source, illumination path and image recording [116–120]. In our system a high-pressure mercury lamp is used as a light source. It offers sufficient brightness (Osram HBO 100W; luminance 220000 cd/cm^2) and a wide emission spectrum. The superior features of the power supply and the housing of the mercury lamp remove the instability of the lamp intensity (LOT-Oriel, Research Light Source-100-500W). A high-quality aspherical condenser lens (LOT-Oriel, Aspehricon©) is placed after the lamp in order to collimate the rays. Further optical components in the incident-light path include a heat-reflection filter to avoid heat load on other optical components and the sample, an edge filter to select the yellow and green lines in the spectrum with a maximum at 546 nm. The collimated light is focused onto the sample by a long-focal length aspherical lens (Melles-Griot) before it is polarized by means of a sheet polarizer (Codixx). In order to enhance the contrast again it is avoided to place any lens or mirror between the polarizer and analyzer. The illuminating aperture in a Kerr microscope should be neither too small nor too large. Too small an aperture (parallel light) leads to disturbing diffraction fringes especially around sharp defects on the sample surface. A large aperture reduces the contrast by generating a background intensity because of depolarization effects [121]. For the latter case, the zone of maximum extinction is in general cross-shaped (conoscopical image) in the full aperture. To obtain best contrast conditions, the illumination should be restricted to the extinction zone in the conoscopical image. For the polar effect, a central circular diaphragm is placed in the

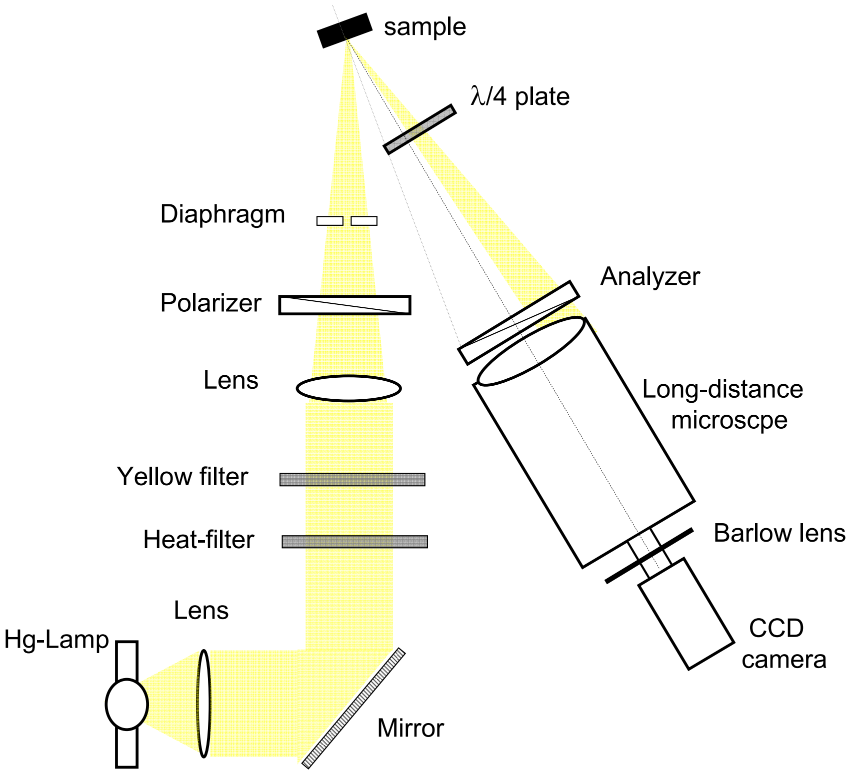

Figure 3.18: Schematic diagram of the Kerr microscope. The inclination of the sample surface normal with respect to the microscope optical axis is kept as small as possible whereas the incident angle of the light as large as possible. The working distance of the microscope is 15 cm.

illuminating beam. For the longitudinal effect, a displaced slit aperture oriented parallel to the plane of incidence is preferable [122]. An additional quarter-wave plate can be placed in the illumination path in order to eliminate ellipticities caused by the window of the cryostat and the metallic reflection from the sample surface. The domain imaging is based on a Questar QM-100 long-distance microscope coupled to a Andor electron-multiplied CCD camera (EMCCD). The QM-100 in our configuration is positioned at the optimum working distance of 15 cm and yields a nominal magnification of 10 that images a 0.5 mm field of view at the sample on the CCD detector. Barlow lenses (x2 or x3) placed between the microscope and the CCD camera are used to expand the image. The resolution of the Kerr microscope is determined by the resolution of the long-distance microscope, which is given by

$$d_{min} = 0.61 \frac{\lambda}{NA} \tag{3.29}$$

For the given numerical aperture (NA) at 15 cm working distance and a wavelength of λ=546 nm, it amounts to d_{min}=2 μm. The actual experimental resolution of the Kerr microscope is probably reduced due to the presence of non-perfect extinction and

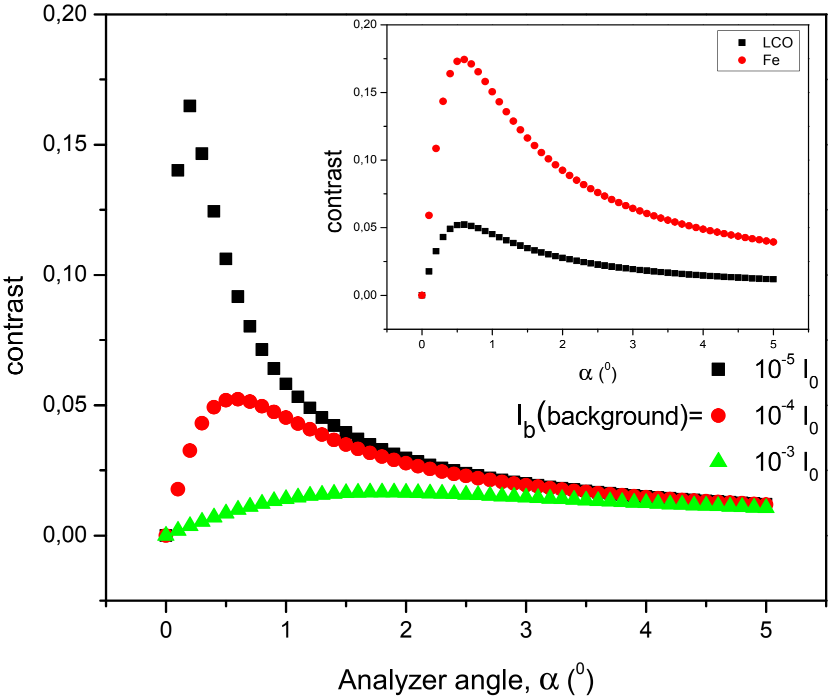

Figure 3.19: Calculated contrast values for a 50-nm thin LCO film in longitudinal Kerr microscopy as a function of the analyzer angle α (for $\alpha = 0$, analyzer is set at extinction). It is seen that maximum in contrast occurs at a finite value of α due to a certain amount of background light, I_b, that enters the microscope. Notice that, as I_b approaches 0, the maximum contrast angle comes close to the extinction point, $\alpha = 0$. Moreover, the maximum contrast decreases dramatically as I_b increases. Inset: Calculated longitudinal Kerr-microscopy contrasts for Fe and LCO thin films for I_b=$10^{-4}I_0$.

“technical noise“. It is important to note that the surface normal of the sample should be aligned with the microscope axis to provide sharp imaging of all areas within the field of view (0.5 mm). The depth of focus is given by $t \approx 0.5\lambda/(NA)^2$ and it amounts to t=8 μm. Hence, for sharp imaging, the inclination of the surface normal with respect to the microscope must not be larger than 1°. However, this is not realistic for an optimized longitudinal Kerr microscope configuration, where the incidence angle of light on the sample is $\Theta_0 = 45°$. If we set the inclination angle <1° and microscope distance 15 cm, there would be no reflected light falling onto the aperture of the QM-100. With respect to resolution and contrast, we optimized the incident angle Θ_0 to 20° and the inclination of the surface to 5° for imaging. The longitudinal Kerr effect is reduced due to the decreased incident angle, which leads to reduction of the contrast (see Fig. 3.10). A photograph of the Kerr microscope is shown in Fig. 3.20.

Signal-to-noise ratio and contrast

The magneto-optical Kerr signal, S, is defined as the change of the detector signal due to the Kerr rotation of the polarization, Θ_K. For the simple polarizer/photodiode scheme (conventional MOKE), $S = I_0 \left(\sin^2(\alpha + \Theta_K) - \sin^2(\alpha)\right) \approx 2I_0\alpha\Theta_K$, with I_0 the light intensity and α the angle between the direction of the extinction and the analyzer. Here it is assumed that the angles α and Θ_K are small ($\sin\alpha \approx \alpha$) and that the polarization angle is real (It is assumed that there is no ellipticity). However, by adding a quarter-wave plate we can eliminate the ellipticity. If we assume an ideal experimental setup, i.e., neither intensity fluctuations of the light source, mechanical instabilities, nor amplifier noise, then the noise, N, is given by:$N \propto \sqrt{I_0 \sin^2(\alpha)} \approx \sqrt{I_0}\alpha$. Thus, one gets

$$\frac{S}{N} \propto \sqrt{I_0}\Theta_K \tag{3.30}$$

For small analyzer angles, α, the S/N ratio is nearly independent of α but linear in Θ_K. The term $\sqrt{I_0}\Theta_K$ is the so-called figure of merit. As a result, the S/N ratio is most effectively enhanced by increasing the magneto-optical Kerr effect, Θ_K, e.g., by optimizing the geometry. For Kerr microscopy, however, it is not the S/N ratio alone that should be maximized but also the magneto-optical contrast in the images. If domains with magnetizations M and $-M$, are imaged, then the contrast is defined as $c = (I(M) - I(-M)) / (I(M) + I(-M))$ where $I(M)$ and $I(-M)$ are the detected intensities for two domains of opposite magnetization direction. With an ideal analyzer placed between the sample and the optical microscope the contrast is:

$$c = \frac{\sin(2\alpha)\Theta_K}{\sin^2\alpha + \Theta_K^2\cos^2\alpha + \frac{I_b}{I_0}} \tag{3.31}$$

In a realistic setup a maximum in the contrast occurs at some finite value of α. This is because the extinction ratios of polarizer and analyzer are finite and some stray light (due to the reasons given below) also enters the microscope, and additionally, a final background intensity, I_b, has to be considered. In Fig. 3.19, we simulated the contrast of the longitudinal Kerr rotation of two opposite magnetic domains in a LCO thin film ($\Theta_K = 0.03°$) as a function of the analyzer angle for different background contributions. It can be seen that a maximum in the contrast occurs at a finite analyzer angle, which is slightly away from the extinction position. It is also important to notice that, as the background intensity increases, the contrast decreases dramatically, and the angle giving the maximum increases. If we assume the background intensity between $10^{-3}I_0$ and $10^{-4}I_0$, the optimized analyzer angle would be $\alpha \approx 1°$. This result suggests that suppression of “unwanted“ light is crucial in order to obtain high contrast. The intensity of this spurious light is determined by the following factors:

(1) Elliptical polarization by metallic reflection.

(2) An elliptical polarization resulting from Kerr effect.

(3) The Kerr rotation is a function of incidence, and therefore, the polarization of different rays will be rotated by different amounts, so that the analyzer can not be set at extinction at all.

(4) The polarizer and analyzer are not perfect. For example, crossed sheet polarizers will let through one part per 10000 of the total intensity.

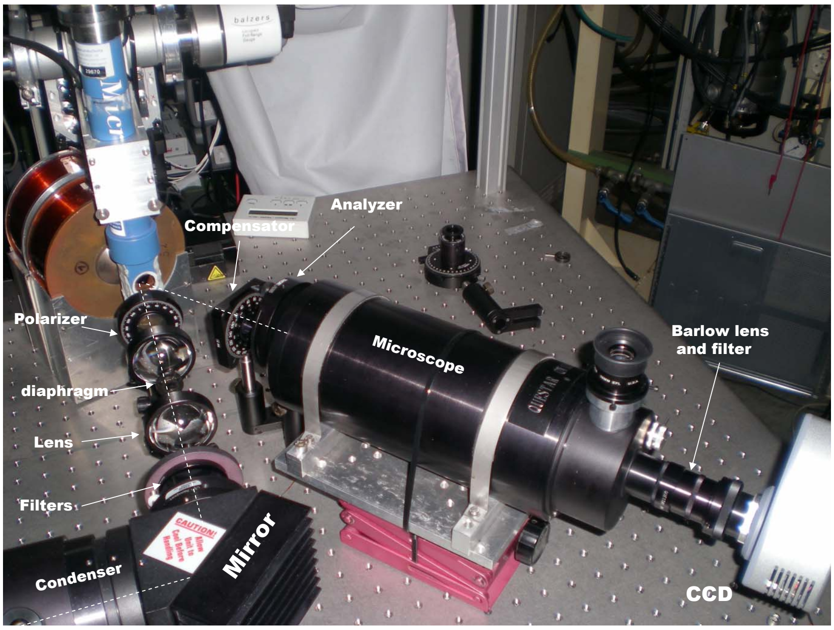

Figure 3.20: Photograph of the Kerr microscope. Highly divergent light from a Hg lamp is collimated by a condenser lens and directed onto the sample plane. A couple of filters are assigned to select the green-yellow spectrum and to reflect the heat. A pair of aspherical lenses with an iris diaphragm placed at the focal point are used to focus the light on the sample. The reflected light reaches the microscope objective through a quarter-wave plate and analyzer. A 3x Barlow lens and a bandpass filter are located between the CCD camera and the microscope.

(5) If the light is not monochromatic ($\lambda = 546 \pm 40nm$), there will be a small dispersion of the Kerr rotation, affecting the contrast in a manner similar to factor (3).
(6) Multiple reflections from surfaces of optical components and the sample, and scattering of light at the edges of stops, will cause some depolarization of the light.
Factors (4)-(6) can be minimized by good design and usage of high-quality optical components. Factor (2) can be eliminated by placing a quarter-wave plate (compensator) in front of the analyzer, while factor (3) and (1) can be reduced by an optimized illumination of the sample (uniform, optimized illumination aperture. A vertical slit can be used for longitudinal Kerr microscopy) [122]. In practice, the polarizer can be left fixed and compensator and analyzer are adjusted “simultaneously“ until an image of satisfactory contrast and brightness is obtained.

Digital contrast enhancement and image processing

As the Kerr effect is weak, polarization effects from imperfect surfaces, showing up at nearly crossed polarizers, can strongly obscure the magnetic image. The magnetic contrast can be enhanced digitally [123–126]. In the standard procedure, a digitized video image of the magnetically saturated state is first stored in a digital memory as reference image, and this domain-free image is subtracted from the pictures containing magnetic contrasts. In this way, contrast caused by the morphology of the surface is eliminated and in the difference image a clear micrograph of the domain pattern is obtained. It is advantageous that this subtraction process is performed in ”real time” at video frequencies. Live observation of magnetization processes is possible, as long as the microscope settings remain unchanged, because the reference image can be used for each of the incoming images. For recording, the resulting difference image can be improved by averaging and increasing the exposure time of video capturing. A high optical, mechanical, electrical and thermal stability of the microscope system is necessary. An image of LCO film on LSAT substrate taken by the Kerr microscope at 35 K is shown in Fig. 3.21. The film was cooled down from room temperature to the target temperature in zero field, and when the temperature was stable, a magnetic field of 0.3 T was applied parallel to the film plane. An image of magnetically saturated state was taken and stored as the background image. Afterwards, the field was switched off and the Kerr images were recorded in real time, from which the background image was subtracted continually as explained above. The displayed image in Fig. 3.21 is the average of 10 individual images captured within the 0.1 s exposure time of CCD. It can be seen that there is a stripe-like structure with different contrast, which might be attributed to the different direction of the magnetization in the stripes. Unfortunately, due to the small Kerr rotation of LCO film and the longitudinal configuration, the magnetic contrast and the sharpness are not good enough to conduct a magnetic domain structure study of LCO thin films by using built Kerr microscope. However, a study of FeCr film proved the proper functionality of the apparatus. The Kerr microscope is suitable for the future study of magnetic domain structures of strong in-plane materials such as Co and Permalloy thin films.

3.4 Complementary techniques for magnetometry

In this study, apart from the MOKE, other complementary magnetic measurement techniques, such as superconducting quantum interference device (SQUID) and torque magnetometry, were used. In the following, principles of those techniques are described.

3.4.1 SQUID magnetometry

SQUID magnetometry is one of the most effective and sensitive ways of measuring magnetic properties. In particular, it is a method which allows to directly determine the overall magnetic moment of a sample in absolute units. A SQUID magnetometer of the type Quantum Design MPMS-XL (Magnetic Properties Measurement System) was used to study the macroscopic magnetic properties of the LCO films. The sample is located in the center of a superconducting solenoid producing magnetic fields up to 7 Tesla. The sample space is filled with helium at low pressure at temperatures ranging from 2 to 400 Kelvin. The sensitivity of the system is 10^{-8} emu in the so-called reciprocating sample option (RSO) mode. A scheme of the technical setup of the SQUID magnetometer is given in Fig. 3.22. To investigate the magnetic properties of a sample, it is exposed to the homogenous field of a superconducting magnet and

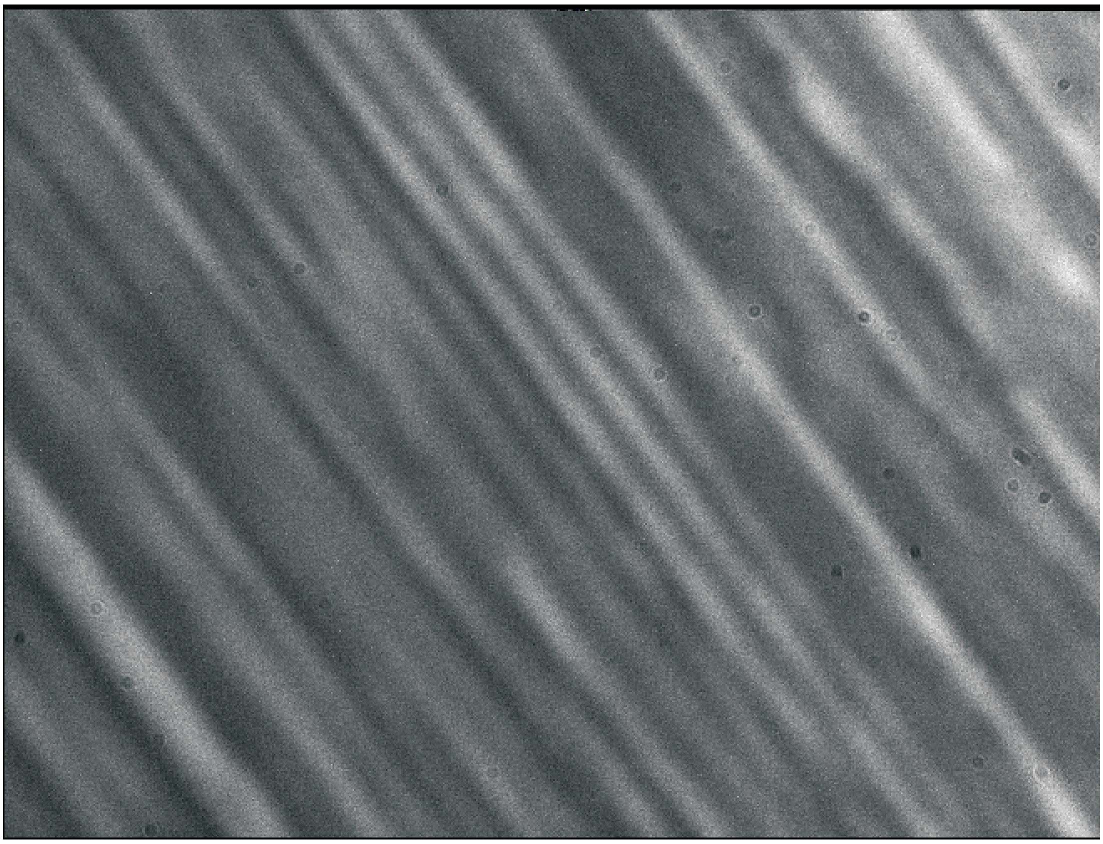

Figure 3.21: A Kerr image of LCO film on LSAT substrate taken at 35 K. The image dimensions are 200 x 150 μm^2

gradually moved through the pick-up coil system, which is essentially an arrangement of induction coils. The magnetic signal of the sample is obtained via a superconducting pick-up coil with 4 windings. This coil is, together with a SQUID antenna, part of a superconducting circuit transferring the magnetic flux from the sample to a rf SQUID device which is located away from the sample in the liquid helium bath. This device acts as a magnetic flux-to-voltage converter. This voltage is then amplified and read out by the magnetometer's electronics. When the sample is moved up and down it produces an alternating magnetic flux in the pick-up coil which leads to an alternating output voltage of the SQUID device. By locking the frequency of the readout to the frequency of the movement (RSO mode), the magnetometer system can achieve the extremely high sensitivity for ultrasmall magnetic signals as described above. Usually a sample is cycled several times through the pick-up coil system at a constant field and at constant temperature. The signals are then summed and averaged.

3.4.2 Torque magnetometry

As a part of this work, magnetometry measurements on LCO thin films were performed at the 1. Physikalisches Institut, Universität Stuttgart. Torque magnetometry is based on the principle that, when a magnetically anisotropic sample is placed in

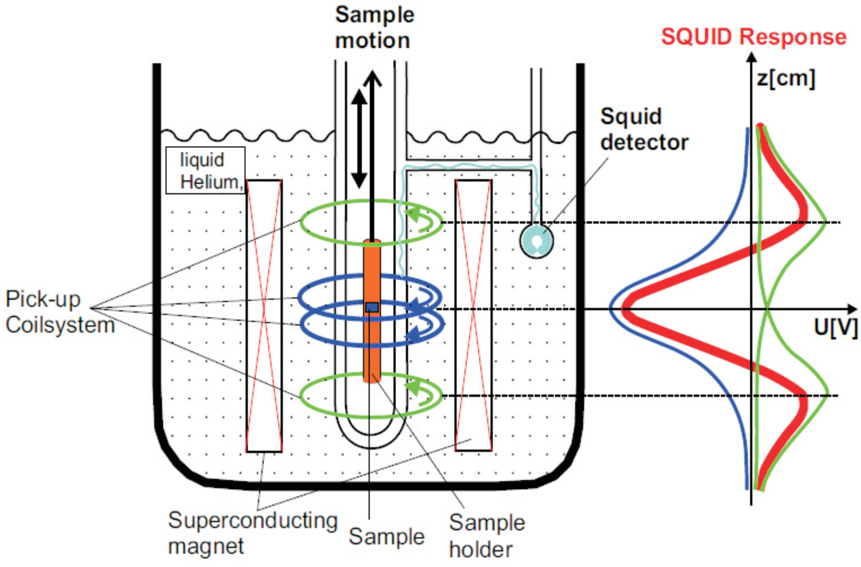

Figure 3.22: Scheme of the SQUID set-up

a magnetic field at a certain angle, the field tries to force the magnetization of the sample to align along its direction, whereas the anisotropy energy of the sample tries to keep the magnetization in the easy-axis direction. The consequence is that the field exerts a torque on the sample. The torque is usually detected by mechanical sensors. The deflection of the mechanical system can be measured by optical, piezoresistive or capacitive methods. This torque is measured as the angle of rotation of the sample at a particular field direction. Then, the value of torque is plotted against the rotation angle of the applied magnetic field which results in a torque curve. The torque per volume $L(\mathrm{J/m^3})$ is proportional to the derivative of the anisotropy energy density E_a with respect to the angle Φ between the magnetization and the easy axis:

$$L(\Phi) = -\frac{\partial E_a}{\partial \Phi} \qquad (3.32)$$

In the torque meter, a rotating strong magnetic field turns the magnetization within the film surface plane. The torque vanishes when the magnetic field is parallel to the easy or hard axis. The slope of the curve is a positive torque curve ($\partial L/\partial\Phi > 0$) at the hard axis, while the slope of the curve is negative ($\partial L/\partial\Phi < 0$) at the easy axis. Torque measurements on LCO thin films were performed by using a cantilever torque magnetometry based on capacitive detection method built at the Universität Stuttgart. It can be operated between 1.3 and 300 K in an external magnetic field up to 8 T. The sensitivity of the cantilever was reported to be 10^{-11} Nm, and the rotation resolution is approximated by 0.1°. Sample alignment is achieved with the aid of an optical microscope, and rotation calibration is performed by means of a mirror-laser technique. There are size and mass restrictions, since LCO thin films are on ”heavy substrates”, and the dimensions are relatively large with respect to the requirements of the cantilever. We cut our LCO films into 1 mm x 1 mm pieces with a diamond knife. The substrate was etched down to 200 μm thickness.

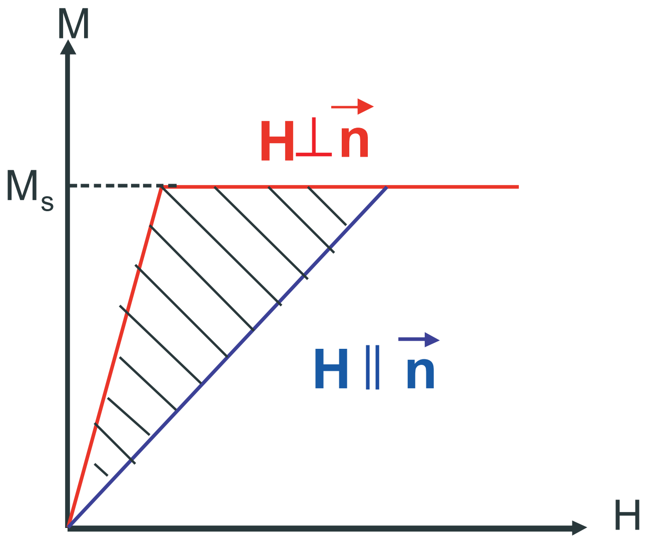

Figure 3.23: Virgin magnetization curves (obtained by cooling the film below T_c in zero field) for a magnetic thin film having an in-plane preferential orientation. Fields are applied parallel (‖) or perpendicular (⊥) to the film plane. These directions are the easy and hard axes, respectively. The saturation field, H_s, is smaller for the easy direction with respect to the that of hard direction. The area between the two curves is a measure of MAE.

3.5 Techniques to determine the anisotropy in thin films

The variation of the film free energy with magnetization orientation means that torques are exerted on the magnetization vector due to the effective field. Thus any experimental technique that permits to measure torques on the magnetization, can be used to obtain the magnetic anisotropy coefficients. A very common method for the investigation of these torques is the Torque magnetometry, which has been explained in the previous section.

A second type of experiments designed to evaluate the anisotropy coefficients is based on the measurement of magnetization curves. Most commonly the magnetic anisotropy energy (MAE) is determined from the field dependent measurements along different crystallographic directions. An example of such a measurement, with the field parallel and perpendicular to the film surface, is demonstrated in Fig. 3.33. The strength of the MAE can be determined from the area, numerically equal to MAE, enclosed between the virgin magnetization curves along the easy and hard axis. This is based on the elementary electromagnetic considerations which shows that in order to saturate the magnetization along the hard axis a certain external field, the saturation field, has to be exceeded. The area corresponds to the effective MAE and is defined as

$$E_{ani} = \int_0^{M_{sat}} (H^{\perp} - H^{\parallel})\, dM \tag{3.33}$$

A very sensitive magnetometer is required to measure the magnetization in thin films. Usually the magnetic moment of a specimen of known thickness and area is measured using a SQUID or vibrating sample magnetometer (VSM). In most cases, as exploiting the "area method", the magnetometer is used only to measure the saturation magnetization, M_s, and the MOKE is used to measure the ratio $M(H)/M_s$ as a function of the applied field, since MOKE cannot provide a direct measurement of the value of the magnetization. MOKE is a particularly convenient tool for finding the orientation of easy and hard magnetic axes. The use of MOKE to investigate anisotropy in thin films can be found in reference [127]. The use of MOKE to measure anisotropy coefficients is discussed by de Jonge *et al.* [128], and by Johnson *et al.* [129]. There are also other approaches to calculate the MAE besides using virgin magnetization curves. de Jonge *et al.* [128] suggested to use complete hysteresis loops taken along the hard and easy axes. Infante *et al.* [130] has calculated the anisotropy energy by determining the area between the easy and hard axes magnetization curves, M, changing from its saturated state to remanence.

Chapter 4

Results and Discussion

In this chapter the study on the correlation between the epitaxial strain and the magnetic properties of $LaCoO_3$ (LCO) thin films is presented. Here, we show that the magnetic properties can be "tuned" by epitaxial strain imposed on LCO thin films by the epitaxial growth on various substrate materials. In the first section, the study on the general magnetic properties, such as magnetization, Curie temperature, coercivity etc., of epitaxial LCO thin films grown on (001)-oriented different substrates is presented. In the next section, the experimental results of the magnetic anisotropy investigations in (001)-, (110)- and (111)-oriented LCO thin films are given. The mathematical expressions used to define and to discuss the magnetic anisotropy in thin films are derived in the Appendix. In the last section, the time dependence of the magnetization in LCO thin films is discussed. A systematic study to reveal the effect of strain on the magnetic relaxation process is presented, and the experimental results are analyzed based on the model regarding a distribution of energy barriers. The experimental results of the three sections are discussed at the end of the each corresponding section.

4.1 Magnetic properties of $LaCoO_3$ thin films

We showed that epitaxial strained LCO thin films show a ferromagnetic phase transition below 85 K despite the non-magnetic ground state of rhombohedral bulk LCO. This observation alone evidences the strong impact of strain on the magnetic properties. In order to study the influence of the epitaxial strain on the magnetic properties of LCO, we have grown epitaxial LCO thin films on (001)-oriented SLAO, SLGO, LSAT, LAO and STO substrates by pulsed laser deposition. In this way, we managed to tune the magnitude of the tensile strain in a controlled way. The details of the deposition and the structural properties of those epitaxial LCO films are given in chapter 3. Magnetic measurements were conducted using SQUID and MOKE magnetometry.

4.1.1 Results

In Fig. 4.1, the magnetization curve is plotted versus temperature for LCO films on LSAT, SLGO, SLAO, LAO and STO substrates in a magnetic field $\mu_0 H$=20 mT applied

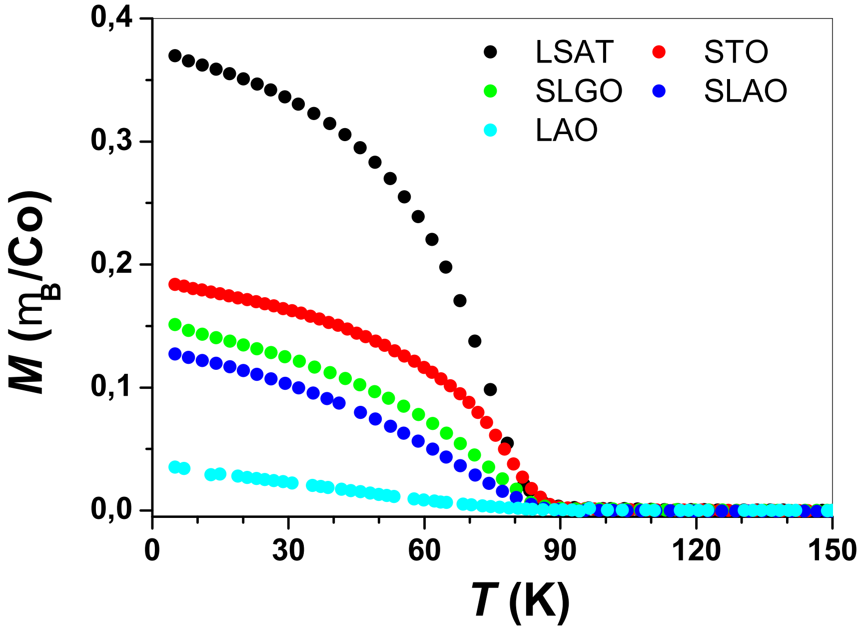

Figure 4.1: Field-cooled (FC) magnetization of LCO films on various substrate materials. The magnetic field $\mu_0 H$=20 mT was applied parallel to the film surface.

parallel to the film surface. In contrast to the non-magnetic ground state of LCO, epitaxially strained films clearly exhibit a ferromagnetic (FM) transition. Both the magnetization and the FM onset temperature of the LCO films in Fig. 4.1 decrease systematically with decreasing in-plane film lattice parameter. In Fig. 4.2a we have plotted the Curie temperature, T_c, as a function of the in-plane film lattice parameter, a. T_c has been determined from the minimum of the derivative of the FC magnetization, dM/dT. We also added the data point for bulk LCO to the plot ($T_c = 0$ and $a = 3.80$ Å). It is obvious that T_c increases very rapidly with increasing lattice constant a and seems to saturate around 85 K above a = 3.86 Å. In order to investigate the influence of the epitaxial strain on the paramagnetic state, we have determined the effective moment μ_{eff} from the susceptibility between 100 and 150 K shown in Fig. 4.2b. In comparison with the effective moment of bulk LCO of μ_{eff}=1.96 μ_B/Co in the temperature range of 100 K< T <300 K [131, 132], epitaxially strained LCO films show higher effective moments ranging from 2.8μ_B/Co for LCO on SLAO up to 4.6 μ_B/Co for LCO on STO.

The increase of the magnetic moment can be attributed to an increased population of higher spin states. In a single-ion picture the effective moment is given by $\mu_{eff} = g_e\sqrt{S(S+1)}$, with the electron g factor $g_e \approx 2$, where μ_{eff} depends on the spin state of the Co ions. The magnetization reversals recorded at T/T_c = 0.7 by MOKE are shown in Fig. 4.3. The loops are more square shaped for the higher tensile strained LCO/LSAT and LCO/STO films. Whilst the magnetization of LCO/LSAT and LCO/STO films reach saturation, it is not achieved for LCO/SLGO and LCO/SLAO films. In ferromagnetic thin films, magnetization reversal takes place

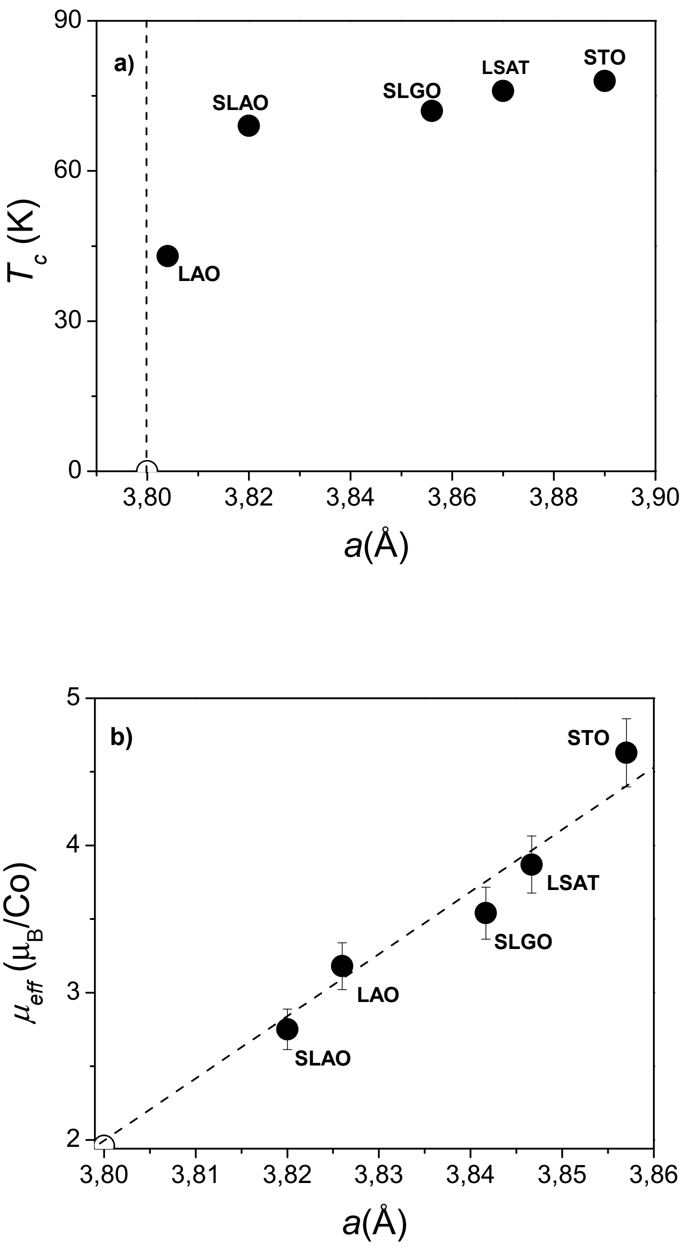

Figure 4.2: a) The Curie temperature, T_c, as a function of the in-plane film lattice parameter, a. The data points are labeled with the names of the corresponding substrates. We also added the data point for bulk LCO (open symbol). b) The effective paramagnetic moment, μ_{eff}, of LCO films as a function of the mean lattice parameter $< a >= (2/3a + 1/3c)$ (closed symbols). The data points are labeled with the names of the corresponding substrates. The bulk value of LCO is displayed by the open symbol. The dashed line is a linear fit to the data points.

by magnetization rotation and/or domain wall motion. Often, both processes take place at the same time with different dynamics, and the shape of the loops is strongly

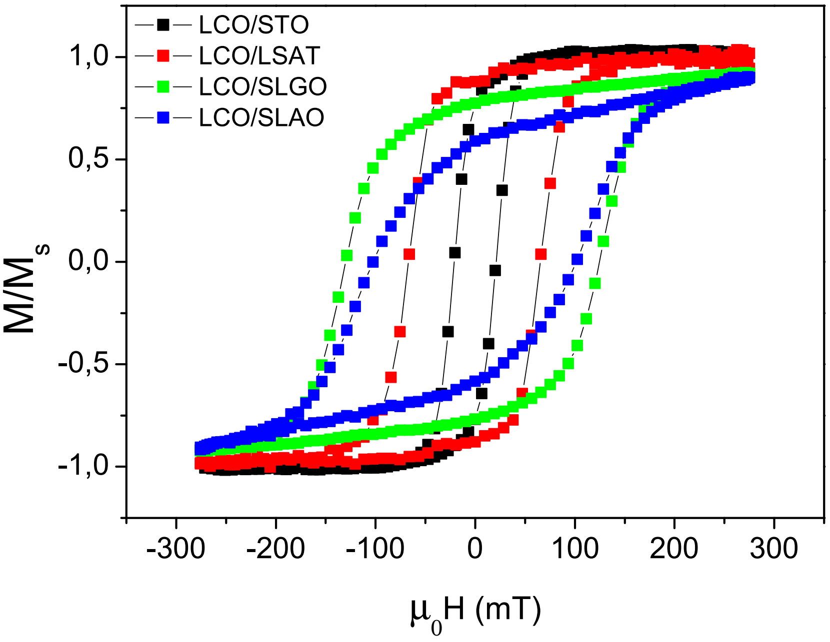

Figure 4.3: Normalized in-plane hysteresis loops of differently strained (001)-oriented LCO thin films recorded by MOKE at T/T_c=0.7.

affected by the type of the reversal process. For instance, a reversal occurring by domain wall motion exhibits more square shaped loop. By comparing the hysteresis loops of LCO/LSAT, LCO/SLGO and LCO/SLAO films one can infer that epitaxial strain has an effect on the reversal dynamics. In Fig. 4.4a the temperature dependence of the coercive field, H_c, measured by the SQUID magnetometer, is shown. H_c increases with decreasing temperature, which is a general property of ferromagnetic materials because magnetization rotation and domain wall motion are thermally activated. Likewise, the difference in H_c for the different films becomes more pronounced as the temperature decreases. The coercive fields of LCO/STO ($\epsilon_{xx} \approx 1.4\%$) and LCO/LSAT ($\epsilon_{xx} \approx 1.1\%$) films are remarkably smaller than that of LCO/SLAO ($\epsilon_{xx} \approx 0.1\%$) and LCO/SLGO ($\epsilon_{xx} \approx 0,5\%$) films at 10 K. The dependence of the remanent magnetization normalized to saturation magnetization, M_r/M_S, on the epitaxial strain is shown in Fig. 4.4b. The saturation magnetization of LCO/SLAO and LCO/SLGO films was estimated by the extrapolation of the $M(H)$ curves since it was not possible to saturate completely those films even at $\mu_0 H$ =7 T. It is obvious that M_r/M_s increases with increasing tensile strain and seems to saturate above $\epsilon_{xx} = 1.1\%$. This behavior resembles that of T_c as a function of a (Fig. 4.2) although the approach to saturation is slower.

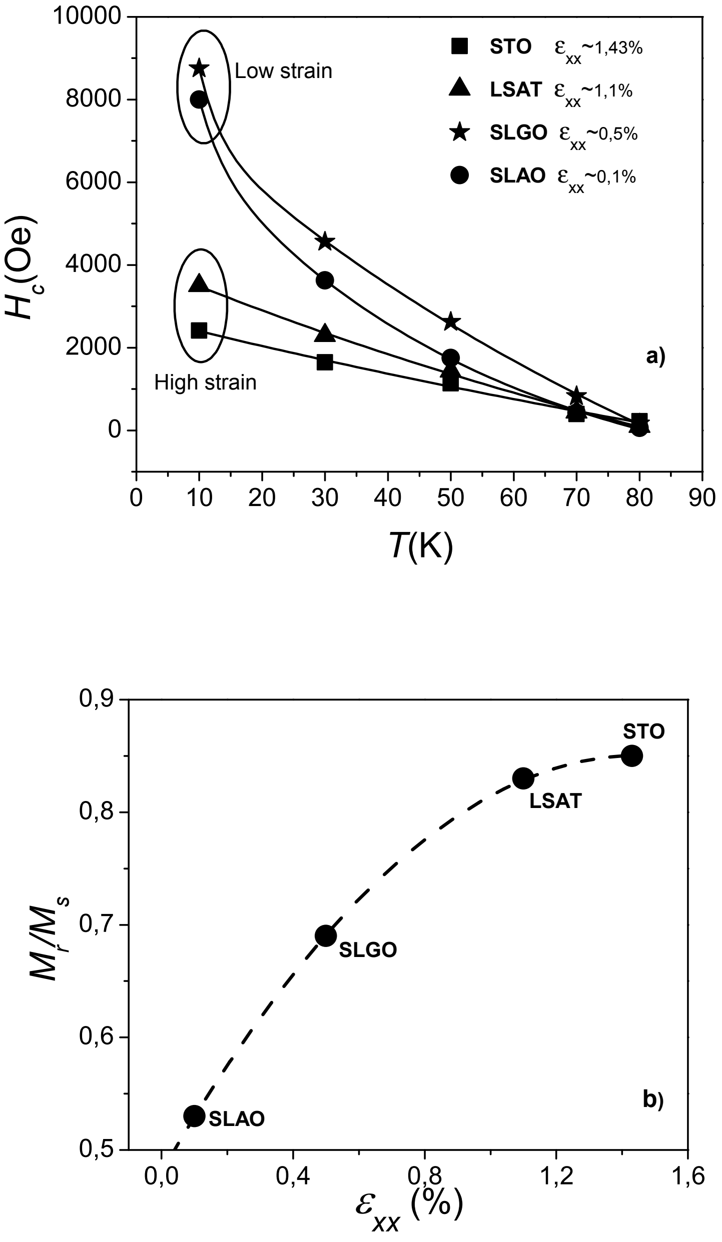

Figure 4.4: a) The coercive field, H_c, as a function of the temperature for the differently strained films. The increase of H_c with decreasing temperature is common for all the films. The value of H_c differs for the different films. The coercive field is larger for the "less" tensile strained LCO/SLAO and LCO/SLGO films, while H_c is smaller for the "high" tensile strained LCO/LSAT and LCO/STO films. b) M_r/M_s as a function of tensile strain. The dashed line is a guide to the eyes.

4.1.2 Discussion and conclusion

A possible explanation for the trend of T_c displayed in Fig. 4.2) could be an increase of the Co-O-Co bonding angle β toward 180° with increasing lattice constant caused by increasing tensile strain. LDA calculations of Eyert *et al.* [64] demonstrated that the tendency to long-range order is significantly influenced by the symmetry. He obtained an increase of the partial densities of states (PDOS) of t_{2g} states near the Fermi energy E_F for a simple cubic structure of $\mathrm{LaCoO_3}$ in comparison to a rhombohedral structure. The approach to cubic symmetry ($\beta \to 180°$) leads to a lower hybridization of t_{2g} states and thus an increased PDOS. Therefore, the increase of T_C is likely caused by an increased PDOS of t_{2g} state near E_f [133]. Moreover, SXMCD measurements demonstrated that ferromagnetism is most probably established via superexchange where the spin and orbital moment of t_{2g} electrons is transferred between Co and O.

The increase of μ_{eff} with tensile strain in Fig. 4.2b indicates an increased population of IS and HS states. The increased population of IS and HS states is primarily due to a reduction of the energy difference ΔE between the crystal-field splitting and the intra-atomic exchange interaction, which leads to a redistribution of electrons between the t_{2g} and e_g levels. A strong hybridization between Co e_g orbitals and p orbitals of the oxygen ligands favors the IS state, as has been shown by calculations based on density-functional theory [8, 131]. The hybridization broadens the bandwidth W of the $d-p$ bands, which reduces the energy difference to $([\Delta_{CF} - W/2] - \Delta_{EX})$, and makes the e_g and t_{2g} bands overlap [58]. Since the bandwidth is given by $W \propto \cos(\pi - \beta)/d^{3.5}$, higher spin states are not only stabilized by a decrease of Δ_{CF} but also by an increase of W, i.e., an increase of the Co-O-Co bond angle β and a decrease of the Co-O bond length d. Since tensile strain affects both β and d, and hence Δ_{EX} and W, a clear assignment of what causes the increase of μ_{eff} cannot be made. Let us consider the reversal process, which will be a complex combination of irreversible rotation of domain magnetization and domain wall motion. From the energy considerations, in a ferromagnetic volume (assuming there are no strong pinning centers) a smaller field is required to achieve magnetization reversal by domain wall motion than by irreversible magnetization rotation [134]. Thus, when the reversal is dominated by domain wall motion, a smaller coercivity is expected with respect to rotation dominated reversal. Often, the two phenomena can be distinguished from the shape of reversal loops. The loops observed for a domain wall displacement have a rectangle-like appearance compared to the rounded loops for magnetization rotation [135–137]. By comparing the coercivities and the loop shapes of differently strained LCO films, we can claim that tensile strain enhances primarily the domain wall dynamics. However, magnetization reversal is a rather complex phenomenon with several parameters playing a crucial role, such as pinning centers, dislocations, local magnetic anisotropies, grain sizes etc. Strain might couple with all the parameters to some extent. Therefore, it is hard to draw a concrete conclusion of how strain can enhance the domain wall motion in detail.

In conclusion, the transition temperature T_c and the magnetization increase strongly with increasing a, where T_c seems to saturate at T_c=85 K above a=3.86 Å. The effective magnetic moment μ_{eff} in the paramagnetic state increases linearly with $< a >$, which may indicate an enhanced population of IS or HS spin states. Magnetization reversal dynamics appears to be affected by strain. The coercive field decreases while remanent magnetization increases with increasing tensile strain as well. The tensile strain seems to favor the domain wall motion dominated reversal.

4.2 Magnetic anisotropy in $LaCoO_3$ thin films

In the previous section we evidenced the strong impact of strain on the magnetic properties. Even a small strain of the order of 0.1% can induce a significant change in the magnetic anisotropy in thin films depending on the magnitude and the sign of the magnetoelastic coefficient B_i. In the case where magnetoelastic anisotropy is larger than other contributions, strain may be established as a tailoring tool of magnetic anisotropy for potential applications.

In this section the magnetic anisotropy of $LaCoO_3$ thin films is discussed based on simple energy expressions considering magnetic thin films with cubic symmetry, and compared with other perovskite systems. The energy expressions are derived for different crystallographic orientations in the Appendix. The individual magnetic anisotropy contributions (shape, magnetocrystalline, and magnetoelastic anisotropies) are determined and compared. In particular, the important role of the epitaxial strain on the magnetic anisotropy is discussed. Experimentally, the determination of the magnitude of the strain induced anisotropy is difficult due to the contribution from other terms which must be separated from total anisotropy. The experimental procedure for the quantitative determination of strain induced anisotropy is described. The magnetocrystalline and magnetoelastic anisotropy constants are extracted and compared with that of LSMO thin films. Moreover, the extracted values are used to simulate the effective magnetic anisotropy, which is compared with experimental results in order to check the reliability of the analysis.

The investigated $LaCoO_3$ thin films were prepared as it is explained in section 3.1. The magnitude of the epitaxial strain in the films was controlled by growing the films on the single crystal substrates with different lattice parameters. The strain field was varied by growing (001)-, (110)- and (111)-oriented LCO thin films on LSAT substrates. In the following, we have exploited magneto optical Kerr effect (MOKE), superconducting quantum interference device (SQUID), and torque magnetometry to study the magnetic anisotropy.

4.2.1 Results

(001) oriented LCO thin films

As a starting point we recorded in-plane (the external magnetic field is applied along the surface plane of the film) and out-of-plane (the external magnetic field is applied along the surface normal) hysteresis loops of (001)-oriented LCO thin films with different magnitudes of tensile strain by MOKE. In general, we observed hysteresis loops for the tensile strained (001)-oriented films for field in the film plane only, showing that the magnetization is preferred to lie in the film plane (easy plane), whereas the c axis is the hard axis. In Fig. 4.5, we illustrate out-of-plane and in-plane magnetization data of strained (001)-oriented, approximately 30 nm thick LCO/LSAT, LCO/SLGO and LCO/SLAO thin films. Zero remanent magnetization of out-of-plane loops indicates

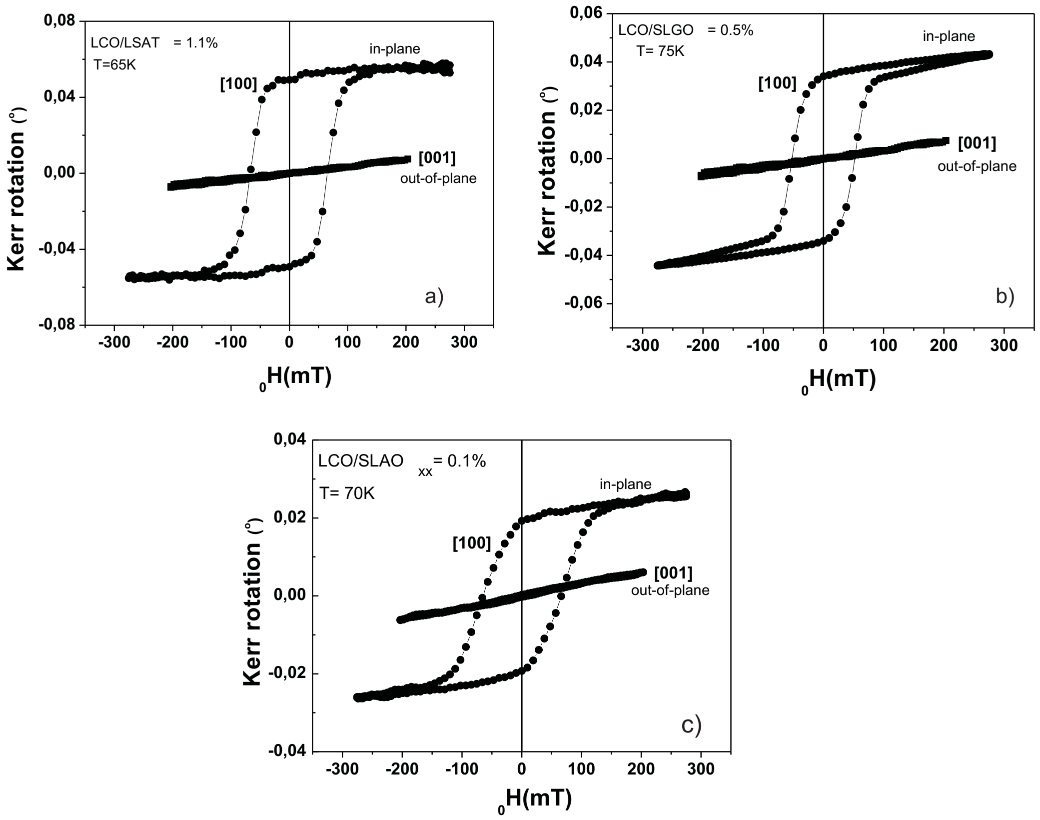

Figure 4.5: MOKE measurements on (001) oriented LCO thin films for different magnitudes of strain. Kerr rotation is proportional to the magnetization. a) In-plane and out-of-plane hysteresis loops of the LCO/LSAT thin film with tensile strain $\epsilon \approx 1.1\%$ taken at 65 K. b) Loops for the LCO/SLGO thin film which accommodates $\epsilon \approx 0.5\%$ taken at 75K. c) Loops of the less strained LCO/SLAO thin films $\epsilon \approx 0.1\%$. All the films show clear in-plane magnetization, and the hard axis is along the c. axis.

a magnetic hard axis along the c axis. Moreover, the small values of Kerr rotations obtained for the [001] direction even at the highest applied field suggests that magnetization is strongly pinned in the film plane. This behavior is observed at temperatures below the Curie temperature.

The magnetic energy difference between the out-of-plane and in-plane magnetizations, the so-called out-of-plane anisotropy, $E_a^{op} = E([001]) - E([100])$, includes the shape and magnetoelastic anisotropy for (001)-oriented LCO thin films. (Contributions to magnetocrystalline anisotropy vanish if cubic symmetry is considered in thin films, see Appendix). As it is seen in Fig. 4.5, while the magnetization approaches saturation above 150 mT applied field in the plane direction, it is far away from the saturation for the out-of-plane measurements. The saturation field is well above 300 mT, which is the limit of the experimental apparatus. Even with SQUID measurements it was not possible to saturate the out-of-plane magnetization at a field strength of up to 7 T. Although an in-plane magnetization is typical for ferromagnetic thin films due to the demagnetizing field, the large difference between magnetization along the

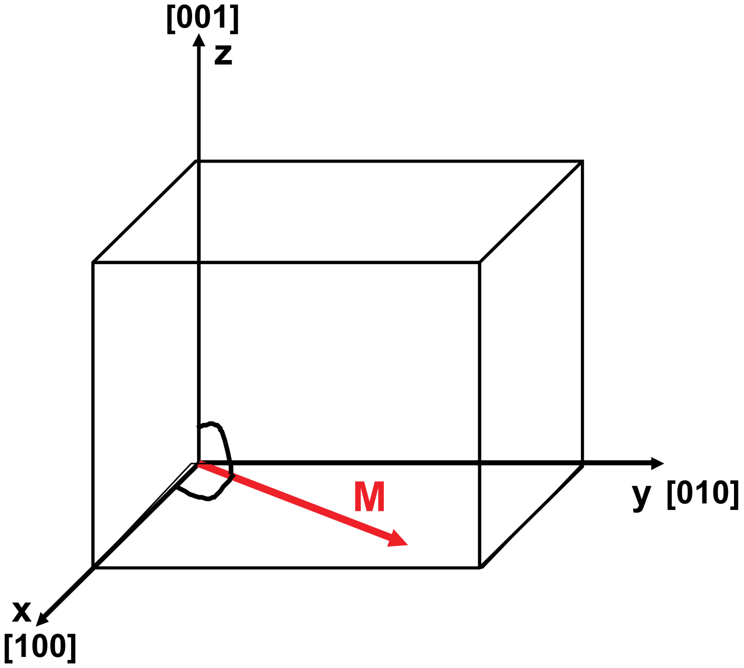

Figure 4.6: Crystallographic coordinates of (001) oriented thin films with z axis along the [001] direction. The angular dependence of the magnetization in the plane of the film is monitored by the angle Φ, the angle between the [100] axis and the magnetization. The polar dependence of the magnetization monitored by the angle Θ, the angle between [001] axis and the magnetization.

[100] and [001] directions suggests additional anisotropy contributions which favor an in-plane magnetization. In order to account for strong pinning of the magnetization in the film plane, the nature of the magnetoelastic anisotropy in epitaxial LCO thin films was explored in detail.

In the following, we discuss, first, the angular dependence of in-plane magnetization of (001)-oriented epitaxial strained LCO thin films. The high crystal quality of our thin films allows us to investigate the angular dependence of the in-plane magnetization with respect to the crystallographic coordinates of the film shown in Fig. 4.6. Given the fact that the magnetization vector will tend to align itself along the external applied field, the angular dependence of the magnetization can be determined by performing magnetic measurements for various angles Φ of the external magnetic field with respect to the film axis. The first magnetic analysis was carried out with the MOKE-technique using the longitudinal Kerr effect. MOKE hysteresis loops of a LCO/LSAT thin film taken along the [100] and [110] directions are shown in Fig. 4.7a. The normalized remanent value, M_r/M_s, differs for the two directions. M_r/M_s is equal to 0.87 for the [110] direction and 0.73 for the [100] direction. This observation yields that [110] is the easy axis while [100] is the harder one. Moreover, it is clearly seen that for the measurement along the [100] direction, the magnetization approaches saturation only at higher fields, which is a clear indication for [100] hard axis. A comparison of the magnetization versus temperature data for the [110] and the [100] directions, shown in

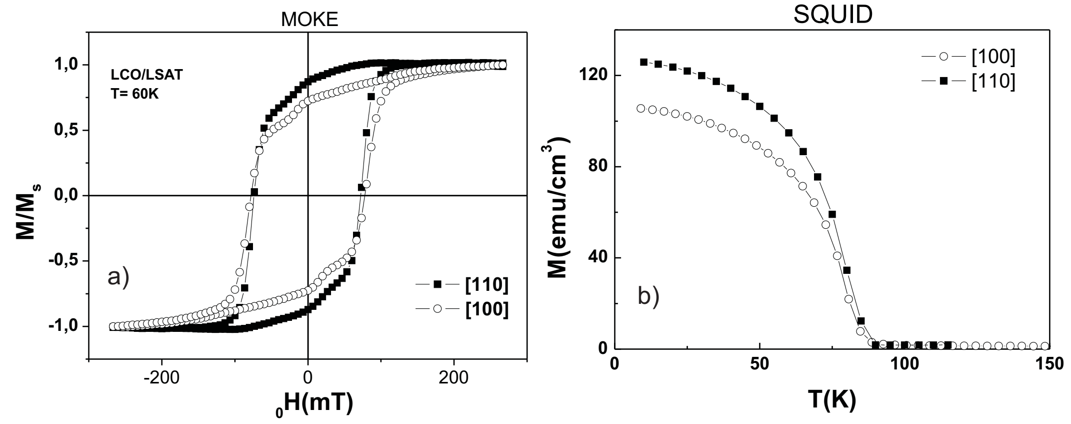

Figure 4.7: a) Hysteresis curves along the in-plane [110] easy and [100] hard axis at T=60 K for an epitaxial LCO film, t=30 nm grown on (001) LSAT substrate. b) Magnetization versus temperature taken with the field $\mu_0 H$=30 mT applied along the [110] and [100] directions.

Fig. 4.7b, immediately shows that the magnetization is somewhat enhanced along the [110] direction in comparison to that of [100] direction. In addition, similar measurements were taken along the [010], [$\bar{1}$00], [1$\bar{1}$0] and [$\bar{1}$10] directions, and the observed behavior corresponds to the characteristics of biaxial anisotropy with [110] easy and [100] hard axes.

We carried out torque magnetometry measurements on the same thin films. Torque measurements, torque was measured as a function of the angle Φ between the applied 5-T field and the [100] direction at 1.7 K, as displayed in Fig. 4.8. Torque measurements of (001) LCO/LSAT films show a clear biaxial anisotropy confirming the MOKE measurements. The interpretation of the torque data depends on the free-energy expressions used to describe the magnetic anisotropy given in the Appendix. Since the magnetization is confined to the (001) plane ($\Theta = \pi/2$) during the measurements, only the angle Φ is needed to specify the in-plane anisotropy, which can be described using the following energy expressions. The angular dependence of the energy density for (001) oriented LCO films assuming cubic symmetry is then given by:

$$E^{(001)}_{tot.}(\Theta = \pi/2, \Phi) = \frac{K_1}{4}\sin^2(2\Phi) \tag{4.1}$$

where K_1 is the first-order cubic magnetocrystalline anisotropy constant. According to the expression above, the magnetocrystalline energy exhibits biaxial anisotropy in the (001) plane. And, thus, for (001) LCO thin films, in-plane magnetic anisotropy is caused by the magneto-crystalline anisotropy, with the magnitude of $E^{ip}_a = E[100] - E[110] = -K_1/4$, which is defined as the energy difference between the hard and easy axes. With the energy density given by Eq. 4.1, the calculated torque is given as [138]

$$L(\Phi) = -\frac{\partial E^{(001)}_{tot.}(\Theta = \pi/2, \Phi)}{\partial \Phi} = -\frac{1}{2}K_1\sin(4\Phi) \tag{4.2}$$

Indeed, the torque curve in Fig. 4.8a shows a sin(4Φ) dependence. Furthermore, the very good agreement between the torque data and fitted curve (solid line) using Eq. 4.2

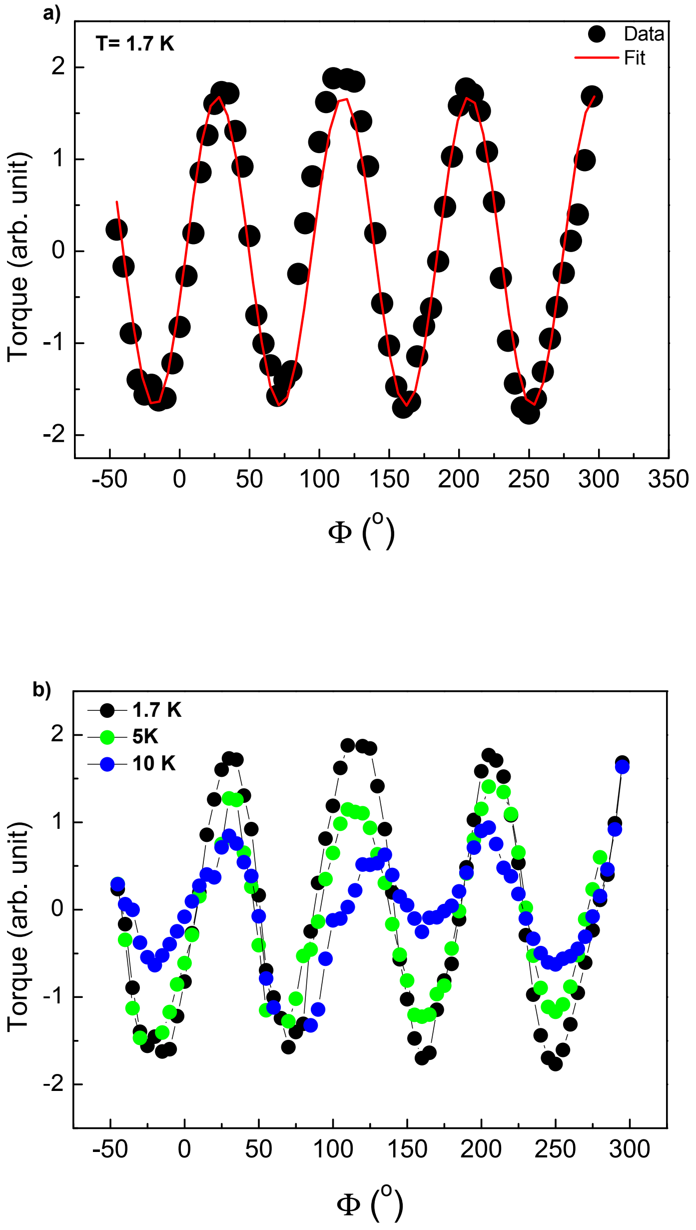

Figure 4.8: a) The torque as a function of Φ for a (001) LCO/LSAT thin film. At $\Phi = 0°$ the magnetic field is parallel to the [100] direction of the film. The torque shows four-fold symmetry indicating the existence of the biaxial magnetic anisotropy in the (001) plane of the film. The experimental data were fitted with Eq. 4.2 (red curve). The quality of the fit proves that the in-plane magnetic anisotropy of the (001) LCO/LSAT film can be described by cubic magnetocrystalline anisotropy with the fit parameter $K_1 < 0$. The negative sign of the magnetocrystalline anisotropy constant leads the easy axis along the [110] direction and the hard axis along the [100] direction, which is consistent with MOKE measurements. b) Torque curves taken at different temperatures. The biaxial anisotropy becomes more pronounced as the temperature decreases. Data taken at the University of Stuttgart.

suggests that the biaxial anisotropy of the magnetization in the (001) plane of LCO thin film with easy and hard axes along the [110] and [100] directions, respectively, can be described by taking only the cubic crystal anisotropy constant $K_1 < 0$ into account. The temperature dependence of the observed biaxial anisotropy is also shown in Fig. 4.8b. Biaxial anisotropy becomes more distinguishable at lower temperatures. This is consistent with the well-known fact that magnetocrystalline anisotropy increases with decreasing temperature in most of the ferromagnetic systems. The magnitude of the in-plane anisotropy, $E_a^{ip} = -K_1/4$, is determined from the difference of the works, $W = \int_{M_r}^{M_s} HdM$, done by the applied field along the [100] and [110] directions in Fig. 4.7 as described by Infante *et al.* [130] (see section 3.5). The extracted value of the cubic magnetocrystalline anisotropy constant amounts to $K_1 \approx$ -1.2x10^4 erg/cm^3 at 60 K.

In the following, we present the results on the out-of-plane magnetic anisotropy. The hysteresis loops along [100] and [001] directions in Fig. 4.5 indicate a large out-of-plane anisotropy with a strong hard axis parallel to the surface normal and easy axes along the film plane. The polar dependence (Θ dependence) of the energy density is written as:

$$E_{tot}^{(001)}(\Phi = 0, \Theta) = K_1/4 \sin^2 2\Theta + 1/2\mu_0 M_s^2 \cos\Theta + B_1(\epsilon_1 - \epsilon_3)\sin^2\Theta \tag{4.3}$$

where the first term is the cubic magnetocrystalline energy, the second is the shape energy and the last term is the magnetoelastic energy. According to Eq. 4.3 the magnetocrystalline energy induces a biaxial anisotropy, while shape and magnetoelastic anisotropies induce a uniaxial anisotropy. Since the magnetocrystalline energy is the same for $< 100 >$ cubic crystal axes, the magnetocrystalline anisotropy does not contribute to E_a^{op}. The magnetic anisotropy is then determined by the magnetoelastic anisotropy and the demagnetizing field, which gives ($\epsilon_1 = \epsilon_2 = -\epsilon_3 = \epsilon_0$)

$$E_a^{op} = E([001]) - E([100]) = -2B_1\epsilon_0 + 1/2\mu_0 M_s^2 \tag{4.4}$$

It is clear that regarding tensile strain ($\epsilon_0 > 0$), magnetoelastic anisotropy favors in-plane magnetization if the magnetoelastic coefficient B_1 is negative, while out-of-plane magnetization is preferred for positive B_1 and $|B_1| > \frac{1}{4}\frac{\mu_0}{\epsilon_0}M_s^2$. The shape anisotropy can be calculated easily by extracting the M_s value from SQUID measurements. Then, the area between $M(H)$ curves along the [100] and [001] directions is a direct measure of the magnetoelastic anisotropy providing the magnetization saturation in both direction is achieved. Since our strained (001) LCO films cannot be saturated along the c axis, we cannot apply the area method as mentioned above.

Instead, we use a different approach by exploiting the virgin $M(H)$ curves along the [100] directions of (001) LCO films with different strain in order to discuss strain induced magnetic anisotropy quantitatively. In Fig. 4.9a we show virgin $M(H)$ curves of the LCO/LSAT($\epsilon_0 \approx$ 1.1%) and LCO/SLGO($\epsilon_0 \approx$ 0.5%) as well as LCO/SLAO ($\epsilon_0 \approx$ 0.1%) thin films taken at 20 K. The quantitative discussion of the magnetoelastic anisotropy in LCO thin films is on the electromagnetic considerations (See 3.5). According to the area method, the work difference, $\Delta W = \int_0^{M_s}(H_1 - H_2)\,dM$ of two differently strained films, ϵ_0^1 and ϵ_0^2 ($\epsilon_1 = \epsilon_2 = -\epsilon_3 = \epsilon_0^i$), is equal to the total anisotropy, $\Delta W = E_a$. If the magnetocrystalline and the shape anisotropy are the same for two

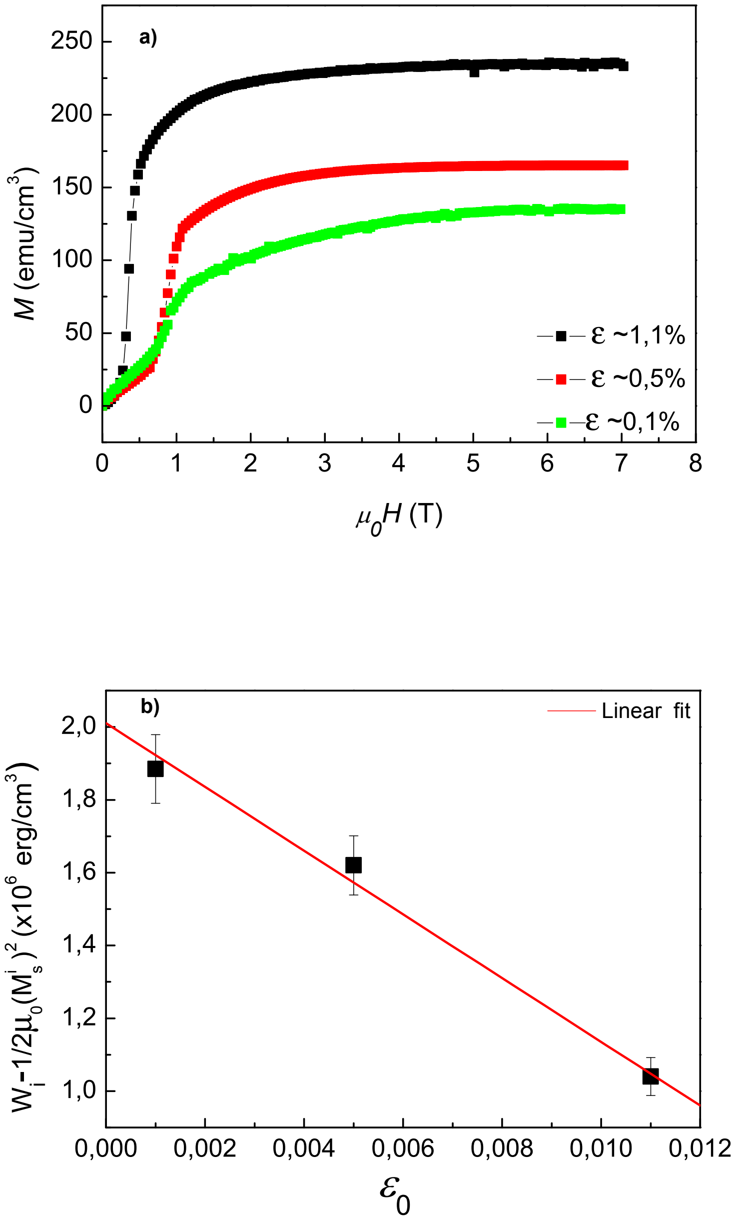

Figure 4.9: a) The virgin $M(H)$ curves recorded in applied field along the [100] direction for LCO/LSAT ($\epsilon_0 \approx 1.1\%$), LCO/SLGO ($\epsilon_0 \approx 0.5\%$) and LCO/SLAO ($\epsilon_0 \approx 0.1\%$) thin films. b) $W_i - 1/2\mu_0(M_s^i)^2$ versus epitaxial strain. The work, $W_i = \int_0^{M_s^i} H\,dM$, was calculated from the curves shown on the left. The work difference $\Delta W = \int_0^{M_s^1} H_1\,dM - \int_0^{M_s^2} H_2\,dM$, is equal to sum of the magnetoelastic and the shape anisotropy, $\Delta W = B_1(\epsilon_0^1 - \epsilon_0^2) + 1/2\mu_0(M_s^1 - M_s^2)^2$. Thus, the slope of the linear fit gives B_1=-8.7x10^7 erg/cm^3.

films, ΔW is equal to magnetoelastic anisotropy. However, as seen in Fig. 4.9a, the saturation magnetization, M_s, differs for the different strained LCO films. Then, the

Table 4.1: Intrinsic magnetic anisotropy constants, K_1 and B_1, for 30 nm LCO/LSAT thin film ($\epsilon_0 = 0.011$) . The values for the shape (E_d), magnetocrystalline (E_{mc}) and magnetoelastic (E_{me}) anisotropies are also shown. The uniaxial out-of-plane anisotropy is the sum of the uniaxial shape and the magnetoelastic anisotropy, E_a^{op} ≈2.0x10^6 erg/cm^3, which exhibit hard axis along the [001] direction. The biaxial anisotropy is determined by the weak magnetocrystalline anisotropy, E_a^{ip} ≈0.3x10^4 erg/cm^3.

Anisotropy constant	E$_a$ (erg/cm^3)
M_s=2.35x10^2 emu/cm^3	$E_d = \frac{\mu_0}{2}M_s^2 \approx 3.3\text{x}10^5$
K_1=-1.2x10^4 erg/cm^3	$E_{mc} = -\frac{K_1}{4} \approx 0.3\text{x}10^4$
B_1=-8.7x10^7 erg/cm^3	$E_{me} = -2B_1\epsilon_0 \approx 1.7\text{x}10^6$

work difference $\Delta W = \int_0^{M_s^1} H_1\,dM - \int_0^{M_s^2} H_2\,dM$, is equal to sum of the magnetoelastic and the shape anisotropy, $\Delta W = B_1(\epsilon_1 - \epsilon_2) + 1/2\mu_0(M_s^1 - M_s^2)^2$. By calculating ΔW from Fig. 4.9a and using the M_s^i values from the same $M(H)$ curves, we can calculate B_1. In Fig. 4.9b we plot $W_i - 1/2\mu_0(M_s^i)^2$ as a function of the strain, where the slope is equal to B_1=-8.7x10^7±1.0x10^7 erg/cm^3. The negative sign of B_1 imposes the magnetoelastic anisotropy favoring in-plane magnetization in the case of the tensile strained (001) oriented LCO thin films.

In table 4.1, we list the obtained magnetic anisotropy constants and the resulting individual magnetic anisotropy for (001) oriented 30-nm thick LCO/LSAT thin film. A very interesting result is that both shape and magnetoelastic anisotropies cause a very strong uniaxial out-of-plane anisotropy $E_a^{op} = E([001]) - E([100]) = -2B_1\epsilon_0 + 1/2\mu_0 M_s^2 \approx$ 2.0x10^6 erg/cm^3 with the hard axis along the surface normal. This large anisotropy accounts very likely for the very high saturation field required along the [001] direction. The biaxial in-plane anisotropy is rather weak due to the small crystalline anisotropy constant, $E_a^{ip} = E([100]) - E([110]) = -\frac{K_1}{4} \approx$ 0.3x10^4 erg/cm^3. The comparison of the individual anisotropies tabulated in the table 4.1 immediately reveals the dominant role of the magnetoelastic anisotropy over the other terms. Of particular interest, the results suggest that magnetic anisotropy can be switched from in-plane to out-of-plane if a strong enough compressive strain is introduced to (001) LCO thin films. So, the strain might be used as controlling parameter to tune magnetic anisotropy in epitaxial LCO thin films.

In Fig. 4.10 we simulate $E_{tot}^{(001)}$ using the experimental values as tabulated above. The in-plane angular dependence of $E_{tot}^{(001)}$, is shown in Fig. 4.10b, where the weak biaxial anisotropy with easy axes along [110] and hard axes along [100] can be seen. The strong uniaxial anisotropy along the surface normal due to the adding of the shape and magnetoelastic anisotropy is shown in Fig. 4.10c.

(110) oriented thin films

From symmetry considerations, in (001) oriented films an in-plane anisotropy with a fourfold symmetry should be observed, while for a (110) orientation a twofold symmetry is expected. The angular dependence of the magnetization in the plane of (110) oriented

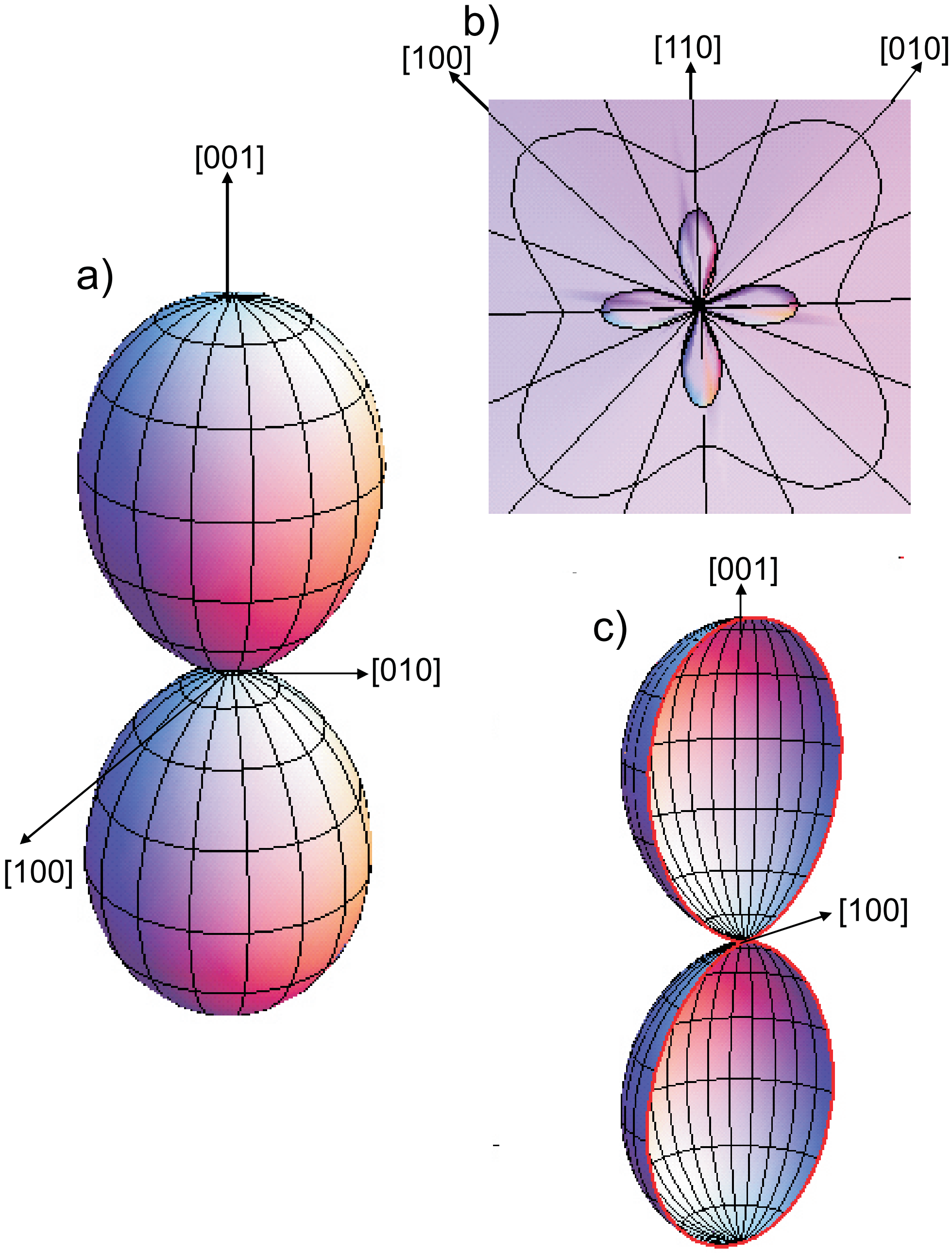

Figure 4.10: a) Calculated anisotropy energy, E_{ani} for the 30 nm (001) oriented tensile strained LCO/LSAT thin film using the experimental values from Tab. 4.1. b) A cut along the *ab* plane through the energy surface showing the presence of a fourfold anisotropy. c) A cut through the energy surface along the *ac* plane showing the presence of strong uniaxial anisotropy along the out-of-plane direction.

films (see Appendix) depends on the competition between the magnetocrystalline and the magnetoelastic anisotropy. Thus, the in-plane anisotropy of LCO thin films may be manipulated by growing the films on (110) oriented substrates.

In order to study the magnetic anisotropy in the (110) surface, LCO films were

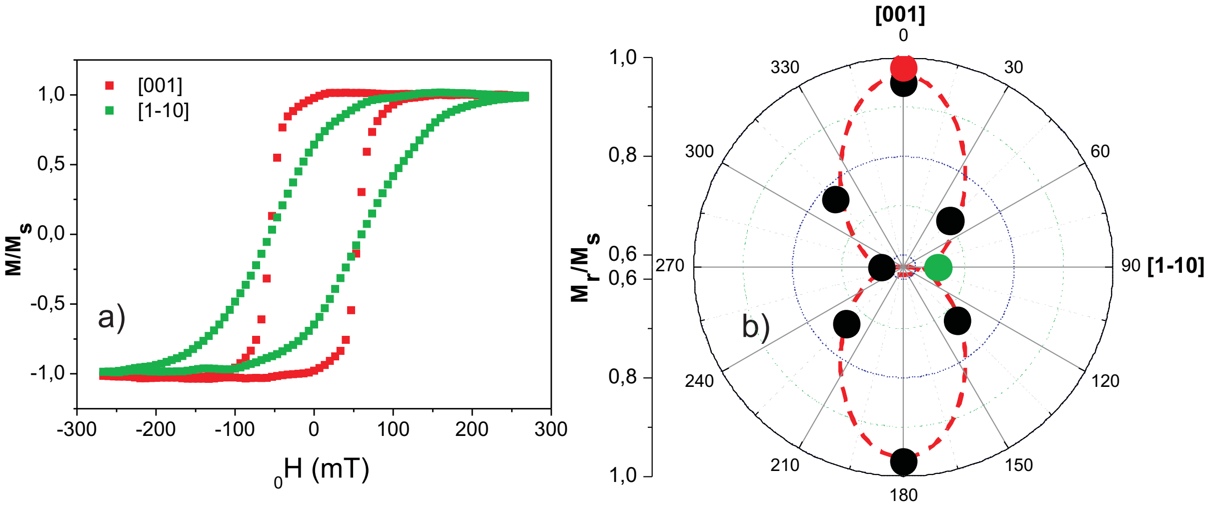

Figure 4.11: a) The normalized hysteresis loops taken along the [001] and [1$\bar{1}$0] directions of a (110) oriented film. The red dashed line is guide to the eye. b) Polar plot (Φ-dependence, $\Theta = \pi/2$) of M_r/M_s extracted from hysteresis loops. The individual loops were recorded after each 45° rotation of the film with respect to the external field direction. The angular dependence of M_r/M_s indicates a uniaxial magnetic anisotropy with easy and hard axes along the [001] and [1$\bar{1}$0] directions, respectively.

grown on (110) LSAT by the PLD technique under the same conditions applied to (001) oriented films. The X-ray diffraction measurements confirmed the cube-on-cube epitaxial growth. In the pseudocubic notation, the LCO films have therefore the [110] direction perpendicular to the film plane, while the [1$\bar{1}$0] and [001] directions lie in the film plane. The quality of the crystal structure was confirmed by the full width at half maximum (FHWM) of the rocking curve which was less than 0.25°.

We first recorded in-plane hysteresis loops of (110) LCO/LSAT thin films at 60 K by MOKE, from which the normalized remanent magnetization, M_r/M_s, of each individual loop was extracted. The direction of the external magnetic field was varied within the film plane. The angular dependence of M_r/M_s is plotted in Fig. 4.11 with the step-width of 45°. We observed that M_r/M_s is lowest for the [1$\bar{1}$0] loops and highest for the [001] loops while it takes intermediate values for loops in-between. This result points to an uniaxial anisotropy with easy axis along [001] and hard axis along the [1$\bar{1}$0] direction. However, the angular resolution and the accuracy of the MOKE measurement are not large enough to discuss a possible uniaxial anisotropy. We also performed torque magnetometry measurements on (110) films under the same conditions as applied to (001) films. In Fig. 4.12 the in-plane torque data obtained as a function of angle, Φ, between the applied field and the [001] direction are shown. The torque curve showing two-fold symmetry indicates a uniaxial anisotropy in the plane of the (110) oriented films with the easy and hard axes along the [001] and [1$\bar{1}$0] directions, respectively. Taking the energy expressions derived for the (110) oriented films in the Appendix by using the proper tensor transformation, the angular dependence of the

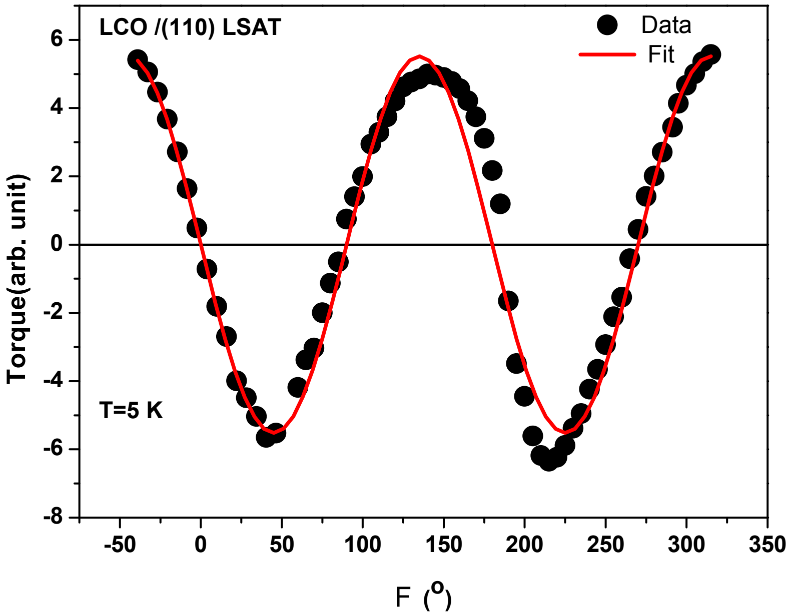

Figure 4.12: Torque curve of a (110) LCO/LSAT film at 5 K. The field is applied in the plane of the film as a function of Φ between the applied field and the [001] direction. The red curve is the fit by using Eq. 4.6.

energy density in the film plane of (110) oriented LCO films is given as:

$$E_{tot}^{(110)}(\Theta = \pi/2, \Phi,) = \frac{1}{4}K_1(\sin^4\Phi + \sin^2 2\Phi) + (B_1\epsilon_0\cos^2\Phi + B_2\epsilon_0\sin^2\Phi) \tag{4.5}$$

where the first term is the magnetocrystalline energy and the second term is the magnetoelastic energy. The combination of the magnetocrystalline and magnetoelastic anisotropies determines the in-plane anisotropy of (110) films. In order to clarify the origin of the uniaxial magnetic anisotropy in the (110) plane, we first discuss the magnetocrystalline anisotropy. Regarding a negative K_1, as inferred in the previous section, the expected magnetocrystalline anisotropy in the (110) plane is shown in Fig. 4.13 (first term in the Eq. 4.5). Obviously, it yields a hard axis along the [001] direction.

However, we observed a uniaxial anisotropy with a [001] easy axis that cannot be explained by the cubic magnetocrystalline anisotropy. One possibility to explain this result is to invoke a dominant uniaxial magnetoelastic anisotropy with an easy axis along the [001] direction caused by the second term in the Eq. 4.5. Indeed, it predicts a uniaxial anisotropy in the (110) plane unless $B_1 = B_2$. The direction and the strength of the uniaxial anisotropy depends on the relative values of the first- and second-order magnetoelastic coefficients. By assuming the magnetocrystalline anisotropy to be much weaker compared to the magnetoelastic anisotropy, we can neglect E_{mc} and the torque is given by:

$$L(\Phi) = -\frac{\partial E_{tot.}^{(110)}(\Theta = \pi/2, \Phi,)}{\partial \Phi} \approx \epsilon_0(B_1 - B_2)\sin 2\Phi \tag{4.6}$$

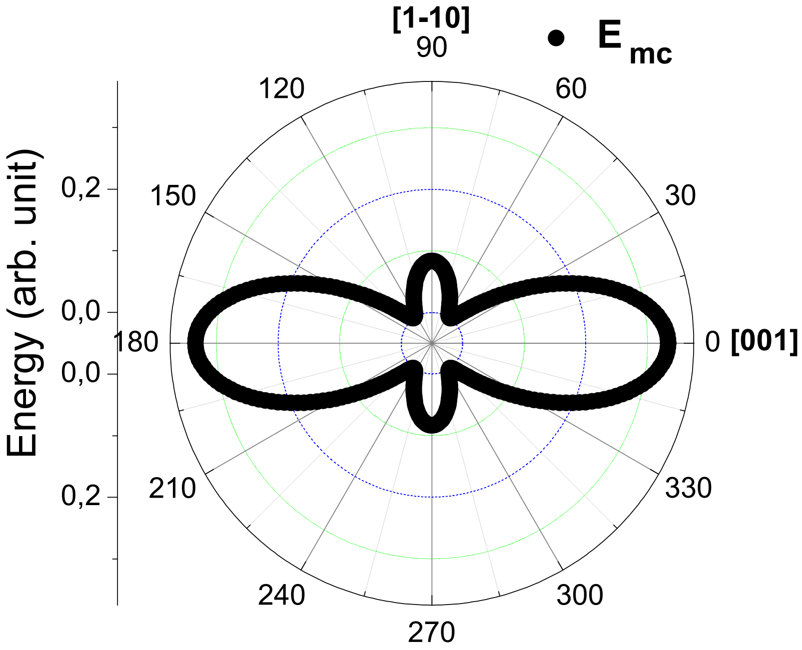

Figure 4.13: The simulated polar diagram of the magnetocrystalline energy in the (110) plane by using the equation $\frac{1}{4}K_1(\sin^4\phi + \sin^2 2\phi)$. It yields an anisotropy with the hard axis along the [001] direction and easy axis between the [001] and [$1\bar{1}0$] directions.

The experimental data can be well described by fitting the torque curve with the expression of Eq. 4.6 in Fig. 4.12. This suggests that the uniaxial in-plane anisotropy of (110) oriented LCO thin films is caused by the magnetoelastic anisotropy with easy and hard axes along the [001] and [$1\bar{1}0$] directions, respectively. It is possible to estimate the ratio between B_1 and B_2 from the fitting in Fig. 4.12. Taken the value of B_1 as determined in the previous section, this leads to B_2=4.3x10^7 erg/cm^3. By using B_1, B_2 and $\epsilon_0 = 0.007$ (extracted from x-ray diffraction measurements), the magnitude of the uniaxial in-plane anisotropy, $E_a^{ip} = E([1\bar{1}0]) - E([001])$=8.8x$10^5$ erg/cm^3.

The in-plane and out-of-plane plane hysteresis loops of (110) oriented LCO/LSAT films are shown in Fig. 4.14. Surprisingly, the out-of-plane magnetization shows remanence and reaches saturation. This observation is significantly different that of (001) oriented films. The different behavior of (110) films can be ascribed to the fact that there is no strong anisotropy between the [001] and the [110] directions. Since the shape anisotropy favors in-plane magnetization, it can be speculated that the dominating magnetoelastic anisotropy causes observed behavior. The resulting out-of-plane anisotropy amounts to $E_a^{op} = E([110]) - E([001])$=3x$10^5$ erg/cm^3, which is an order of magnitude smaller than that of the out-of-plane anisotropy of (001) oriented films. Therefore, we were able to record a full hysteresis loop for the out-of-plane direction of (110) oriented film. In Fig. 4.15 we simulated $E_{tot}^{(110)}$ using the extracted experimental values.

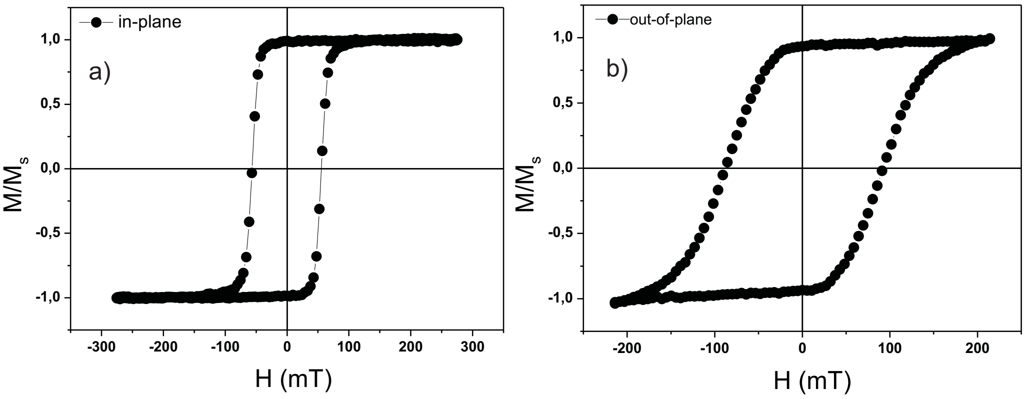

Figure 4.14: Hysteresis loops of a (110) oriented LCO/LSAT thin film taken by longitudinal and polar MOKE magnetometry. a) In-plane loop, field applied along the [001] direction. b) Out-of-plane loop, field applied along the [110] direction.

(111) oriented thin films

We also investigated the in-plane magnetic anisotropy of (111) oriented LCO/LSAT thin films. The torque measurements shown in Fig. 4.16 revealed that there is no magnetic anisotropy in the (111) film plane. This is actually expected considering the energy expressions derived for (111) oriented films in the Appendix. The Eq. 6.18 and 6.19 reflect that the magnetocrystalline and magnetoelastic energies are isotropic in the (111) film plane, which is consistent with our torque data. As for the out-of-plane anisotropy, from Eq. 6.18 and 6.19 $E_a^{op} = E([111]) - E([\frac{-1}{\sqrt{2}}, \frac{1}{\sqrt{2}}, 0]$ is expected to be small because the magnetoelastic anisotropy favors the out-of-plane magnetization whilst shape anisotropy favors in-plane magnetization with similar magnitudes. However, the in-plane and out-of-plane hysteresis loops, shown in Fig. 4.17, suggest that [111] direction is the hard axis while the film plane is the easy plane with a relatively strong anisotropy. This inconsistency may be clarified by the fact that the FWHM of the rocking curve of (111) oriented films was larger than that of (001) and (110) oriented LCO films. Moreover, the Curie temperature, $T_C = 30$K, is significantly reduced in comparison to other oriented films. Those results might indicate that strain in (111) oriented films is strongly relaxed. This probably leads to non-homogeneous strain field which possibly may affect the magnetic anisotropy and might be the reason for the inconsistence between the expected and observed out-of-plane anisotropy in (111) oriented LCO films.

4.2.2 Discussion and conclusion

We observed experimentally a biaxial in-plane anisotropy of (001) oriented LCO/LSAT epitaxial thin films with [110] easy and [100] hard axes, respectively. According to energy expressions only the cubic magnetocrystalline energy is anisotropic in the (001) film plane of the strained LCO thin films if the cubic crystal symmetry is assumed.

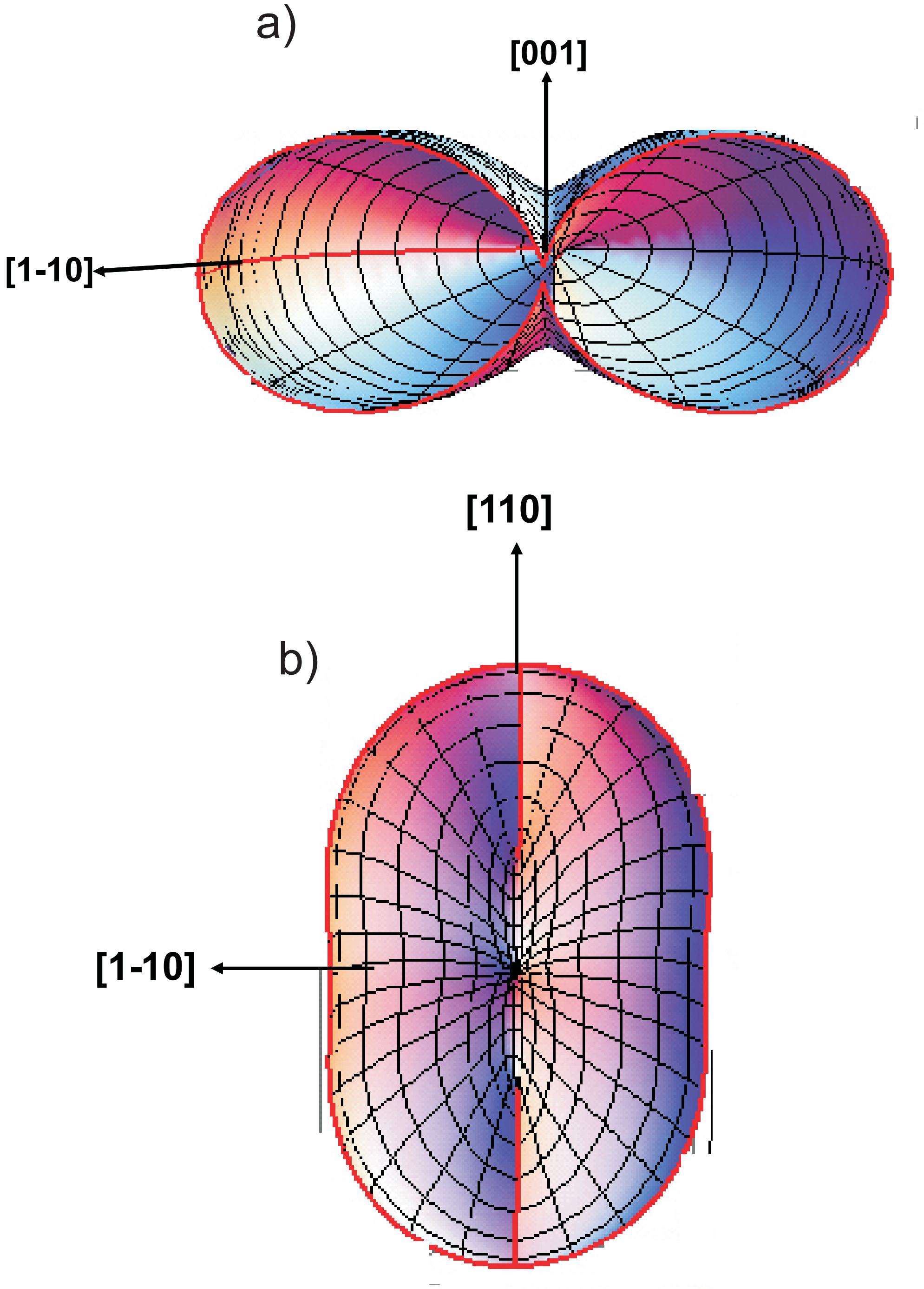

Figure 4.15: Anisotropy energy for 30 nm (110) oriented tensile strained LCO/LSAT thin film calculated using the experimental values. a) A cut through the energy surface parallel to the film plane showing the presence of uniaxial anisotropy in the (110) plane. b) A cut the energy surface perpendicular to the film plane showing the presence of weak anisotropy between the out-of-plane ([110]) and in-plane direction ($[1\bar{1}0]$).

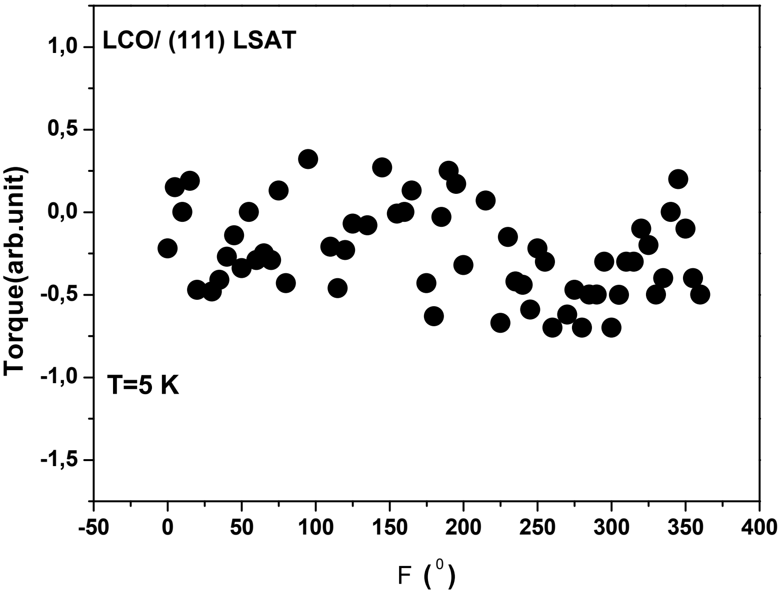

Figure 4.16: Torque curve of a (111) LCO/LSAT film at 5 K. The field is varied in the film with the step of Φ.

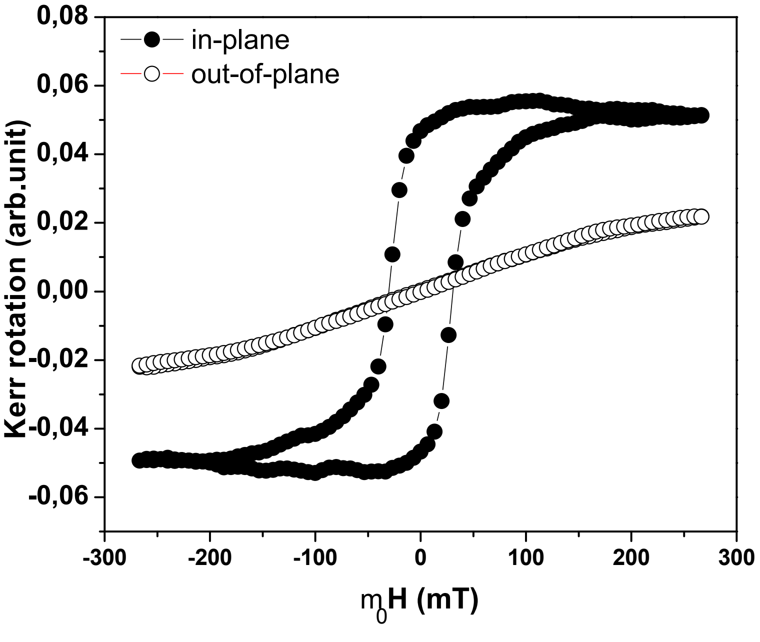

Figure 4.17: Hysteresis loops of a (111) oriented LCO/LSAT film taken at 12 K.

In section 4.1, we have discussed that the tensile strained epitaxial LCO films can be considered having pseudocubic crystal structure, which allows us to assume cubic symmetry. We show that a cubic magnetocrystalline anisotropy with K_1= -1.2x10^4 erg/cm^3 can explain the origin of the biaxial in-plane anisotropy of (001) oriented LCO films. To a certain degree, cobaltates may appear similar to the manganites concerning structural aspects. Steenbeck et al. [37] reported biaxial in-plane magnetic anisotropy with easy and hard axes along the [110] and [100] directions, respectively, in (001) oriented $La_{0.7}Sr_{0.3}MnO_3$ (LSMO) thin films grown on STO substrate. A very similar result has been reported by Lodder *et al.* [39]. They described the symmetry of their magnetic anisotropy in terms of a dominating cubic crystal anisotropy constant $K_1 < 0$, superimposed with a small uniaxial anisotropy induced by anisotropic stress. In contrast to those results, Suzuki *et al.* [139] reported a [100] easy axis and a [110] hard axis in LSMO thin films. In that work, the 4-fold symmetry was explained by a dominant contribution from the strain induced anisotropy. The influence of the substrate symmetry and the strain state on the in-plane magnetic anisotropy of L(S,C)MO thin films were discussed extensively in the literature [140–142]. Although several groups agreed that the observed biaxial magnetic anisotropy in the (001) plane of LSMO thin films can be described by an intrinsic magnetocrystalline anisotropy, there is no general consensus on the reason for the scatter of the sign and magnitude of the anisotropy constant, K_1. We extracted K_1 ≈-1.2x10^4 erg/cm^3 of LCO films for the temperature of $T/T_c = 0.7$, which is comparable to that of LSMO epitaxial thin films where K_1 ≈-1.4x10^4 erg/cm^3 for $T/T_c = 0.2$. Since magnetocrystalline anisotropy becomes stronger at lower temperatures, as shown in Fig. 4.8, it is likely that K_1 of LCO is larger than that of LSMO at the same reduced temperature.

A strong anisotropy between the film plane and the c axis direction was observed in (001) oriented LCO films. The large B_1 ≈-8.7x10^7 erg/cm^3 seems to be the reason for that. The negative sign of B_1 implies that magnetoelastic anisotropy favors in-plane magnetization adding to the shape anisotropy. By comparing the magnitude of the individual anisotropy contributions, we can claim that the large value of B_1 leads to the dominant role of the magnetoelastic anisotropy over the other anisotropy contributions. Since both shape and magnetoelastic anisotropies impose the magnetization to lie in the film plane for (001) films, the superposition of them causes a strong out-of-plane hard axis. The large anisotropy between the [001] and [100] directions explains why we could not record hysteresis loops for out-of-plane direction. There are several groups reporting the presence of a strong magnetoelastic anisotropy via a large B_1 in perovskite thin films. O'Donnell *et al.* [143] calculated B_1=-6.7x10^7 erg/cm^3 for epitaxial LCMO thin films. By neglecting the strain dependence of B_1, which brings about a small second order correction term, D, $(B_1^{eff.}(\epsilon) = B_1 + D.(\epsilon))$, we can argue that magnetoelastic coefficients of LCO and LSMO epitaxial thin films are comparable. In particular, the results suggest that magnetic anisotropy can be switched from in-plane to out-of-plane if a strong compressive strain is introduced to (001) oriented LCO thin films.

We observed a uniaxial anisotropy in the plane of (110) oriented LCO thin films. The observed uniaxial in-plane anisotropy with the easy and hard axes along the [001] and [$1\bar{1}0$] directions, is induced by the magnetoelastic anisotropy. Suzuki *et al.* [139] also reported a uniaxial anisotropy in the plane of tensile strained (110) oriented LSMO thin films, which was explained by magnetoelastic anisotropy. However, the out-of-plane anisotropy in the (110) oriented films is much less that that of (001) oriented films. This can be explained by the presence of shear strain components in (110) oriented films which lead to an additional contribution to the magnetoelastic anisotropy via the anisotropy constant B_2, see Eq. 6.14 and 6.15. Since $B_2 > 0$, this contribution will compete with the shape anisotropy and thus diminish the overall out-of-plane anisotropy. In the film plane of (111) oriented films we did not observe any anisotropy, which is consistent with the energy calculations estimating that magnetoelastic anisotropy and magnetocrystalline anisotropy are isotropic in the (111) plane.

In conclusion, we have shown that magnetic anisotropy in epitaxial LCO thin films can be manipulated by changing the epitaxial strain and the film orientation.

4.3 The time dependence of magnetization

There is only little work concerning magnetic relaxation of epitaxial thin films. Especially, there is no study on the time dependence of the magnetization of LCO. Since the magnetic after-effect is strongly affected by the distribution of the energy barriers, ΔE, it is of special interest if the magnetization relaxation is affected by epitaxial strain. For that reason, we have investigated the time dependence of the magnetization of differently strained LCO films in order to reveal possible systematic correlation between the time dependence of the magnetization and epitaxial strain.

The experiments were performed on (001) oriented thin films with different strain, i.e., LCO/SLAO ($\epsilon_0 \approx 0.1\%$), LCO/SLGO ($\epsilon_0 \approx 0.5\%$), and LCO/LSAT ($\epsilon_0 \approx 1.1\%$). The experimental procedure was applied as follow: The thin film was cooled down from room temperature to the target temperature where the measurements were done. Then, a DC magnetic field of 7 Tesla was applied along the film plane for 30 minutes. After that, a reverse field, H_r, is applied in the opposite direction, and the evolution of the magnetization $M(H_r, T, t)$ of the film was measured over a time period of approximately 10^4 s. The time dependence of the magnetization was measured for $0.2H_c < H_r < 2H_c$. The measurement routine was also repeated for different target temperatures between 20 and 60K.

4.3.1 Results

Figure 4.18 shows the variation of the magnetization of the LCO/SLAO versus ln(t) ($\epsilon_0 \approx 0.1\%$) for different values of H_r and temperatures ranging between 20-60 K. For our analysis we have only used the data from 60 to 12.000 s, since the SQUID magnetometer needs some time to achieve field stability after setting the reverse field. First we have tried to fit the data in Fig. 4.18 with Eqs. 2.10 and 2.9, which was not successful. The data can be much better described by the logarithmic decay model, $M(t) = M_0 + S_0\ln(t) + S_1\ln^2(t) + ...$, described in section 2.4.4. It should be pointed out that the data can be fitted quite well by using only the first-order expansion of Eq.

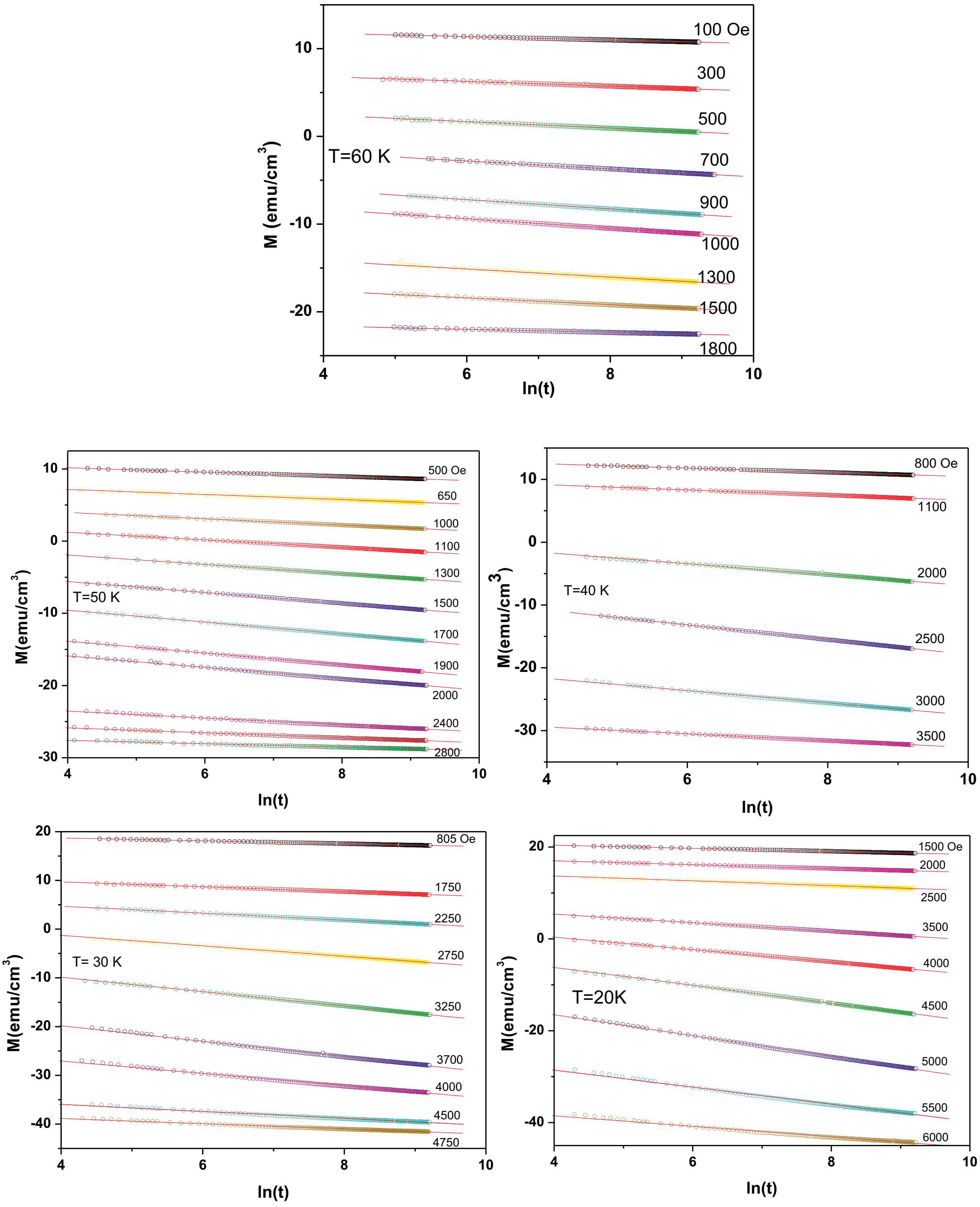

Figure 4.18: M versus ln (t) for LCO/SLAO that has only a small tensile strain, $\epsilon_0 \approx 0.1\%$, for different temperatures between 60 and 20 K. The different colors represent data taken at different reverse fields. The solid lines are fits to the data using $M(t) = M(0) + S_0 \ln(t)$.

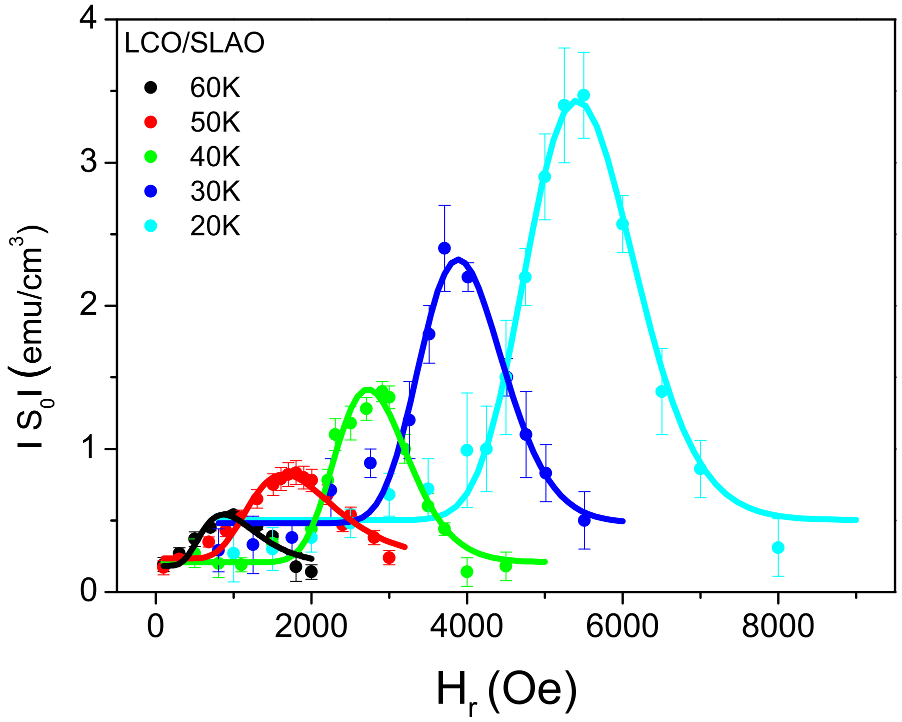

Figure 4.19: Magnetic viscosity coefficient, $|S_0|$, of LCO/SLAO film as a function of reversed field H_r at different temperatures. The solid lines are fits to the data with log-normal functions.

2.18 and neglecting higher orders. Since all $M(H_r, T, t)$ measurements obey the ln(t) law, it can be deduced that $f(\Delta E)$ for LCO/SLAO is broad (σ is large). However, small deviations from linear behavior are observable for temperatures below 20 K. This might be attributed to the fact that σ becomes smaller as temperature decreases.

In Fig. 4.19 we show magnetic viscosity coefficient, $|S_0|$, values plotted as a function of reverse field H_r for different temperatures. The curves are bell-shaped and the maximum is obtained around H_c. Based on an analytical model proposed by Chantrell et al. [72] (see Eq. 2.16) we fitted the curves with the following equation

$$S_0 = \frac{\partial M(t)}{\partial \ln(t)} = \frac{AkT}{\Delta E_m} f(y) \tag{4.7}$$

$$f(y) = \frac{1}{\sqrt{2\pi}\sigma y} exp\left(-\frac{1}{2}\left(\frac{\ln(y/y_c)}{\sigma}\right)^2\right) \tag{4.8}$$

$$\Delta E = KV_{sw}(1 - H_r/H_k)^2 \tag{4.9}$$

$$y_c = \frac{\Delta E_c}{\Delta E_m}, \quad y = \frac{\Delta E}{\Delta E_m}, \quad \Delta E_c = kT\ln(t/\tau_0) \tag{4.10}$$

where ΔE_m is the median energy barrier and $f(y)$ is the log-normal energy barrier

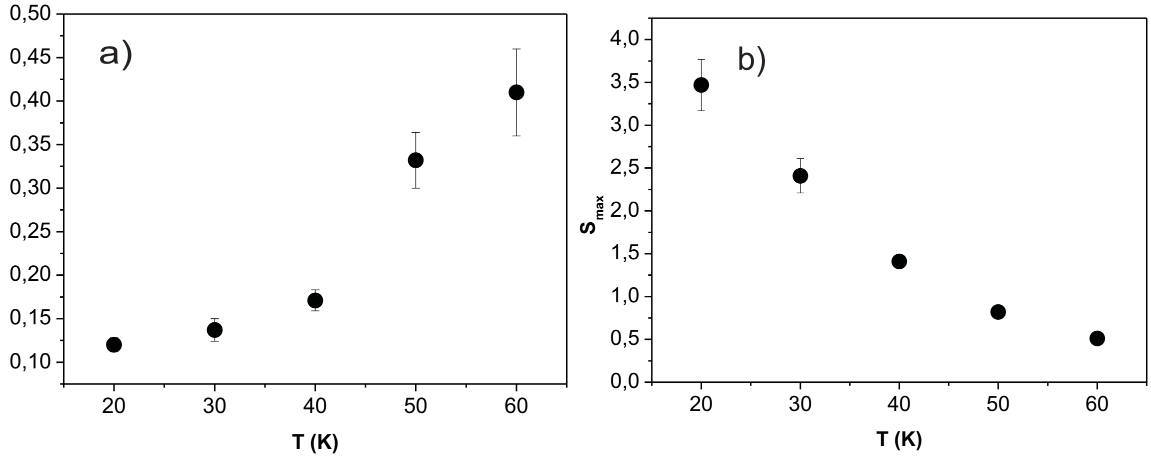

Figure 4.20: a) σ values, as extracted from fitting of $|S_0|$ vs. H_r (see Fig. 4.19), as a function of T. b) Maximum values, S_{max}, of first-order magnetic viscosity, $|S_0|$, for different temperatures.

distribution function. K and H_k are anisotropy constant and anisotropy field. V_{sw} is the switching volume of a Stoner-Wohlfarth particle [144]. The width σ is treated as the fitting parameter. The fitted curves (solid lines) match the experimental results quite well. This means that the energy barrier distribution function, $f(\Delta E)$, can be well described by a log-normal function. We also display σ values as extracted from the fits for different temperatures in Fig. 4.20a. The width, σ, of the distribution function becomes smaller as the temperature decreases. This reflects the observation that at low temperatures a small non-linearity in $M(t)$ vs ln(t) is observable for LCO/SLAO films, which also hints at some narrowing of the energy distribution function (see sec. 2.4.4). The maximum $|S_0|$ values (S_{max}) increase as temperature decreases as shown in Fig. 4.20b.

In the following, measurements performed on LCO/SLGO films are presented. As mentioned before, LCO/SLGO films accommodate tensile strain of about $\epsilon_0 \approx 0.5\%$ with a Curie temperature $T_c = 69$K. The variation of the magnetization versus ln(t) is shown in Fig. 4.21 for different temperatures. The behavior of $M(t)$ versus ln(t) is slightly different from that of LCO/SLAO. The curves show a stronger non-linearity and in addition to S_0 the second term of the expansion S_1 has to be considered for a satisfactory fitting. The solid lines are fits to the data points by using $M(t) = M(0) + S_0\ln(t) + S_1\ln^2(t)$. Similar to LCO/SLAO the magnitude of non-linearity in $M(t)$ vs $\ln(t)$ increases as the temperature decreases. The non-linearity in M versus ln(t) for LCO/SLGO is shown in more detail in Fig. 4.22, where $M(t)$ is recorded for different H_r at 25 K. Note that $M(t)$ is concave downwards for $H_r < H_c$, and concave upwards for $H_r > H_c$ with a cross-over for $H_r \approx H_c$. This observation matches the theoretical work of Hilo *et al.* [82, 145], in which they predicted such a behavior of $M(H_r, t)$ for a narrow log-normal distribution function of the energy barriers (See section 2.4.4). In Fig. 4.23 we display the second-order magnetic viscosity coefficients, $|S_1|$, of LCO/SLAO and LCO/SLGO films, which is a measure of the non-linearity of the $M(t)$ versus $ln(t)$ curves at 20 K. Obviously, the magnitude of the non-linearity

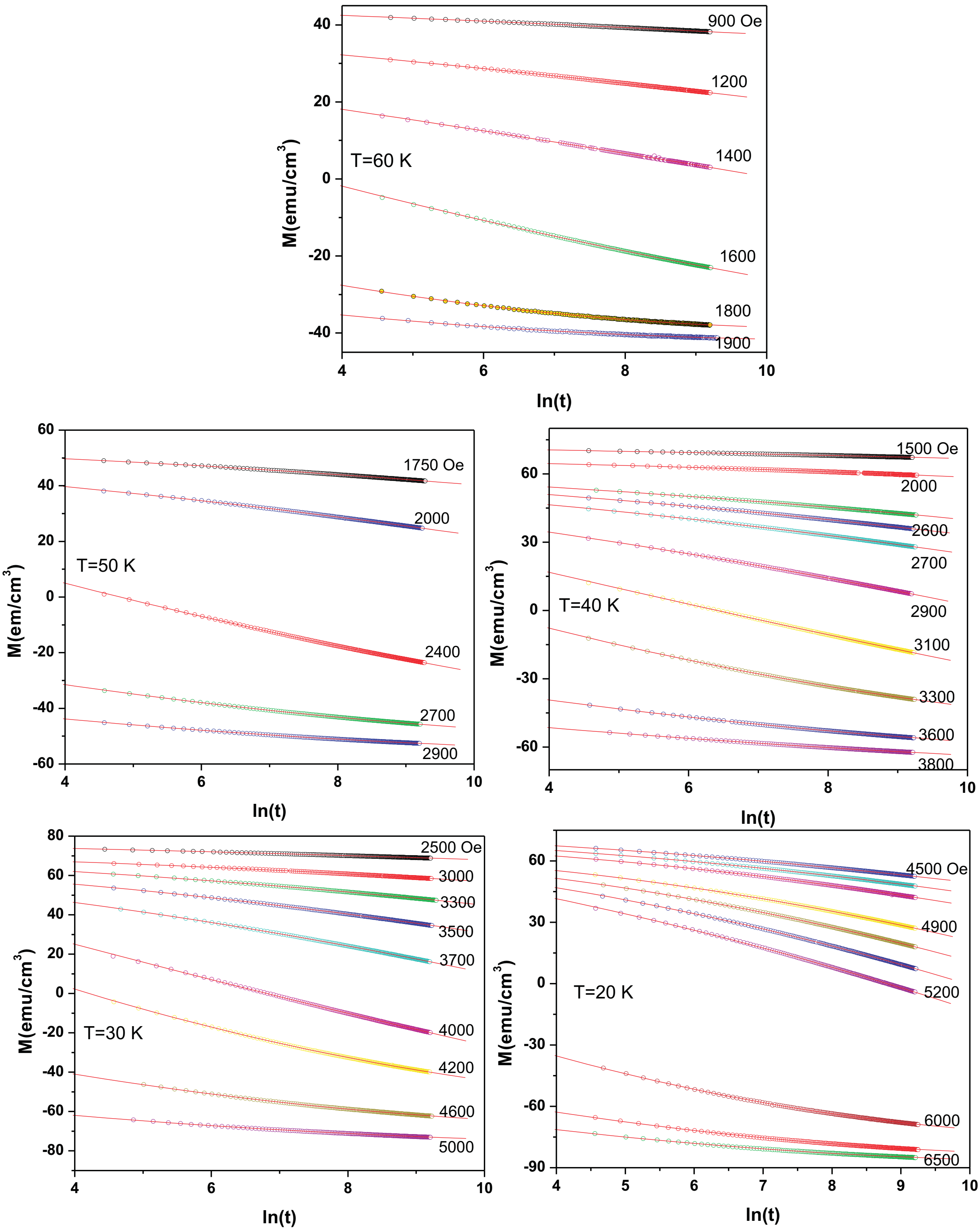

Figure 4.21: M versus ln (t) for LCO/SLGO ($\epsilon_0 \approx 0.5\%$) for different temperatures between 60 and 20 K.The different colors represent data taken at different reverse fields. The solid lines are fits of the form $M(t) = M(0) + S_0 \ln(\mathrm{t}) + S_1 \ \ln^2(t)$.

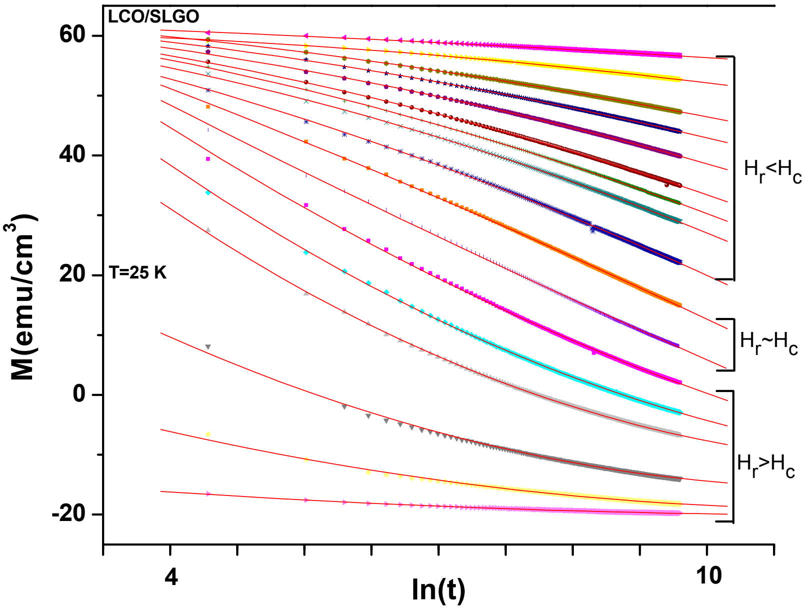

Figure 4.22: $M(t)$ versus ln(t) curves for LCO/SLGO ($\epsilon_0 = 0.5\%$) at 25 K. The applied reverse field, H_r, increases from top to bottom.

in LCO/SLGO is higher than that of LCO/SLAO. Since the magnitude of the non-linear terms in the series expansion depends on the width of the distribution function, i.e.,$|S_n| \propto (1/\sigma^2)^n$, LCO/SLGO films have likely a narrower $f(\Delta E)$ compared to LCO/SLAO films. We also plot $|S_0|$ as a function of H_r for different temperatures in Fig. 4.24. Similar to LCO/SLAO, the curves could be fitted well with a log-normal function.

The maximum viscosity, S_{max}, and the width, σ, of the fitted log-normal functions as a function of temperature are plotted in Fig.4.25. The width, σ, decreases, while S_{max} increases, with decreasing temperature. The same trend has been observed for LCO/SLAO films. We have performed measurements on LCO/LSAT ($\epsilon_0 = 1.1\%$) films as well. The non-linearity in M vs. ln(t) curves was observed similar to that of LCO/SLGO. $|S_0|$ vs. H_r curves are shown in Fig. 4.26. The data were fitted with a log-normal function. The width, σ, of the log-normal functions decreases, and S_{max} increases with decreasing temperature, which seems to be a common feature of all films.

In order to elucidate the influence of the strain on $f(\Delta E)$ and the magnetic viscosity, we plot $|S_0|$ vs. H_r/H_c for differently strained films at 30 K in Fig. 4.27. The width, σ, of the corresponding log-normal function decreases with strain. Since $|S_0|$ vs. H_r/H_c represents $f(\Delta E)$ at a given temperature, $f(\Delta E)$ becomes narrower with tensile strain. This is shown in Fig. 4.28a. Furthermore, Fig. 4.28b demonstrates S_{max} as a function of ϵ which obviously increase with strain.

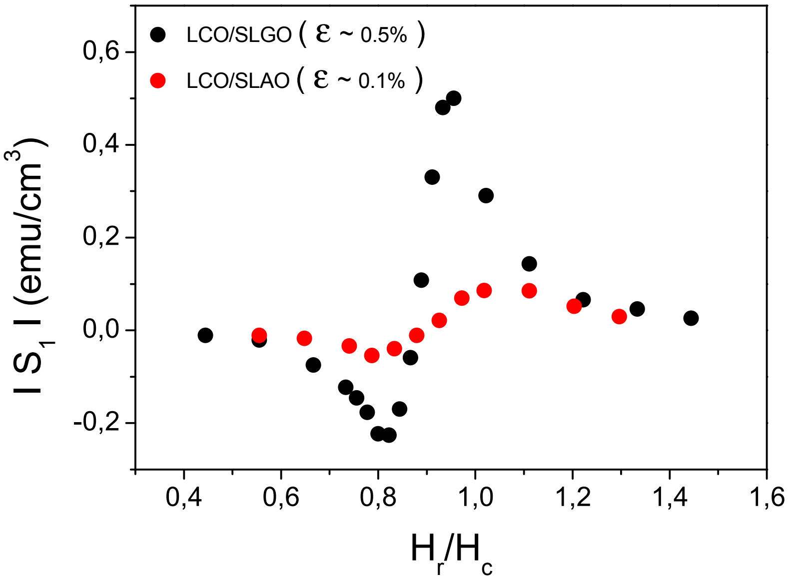

Figure 4.23: $|S_1|$ vs. H_r/H_c for the LCO/SLAO and LCO/SLGO films.

4.3.2 Discussion and conclusion

Existence of the distribution of the energy barriers described by a log-normal function

By following the model introduced by Hilo et al. [41, 82, 145], and expanded by Chantrell et al. [72], the variation of $M(H_r, t, T)$ as a function of ln(t) in LCO thin films indicates that there is an apparent distribution of the energy barriers. The distribution of energy barriers is a fundamental part of all systems. In real systems there is always a distribution of relaxation times brought about by a distribution of ΔE which can arise from the differences in the local anisotropy, grain size, defects etc. Moreover, by fitting $|S_0|$ vs. H_r we deduce that $f(\Delta E)$ can be described well by a log-normal function. Then, the arising question is the origin of the log-normal distribution of energy barriers in LCO thin films. Indeed, the existence of log-normal $f(\Delta E)$ was reported in several magnetic systems [85,144]. For instance, an assembly of nano-sized magnetic particle systems exhibits statistically a log-normal $f(\Delta E)$, which is caused by the volume distribution of the particles [84,146]. However, its origin in ferromagnetic thin films is still an open question. According to the random anisotropy model [147], anisotropy could be different in the each grain locally, thus, a log-normal $f(\Delta E)$ can be expected. Similarly, a statistical distribution of grains in the LCO films might cause a log-normal distribution of energy barriers. Future experiment can be performed to reveal any relation between the structural properties and $f(\Delta E)$ in LCO films.

Strain and temperature dependence of $f(\Delta E)$

The variation of $M(t)$ of LCO/SLAO film ($\epsilon \approx 0.1\%$) follows a linear trend. This linear dependence on ln(t) results from a broad (large σ) distribution of energy barriers, which was analytically proved by Street and Woolley [148]. For the higher strained LCO/SLGO and LCO/LSAT non-linearities arise in $M(t)$ vs. ln(t) curves. This can be attributed to a narrowing of the energy barrier distribution with tensile strain.

A possible way to discuss the influence of the strain on $f(\Delta E)$ is to consider the effect of the magnetic interactions on $f(\Delta E)$. Lee $et al.$ [149] revealed a strong influence of the magnetic interactions, such as exchange and magnetostatic interactions, on the distribution of energy barriers inferred from the time dependence of magnetization of a magnetic thin film by micromagnetic and Monte-Carlo simulations. They showed that the shape of $f(\Delta E)$ is significantly changed with varying magnetic interactions which he parameterized by $h_e = \frac{A}{K_u D^2}$ (A is the effective exchange constant, D is a grain diameter, and K_u is the uniaxial anisotropy energy density). He showed that if h_e is strong then $f(\Delta E)$ has a broad distribution, and the magnetization decay with time shows a linear dependence on ln(t). Indeed, the uniaxial anisotropy in (001) oriented films is equal to E_a^{op}, and, then, K_u is dependent on strain. That is, K_u increases by increasing strain due to the increase of the uniaxial magnetoelastic anisotropy. Thus, h_e

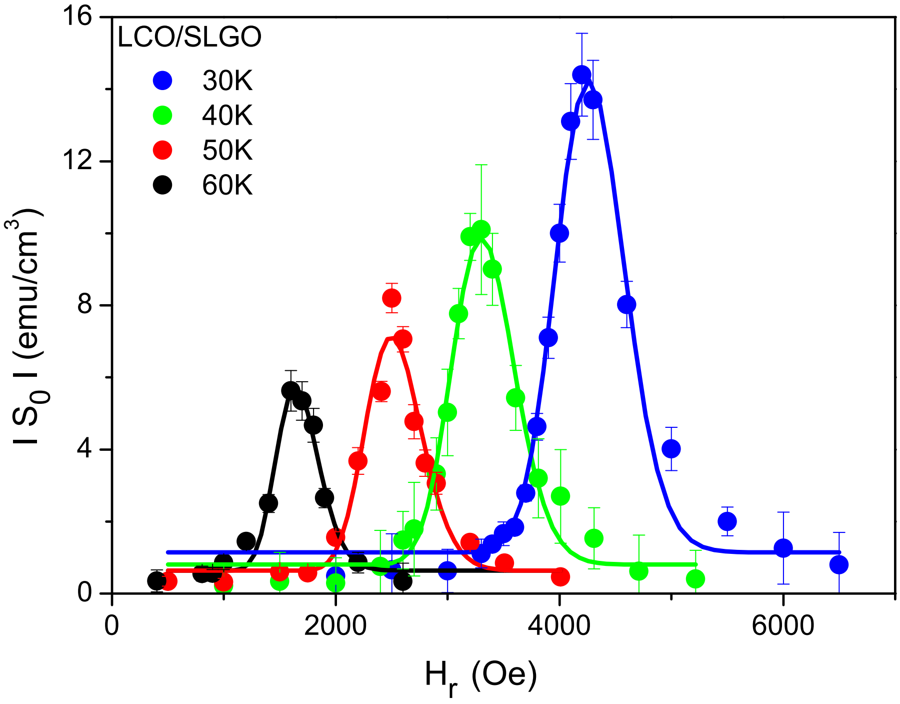

Figure 4.24: $|S_0|$ values of LCO/SLGO film as a function of reversed field H_r at different temperatures. The solid lines are fits to the data with a log-normal function.

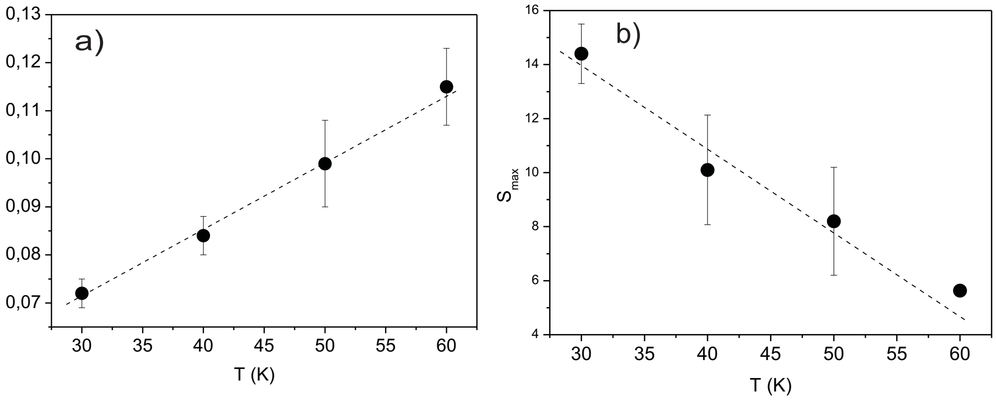

Figure 4.25: a) σ values as extracted from the fits in Fig. 4.24 vs. temperature. b) Maximum values of first-order magnetic viscosity, $|S_0|$, for different temperatures. Dashed lines are guide to the eye.

is largest for LCO/SLAO films, and exhibits the linear decay with ln(t) over the largest range due to the broadened $f(\Delta E)$. As the strain increases, h_e decreases resulting in a narrower $f(\Delta E)$, which explains the non-linearities in the $M(t)$ vs. $ln(t)$ curves of LCO/SLAO and LCO/LSAT films.

The temperature dependence of σ can be quantatively explained in a similar way. The magnetoelastic constant, B_1, generally increases with decreasing temperature,

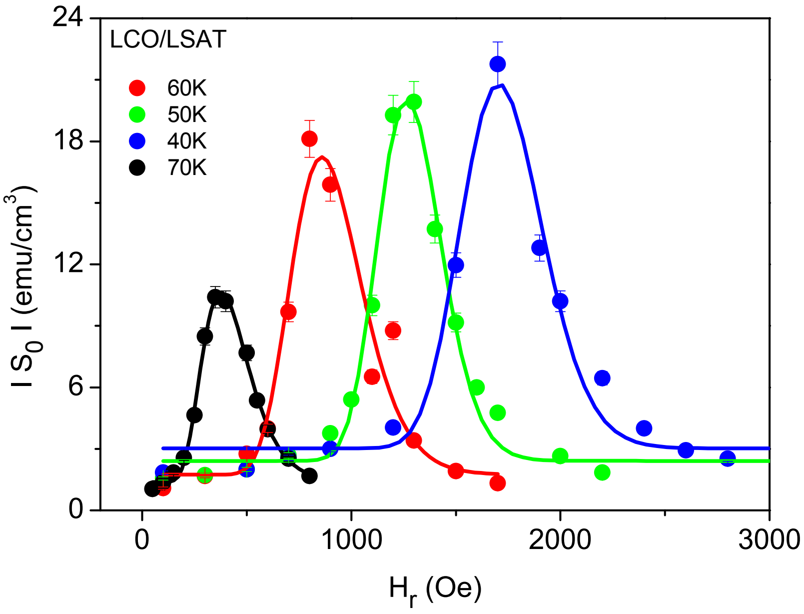

Figure 4.26: $|S_0|$ vs. H_r for LCO/LSAT at different temperatures. The solid lines are fits to the data with a log-normal function.

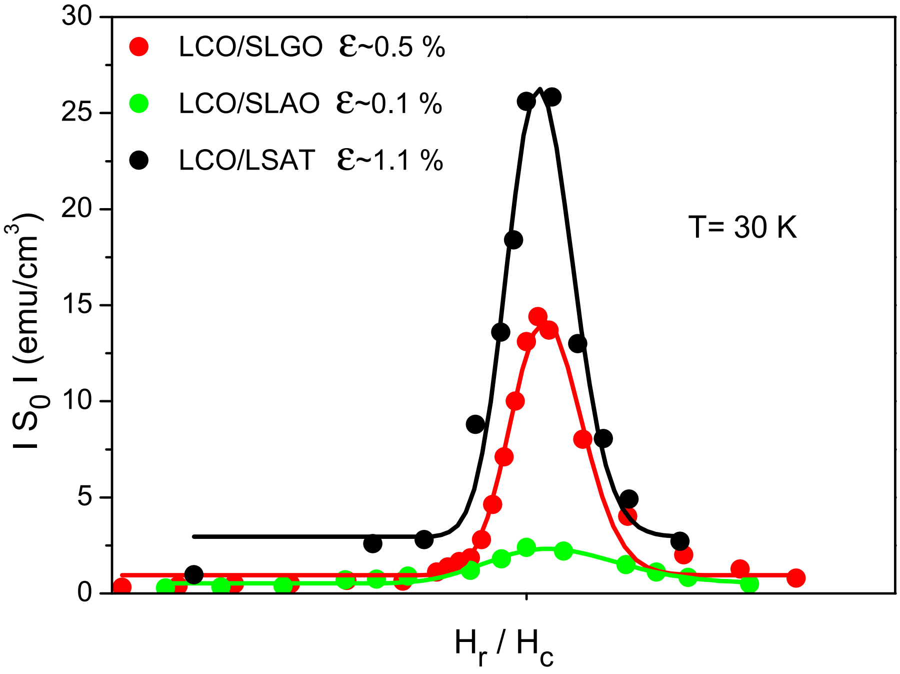

Figure 4.27: $|S_0|$ vs. H_r/H_c curves for 3 differently strained LCO films. The solid lines are fit to the data with log-normal functions.

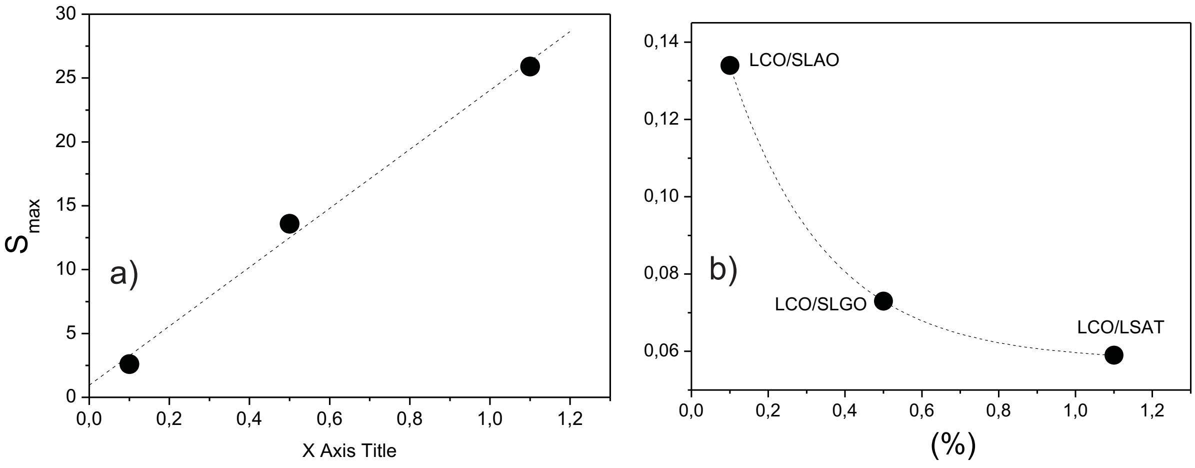

Figure 4.28: a) σ values extracted from fits in Fig. 4.27 vs. strain. b) S_{max} values extracted from Fig. 4.27 vs. strain. Dashed lines are guide to the eyes.

which brings about the increase of K_u (magnetoelastic anisotropy is proportional to B_1). Hence, the strength of the effective exchange interaction, h_e, decreases with temperature causing narrower distribution of energy barriers.

Strain and temperature dependence of S_{max}

Larger S implies a larger change in the magnetization during the observed time period. We observed that the magnetic viscosity increases with both decreasing temperature and increasing tensile strain. Normally, one would expect that S_{max} should decrease with decreasing temperature due to the less thermal energy (less thermally activated relaxation). Yet, it seems that the decrease of the S_{max} caused by thermal loss is compensated by the increase of M. The ferromagnetic fraction in LCO films increases with increasing strain [24], which results in the increase of S_{max}.

In conclusion, we evidenced the existence of a possible energy barrier distribution of LCO films which can be described by a log-normal function. The width, σ, of $f(\Delta)$ decreases with increasing strain.

Chapter 5

Summary

In this thesis, magnetic properties such as the magnetic anisotropy and magnetic aftereffect of strained ferromagnetic $LaCoO_3$ (LCO) thin films were studied. To figure out possible correlations between epitaxial strain and magnetic properties differently strained LCO films were grown epitaxially by pulsed laser deposition on various single crystal substrates with different lattice constants.

The magnetic properties of the films were investigated predominantly by magneto-optical Kerr effect (MOKE) magnetometry. To this purpose an apparatus for measuring MOKE and carrying out Kerr microscopy was built. The system allows measurements in the temperature range from 4.2 to 500 K in magnetic fields up to 300 mT in the longitudinal mode and 200 mT in the polar mode. The spatial resolution of the microscope is limited to about 5 μm.

The Curie temperature,T_c, and saturation magnetization, M_s, increase with increasing tensile strain. The increase of T_c may be explained by an increase of the Co-O-Co bonding angle with increasing tensile strain which leads to a decrease of the hybridization of t_{2g}- states with neighboring O $2p$ states and thus to an increased exchange splitting.

The increase of the magnetic moment and thus M_s is due to an increased population of higher spin states, i.e., high-spin and intermediate-spin states which is possibly caused by a decrease of the crystal-field splitting with increasing tensile strain.

We observed experimentally a biaxial in-plane anisotropy energy (E_a^{ip} $\approx$0.3x10^4 erg/cm^3) of (001) oriented LCO/LSAT epitaxial thin films with $< 110 >$ easy and $< 100 >$ hard axes, respectively. This is explained by a magnetocrystalline anisotropy constant, K_1=-1.2x10^4 erg/cm^3, where the sign of K_1 determines the direction of the easy axis. Hysteresis loops of (001) oriented films along the out-of-plane direction were not observed. Also, the magnetization can not saturate even at 7 T applied field along the c axis. This hints a strong anisotropy between the film plane and the c axis, and is explained by the large magnetoelastic anisotropy. The measured B_1=-8.7x10^7 erg/cm^3 indicates that a large magnetoelastic anisotropy adds to the shape anisotropy and strongly favors in-plane magnetization. The summation of both causes a large anisotropy, E_a^{op} $\approx$2.0x10^6 erg/cm^3, between the film plane and the c axis.

A uniaxial in-plane anisotropy (E_a^{ip} ≈8.0x10^5 erg/cm^3) is found in (110) oriented films, which is explained by a magnetoelastic anisotropy with easy and hard axes along the [001] and [1$\bar{1}$0] directions, respectively. In contrast to (001) oriented films, a strong out-of-plane anisotropy in (110) films does not exist. The out-of-plane magnetization shows remanence and reaches saturation. This can be explained by the presence of a shear strain component of the magnetoelastic anisotropy ($B_2 \approx$ 4.3x10^5 erg/cm^3) in (110) oriented films. The contribution favors an out-of-plane magnetization, and competes with the shape anisotropy leading to a decrease of out-of-plane anisotropy (E_a^{op} ≈3.0x10^5 erg/cm^3), which is an order of magnitude smaller than that of (001) oriented films.

An isotropic in-plane magnetization is found for (111) oriented films. This is expected considering the energy expressions, which predict that magnetocrystalline and magnetoelastic energies are isotropic in the (111) film plane.

The time-dependent magnetization measurements performed on the differently strained LCO films, are analyzed in the frame work of the model of El-Hilo *et. al.* [41, 82]. It is found that there is an apparent distribution of energy barriers, which is a common feature of real systems. The $M(t)$ vs. $\ln(t)$ curves exhibit a linear behavior for LCO/SLAO films while non-linearities arise for LCO/SLGO and LCO/LSAT films, which are attributed to a narrower distribution of energy barriers. It is shown that the distribution function, $f(\Delta E)$, can be described by a log-normal function. This might be caused by a statistical distribution of the local magnetic anisotropies or magnetic domain sizes in LCO films.

The distribution, $f(\Delta E)$ becomes narrower with increasing strain, which can be explained by considering the effect of the magnetic interactions on the shape of the $f(\Delta E)$. Micromagnetic and Monte-Carlo simulations performed by Lee *et. al.* [149] showed that magnetic films with a strong magnetic interaction have a broad barrier distribution and thus show a linear $M(t)$ decay with $\ln(t)$. We suggest that the strength of the interaction decreases with increasing strain via magnetoelastic anisotropy inferred from the fact that the distribution becomes narrower with increasing strain in LCO thin films. Similarly, decrease of the width of $f(\Delta E)$ is interpreted in terms of a decrease of the strength of the effective exchange interaction due to the increase of the anisotropy with decreasing temperature.

Chapter 6

Appendix

The application of anisotropy expressions are formulated for different film coordinate systems in cubic symmetry.

6.1 (001) films

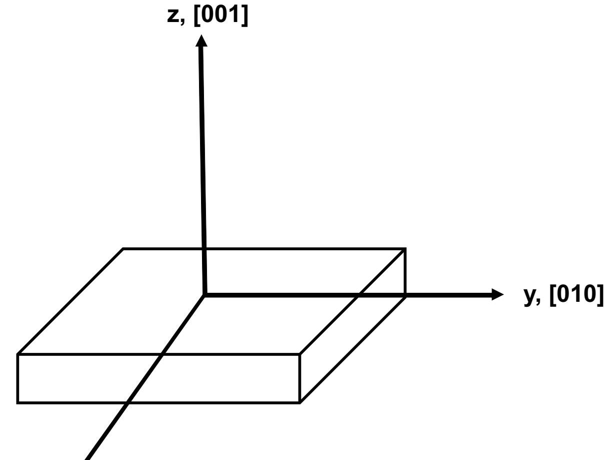

Figure 6.1: The coordinate system for (001) films. The film normal [001] forms the z axis of a cartesian coordinate system.

The geometry of the (001) films is shown in Fig. 6.1. The surface normal is chosen as z axis of a cartesian coordinate system. The directional cosines with respect to this appropriate system

$$\begin{aligned} \alpha_1 &= \sin\Theta\cos\Phi \\ \alpha_2 &= \sin\Theta\sin\Phi \\ \alpha_3 &= \cos\Theta \end{aligned} \tag{6.1}$$

Here $\alpha_1, \alpha_2, \alpha_3$ are the direction cosines of the magnetization vector with respect to x, y and z axes and Φ and Θ are the polar angles measured from x and z axes, respectively. As considering the relation $\alpha_1^2 + \alpha_2^2 + \alpha_3^2 = 1$, the magnetocrystalline anisotropy energy for cubic symmetry is given by

$$E_{mc} = K_1(\alpha_1^2\alpha_2^2 + \alpha_1^2\alpha_3^2 + \alpha_2^2\alpha_3^2) + K_2(\alpha_1^2\alpha_2^2\alpha_3^2) \tag{6.2}$$

Inserting the direction of cosines in Eq. (6.2) and neglecting K_2, magnetocrystalline anisotropy energy density for (001) oriented films is written as:

$$E_{mc}^{(001)}(\Theta, \Phi) = \frac{K_1}{4}[\sin^4\Theta\sin^2 2\Phi + \sin^2 2\Theta] \tag{6.3}$$

The magnetoelastic energy density for cubic symmetry is given by

$$E_{me} = B_1(\epsilon_1\alpha_1^2 + \epsilon_2\alpha_2^2 + \epsilon_3\alpha_3^2) + B_2(2\epsilon_{12}\alpha_1\alpha_2 + 2\epsilon_{23}\alpha_2\alpha_3 + 2\epsilon_{31}\alpha_3\alpha_1) \tag{6.4}$$

By considering epitaxial growth leading $\epsilon_1 = \epsilon_2 = -\epsilon_3 = \epsilon_0$, and $\epsilon_{ij} = 0$ if $i \neq j$, the magnetoelastic anisotropy energy density as a function of Θ and Φ follows:

$$E_{me}^{(001)}(\Theta, \Phi) = B_1\epsilon_0[(-\cos^2\Theta + \sin^2\Theta] \tag{6.5}$$

also the shape anisotropy energy density is given by

$$E_d = \frac{1}{2}\mu_0 M_s^2 \cos^2\Theta \tag{6.6}$$

The total anisotropy energy density expression for cubic (001) oriented film is sum of the terms above,

$$\begin{aligned} E_{ani}^{(001)}(\Theta, \Phi) = &\frac{K_1}{4}[\sin^4\Theta\sin^2 2\Phi + \sin^2 2\Theta] \\ &B_1\epsilon_0[(-\cos^2\Theta + \sin^2\Theta] + \frac{1}{2}\mu_0 M_s^2\cos^2\Theta \end{aligned} \tag{6.7}$$

6.2 (110) films

The (110) orientation requires that the appropriate tensor transformation is performed, as one of the orthogonal in-plane directions does not coincide with a crystal axis. First, the transformation matrix a is derived from an analysis of the surface geometry in Fig. 6.2. To obtain the elements of the transformation matrix a, the primed film directions, $\acute{x}$,$\acute{y}$,$\acute{z}$ have to be expressed in terms of the crystal directions in Fig. 6.1 x, y, z

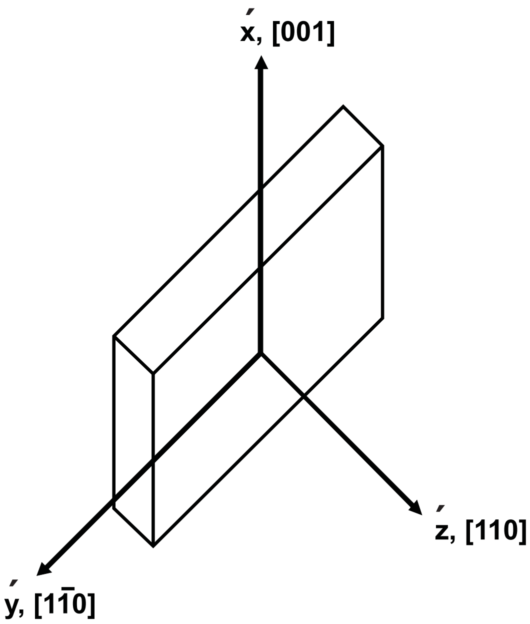

Figure 6.2: The crystal coordinate system for (110) films. The film normal [110] forms the $\acute{z}$-axis of a cartesian coordinate system, while [001] and [1$\bar{1}$0] directions correspond to $\acute{x}$ and $\acute{y}$ axes, respectively.

	x	y	z
$\acute{x}$	0	0	1
$\acute{y}$	$\frac{1}{\sqrt{2}}$	$-\frac{1}{\sqrt{2}}$	0
$\acute{z}$	$\frac{1}{\sqrt{2}}$	$\frac{1}{\sqrt{2}}$	0

as unit vectors. The relations are arranged in form of a matrix, and the elements of a follow directly:

$$a_{ij} = \begin{pmatrix} 0 & 0 & 1 \\ \frac{1}{\sqrt{2}} & \frac{1}{\sqrt{2}} & 0 \\ \frac{1}{\sqrt{2}} & \frac{1}{\sqrt{2}} & 0 \end{pmatrix} \tag{6.8}$$

Now, the tensor transformation can be performed using the the relations below,

$$\alpha_i = \sum_{j=1}^{3} a_{ji}\,\acute{\alpha}_j, \quad \epsilon = a^T\,\acute{\epsilon}\,a \tag{6.9}$$

$$\begin{aligned}\alpha_1 &= \frac{1}{\sqrt{2}}\,(\alpha'_2+\alpha'_3)\\ \alpha_2 &= \frac{1}{\sqrt{2}}\,(-\alpha'_2+\alpha'_3)\\ \alpha_3 &= \alpha'_1\end{aligned}$$

$$\epsilon_{ij}=\begin{pmatrix}\frac{1}{2}(\epsilon'_2+\epsilon'_3) & \frac{1}{2}(-\epsilon'_2+\epsilon'_3) & 0\\ \frac{1}{2}(-\epsilon'_2+\epsilon'_3) & \frac{1}{2}(\epsilon'_2+\epsilon'_3) & 0\\ 0 & 0 & \epsilon'_1\end{pmatrix}$$

By using transformations above magnetocrystalline anisotropy for (110) films can be written as following

$$E_{mc}=K_1[\frac{1}{2}{\alpha'_1}^2(-\alpha'_2+\alpha'_3)^2+\frac{1}{2}{\alpha'_1}^2(\alpha'_2+\alpha'_3)^2+\frac{1}{4}(-\alpha'_2+\alpha'_3)^2(\alpha'_2+\alpha'_3)^2] \qquad (6.10)$$

where the α'_i $(i=1,2,3)$ are the directional cosines with respect to primed coordinate system. Inserting direction of cosines into the Eq. 6.10 yields the magnetocrystalline anisotropy energy density for (110) films as a function of polar coordinates;

$$\begin{aligned}E^{(110)}_{mc}(\Theta,\Phi) =&K_1[\frac{1}{4}\sin^4\Theta\sin^4\Phi+\frac{1}{4}\cos^4\Theta+\sin^4\Theta\sin^2\Phi\cos^2\Phi\\ &-\frac{1}{2}\sin^2\Theta\cos^2\Theta\sin^2\Phi+\sin^2\Theta\cos^2\Theta\cos^2\Phi]\end{aligned} \qquad (6.11)$$

Inserting transformed strain and direction of cosines expressions into Eq. 6.4, the magnetoelastic anisotropy energy density of (110) films with crystallographic coordinates as shown in Fig. 6.2 can be written as

$$\begin{aligned}E_{me} =&{\alpha'_1}^2B_1\epsilon'_1+\frac{1}{2}{\alpha'_2}^2B_1\epsilon'_2+\frac{1}{2}{\alpha'_3}^2B_1\epsilon'_2+\frac{1}{2}{\alpha'_2}^2B_2\epsilon'_2-\frac{1}{2}{\alpha'_3}^2B_2\epsilon'_2\\ &+\frac{1}{2}{\alpha'_2}^2B_1\epsilon'_3+\frac{1}{2}{\alpha'_3}^2B_1\epsilon'_3-\frac{1}{2}{\alpha'_2}^2B_2\epsilon'_3+\frac{1}{2}{\alpha'_3}^2B_2\epsilon'_3\end{aligned} \qquad (6.12)$$

and in terms of polar coordinates it follows;

$$\begin{aligned}E^{(110)}_{me}(\Theta,\Phi) =&\frac{1}{2}B_1\epsilon'_2\cos^2\Theta-\frac{1}{2}B_2\epsilon'_2\cos^2\Theta+\frac{1}{2}B_1\epsilon'_3\cos^2\Theta+\frac{1}{2}B_2\epsilon'_3\cos^2\Theta\\ &+B_1\epsilon'_1\cos^2\Phi\sin^2\Theta+\frac{1}{2}B_1\epsilon'_2\sin^2\Theta\sin^2\Phi+\frac{1}{2}B_2\epsilon'_2\sin^2\Theta\sin^2\Phi\\ &+\frac{1}{2}B_1\epsilon'_3\sin^2\Theta\sin^2\Phi-\frac{1}{2}B_2\epsilon'_3\sin^2\Theta\sin^2\Phi\end{aligned} \qquad (6.13)$$

Setting $\Theta=\frac{\pi}{2}$ in the Eq. 6.13 and using the fact that strain is isotropic in the plane, $\epsilon'_1=\epsilon'_2=\epsilon'_0$, the magnetoelastic anisotropy energy density in the (110) plane (in-plane anisotropy)is given by

$$\begin{aligned} E_{me}^{in-pl.}(\Theta=\pi/2,\Phi) =& B_1\acute{\epsilon}_0\cos^2\Phi+\frac{1}{2}B_1\acute{\epsilon}_0\sin^2\Phi+\frac{1}{2}B_2\acute{\epsilon}_0\sin^2\Phi \\ &+\frac{1}{2}B_1\acute{\epsilon}_3\sin^2\Phi-\frac{1}{2}B_2\acute{\epsilon}_3\sin^2\Phi \end{aligned} \tag{6.14}$$

where $\acute{\epsilon}_0$ and $\acute{\epsilon}_3$ are the in-plane and out-of-plane strains, respectively. It is immediately seen from Eq. 6.14 that magnetoelastic coupling leads to uniaxial anisotropy in the plane of (110) films unless $B_1 = B_2$. And the strength of the anisotropy depends on the relative magnitudes of B_1 and B_2, as the difference between the magnitudes increases the uniaxial anisotropy becomes stronger, while the direction of the easy and hard axes are determined by the mutual signs of the magnetoelastic coefficients, B_1, B_2. We should recall that magnetoelastic energy was isotropic for the case of (001) films. The out-of-plane anisotropy can be traced as setting $\Phi = 0$ in the Eq. 6.13, which corresponds to polar dependence of the magnetization between [001] and [110] axes. According to Eq. 6.15 strain also induces uniaxial anisotropy in the $(1\bar{1}0)$ surface providing that $B_1 \neq B_2$.

$$\begin{aligned} E_{me}^{out-pl.}(\Phi=0,\Theta) =& \frac{1}{2}B_1\acute{\epsilon}_0\cos^2\Theta-\frac{1}{2}B_2\acute{\epsilon}_0\cos^2\Theta+\frac{1}{2}B_1\acute{\epsilon}_3\cos^2\Theta \\ &+\frac{1}{2}B_2\acute{\epsilon}_3\cos^2\Theta+B_1\acute{\epsilon}_0\sin^2\Theta \end{aligned} \tag{6.15}$$

After all, the effective magnetic anisotropy energy including crystalline, magnetoelastic and the shape anisotropies is given as;

$$\begin{aligned} E_{ani}^{(110)}(\Theta,\Phi) =& K_1[\frac{1}{4}\sin^4\Theta\sin^4\Phi+\frac{1}{4}\cos^4\Theta+\sin^4\Theta\sin^2\Phi\cos^2\Phi \\ &-\frac{1}{2}\sin^2\Theta\cos^2\Theta\sin^2\Phi+\sin^2\Theta\cos^2\Theta\cos^2\Phi] \\ &+\frac{1}{2}B_1\acute{\epsilon}_2\cos^2\Theta-\frac{1}{2}B_2\acute{\epsilon}_2\cos^2\Theta+\frac{1}{2}B_1\acute{\epsilon}_3\cos^2\Theta+\frac{1}{2}B_2\acute{\epsilon}_3\cos^2\Theta \\ &+B_1\acute{\epsilon}_1\cos^2\Phi\sin^2\Theta+\frac{1}{2}B_1\acute{\epsilon}_2\sin^2\Theta\sin^2\Phi+\frac{1}{2}B_2\acute{\epsilon}_2\sin^2\Theta\sin^2\Phi \\ &+\frac{1}{2}B_1\acute{\epsilon}_3\sin^2\Theta\sin^2\Phi-\frac{1}{2}B_2\acute{\epsilon}_3\sin^2\Theta\sin^2\Phi+\frac{1}{2}\mu_0M_s^2\cos^2\Theta \end{aligned} \tag{6.16}$$

6.3 (111) films

The (111) orientation also requires appropriate tensor transformation, which is performed similar to that of (110) films. The (111) film directions, $\acute{x}$,$\acute{y}$,$\acute{z}$, are expressed in terms of crystal directions , x, y, z.

$$a_{ij}=\begin{pmatrix} -\frac{1}{\sqrt{2}} & \frac{1}{\sqrt{2}} & 0 \\ -\frac{1}{\sqrt{6}} & -\frac{1}{\sqrt{6}} & \sqrt{\frac{2}{3}} \\ \frac{1}{\sqrt{3}} & \frac{1}{\sqrt{3}} & \frac{1}{\sqrt{3}} \end{pmatrix} \tag{6.17}$$

	x	y	z
$\acute{x}$	-$\frac{1}{\sqrt{2}}$	$\frac{1}{\sqrt{2}}$	0
$\acute{y}$	-$\frac{1}{\sqrt{6}}$	-$\frac{1}{\sqrt{6}}$	$\sqrt{\frac{2}{3}}$
$\acute{z}$	$\frac{1}{\sqrt{3}}$	$\frac{1}{\sqrt{3}}$	$\frac{1}{\sqrt{3}}$

from which the direction cosine and the strain relations follows as

$$\begin{aligned}
\alpha_1 &= -\frac{1}{\sqrt{2}}\acute{\alpha}_1 - \frac{1}{\sqrt{6}}\acute{\alpha}_2 + \frac{1}{\sqrt{3}}\acute{\alpha}_3 \\
\alpha_2 &= \frac{1}{\sqrt{2}}\acute{\alpha}_1 - \frac{1}{\sqrt{6}}\acute{\alpha}_2 + \frac{1}{\sqrt{3}}\acute{\alpha}_3 \\
\alpha_3 &= \sqrt{\frac{2}{3}}\acute{\alpha}_2 + \frac{1}{\sqrt{3}}\acute{\alpha}_3
\end{aligned}$$

$$\epsilon_{ij} = \begin{pmatrix}
\frac{1}{2}\acute{\epsilon}_1 + \frac{1}{6}\acute{\epsilon}_2 + \frac{1}{3}\acute{\epsilon}_3 & -\frac{1}{2}\acute{\epsilon}_1 + \frac{1}{6}\acute{\epsilon}_2 + \frac{1}{3}\acute{\epsilon}_3 & \frac{1}{3}(-\acute{\epsilon}_2 + \acute{\epsilon}_3) \\
-\frac{1}{2}\acute{\epsilon}_1 + \frac{1}{6}\acute{\epsilon}_2 + \frac{1}{3}\acute{\epsilon}_3 & \frac{1}{2}\acute{\epsilon}_1 + \frac{1}{6}\acute{\epsilon}_2 + \frac{1}{3}\acute{\epsilon}_3 & \frac{1}{3}(-\acute{\epsilon}_2 + \acute{\epsilon}_3) \\
\frac{1}{3}(-\acute{\epsilon}_2 + \acute{\epsilon}_3) & \frac{1}{3}(-\acute{\epsilon}_2 + \acute{\epsilon}_3) & \frac{2}{3}\acute{\epsilon}_1 + \frac{1}{3}\acute{\epsilon}_3
\end{pmatrix}$$

and the magnetocrystalline anisotropy energy density for (110) films as a function of polar coordinates is written as;

$$\begin{aligned}
E_{mc}^{(111)}(\Theta,\Phi) =&K_1[\left(\frac{\cos\Theta}{3} + \sqrt{\frac{2}{3}}\sin\Theta\sin\Phi\right)^2 \left(\frac{\cos\Theta}{\sqrt{3}} - \frac{\cos\Phi\sin\Theta}{\sqrt{2}} - \frac{\sin\Theta\sin\Phi}{\sqrt{6}}\right)^2 \\
&+ \left(\frac{\cos\Theta}{\sqrt{3}} + \sqrt{\frac{2}{3}}\sin\Theta\sin\Phi\right)^2 + \left(\frac{\cos\Theta}{\sqrt{3}} + \frac{\cos\Phi\sin\Theta}{\sqrt{2}} - \frac{\sin\Theta\sin\Phi}{\sqrt{6}}\right)^2 \\
&+ \left(\frac{\cos\Theta}{\sqrt{3}} - \frac{\cos\Phi\sin\Theta}{\sqrt{2}} - \frac{\sin\Theta\sin\Phi}{\sqrt{6}}\right)^2 \\
&+ \left(\frac{\cos\Theta}{\sqrt{3}} + \frac{\cos\Phi\sin\Theta}{\sqrt{2}} - \frac{\sin\Theta\sin(\Phi)}{\sqrt{6}}\right)^2]
\end{aligned} \tag{6.18}$$

and magnetoelastic anisotropy energy density in (111) films follows;

$$
\begin{aligned}
E_{me}^{(111)}(\Theta,\Phi) =& B_1[-\frac{1}{3}\epsilon_3\left(\frac{\cos\Theta}{\sqrt{3}}+\sqrt{\frac{2}{3}}\sin\Theta\sin\Phi\right)^2\\
&-\frac{1}{3}\epsilon_3\left(\frac{\cos\Theta}{\sqrt{3}}-\frac{\cos\Phi\sin\Theta}{\sqrt{2}}-\frac{\sin\Theta\sin\Phi}{\sqrt{6}}\right)^2\\
&-\frac{1}{3}\epsilon_3\left(\frac{\cos\Theta}{\sqrt{3}}+\frac{\cos\Phi\sin\Theta}{\sqrt{2}}-\frac{\sin\Theta\sin\Phi}{\sqrt{6}}\right)^2]\\
&+B_2[\frac{4}{3}\epsilon_3\left(\frac{\cos\Theta}{\sqrt{3}}+\sqrt{\frac{2}{3}}\sin\Theta\sin\Phi\right)\left(\frac{\cos\Theta}{\sqrt{3}}-\frac{\cos\Phi\sin\Theta}{\sqrt{2}}-\frac{\sin\Theta\sin\Phi}{\sqrt{6}}\right)\\
&+\frac{4}{3}\epsilon_3\left(\frac{\cos\Theta}{\sqrt{3}}+\sqrt{\frac{2}{3}}\sin\Theta\sin\Phi\right)\left(\frac{\cos\Theta}{\sqrt{3}}+\frac{\cos\Phi\sin\Theta}{\sqrt{2}}-\frac{\sin\Theta\sin\Phi}{\sqrt{6}}\right)\\
&+\frac{4}{3}\epsilon_3\left(\frac{\cos\Theta}{\sqrt{3}}-\frac{\cos\Phi\sin\Theta}{\sqrt{2}}-\frac{\sin\Theta\sin\Phi}{\sqrt{6}}\right)\\
&\left(\frac{\cos\Theta}{\sqrt{3}}+\frac{\cos\Phi\sin\Theta}{\sqrt{2}}-\frac{\sin\Theta\sin\Phi}{\sqrt{6}}\right)]
\end{aligned}
\tag{6.19}
$$

Acknowledgement

I would like to express my sincere gratitude to numerous people whose contribution and support realized this thesis. First of all, I am grateful for Prof. Hilbert von Löhneysen who welcomed me to the IFP and gave me the opportunity to work within his group. I would like to thank Prof. Wulf Wulfhekel for acting as co-referee of this work. I am very grateful for my direct supervisor, Dr. Dirk Fuchs, who guided me throughout this work. I am indebted for his support and interest in my work as well as the helpful discussions. I am finally grateful for reading and correcting my thesis within a very short period. I am also thankful to Dr. Rudolf Schneider, who reviewed my thesis. My special thanks to Dr. Stefan Schuppler for the fruitful discussions. I learned great deal of physics from him. I am grateful for the collaboration with Fadi El Hallak, who performed the torque magnetometry measurements. I am thankful for my colleagues and friends in the IFP, Wanyin Cui, Frederic Hardy, Michael Merz, Markus Wissinger, Stefan Uebe, Andrea Assmann, Roland Hott, Andre Beck, Sandra Drotziger. I would like to thank to Edith Maass for her help in the administrative issues. I can not forget my lovely friends Fadi El Hallak, Jules Mikhael, Pegor Aynajian, Pedro Vidal with whom I shared my happiness and sadness. On a personal level, I would like to thank my parents for their support and the motivation. Finally, I will thank my beloved girlfriend Deniz Dag, who enriched my life and encouraged me every time I needed.

Bibliography

[1] M. Imada, A. Fujimori, and Y. Tokura, Rev. Mod. Phys. **70**, 1039 (1998).

[2] S. Barman and D. Sarma, Phys. Rev. B **49**, 13979 (1994).

[3] M. Abbate, R. Potze, G. Sawatzky, and A. Fujimori, Phys. Rev. B **49**, 7210 (1994).

[4] T. Saitoh et al., Phys. Rev. B **55**, 4257 (1997).

[5] M. W. Haverkort et al., Phys. Rev. Lett. **97**, 176405 (2006).

[6] A. Podlesnyak et al., Phys. Rev. Lett. **97**, 247208 (2006).

[7] R. Klie et al., Phys. Rev. Lett. **99**, 047203 (2007).

[8] M. A. Korotin et al., Phys. Rev. B **54**, 5309 (1996).

[9] C. Zobel et al., Phys. Rev. B **66**, 020402(R) (2002).

[10] S. K. Pandey et al., Phys. Rev. B **77**, 045123 (2008).

[11] P. M. Raccah and J. B. Goodenough, Phys. Rev. **155**, 932 (1967).

[12] L. Craco and E. Muller-Hartmann, Phys. Rev. B **77**, 045130 (2008).

[13] M. Abbate et al., Phys. Rev. B **47**, 16124 (1993).

[14] D. Sherman, *Advances in Physical Geochemistry*, Springer, Berlin, 1988.

[15] D. Fuchs et al., Phys. Rev. B **75**, 144402 (2007).

[16] S. Zhou et al., 172407 **76**, 045130 (2007).

[17] Menyuk, K. Dwight, and P. M. Raccah, J. Phys. Chem. Solids **28**, 549 (1967).

[18] J. Q. Yan, J. S. Zhou, and J. B. Goodenough, Phys. Rev. B **70**, 014402 (2004).

[19] J. Androukalis, N. Katsarakis, and J. Giapintzakis, Phys. Rev. B **64**, 174401 (2001).

[20] A. Harada et al., Phys. Rev. B **75**, 184426 (2007).

[21] S. Zhou et al., Phys. Rev. B **76**, 172407 (2007).

[22] A. Herklotz, A. D. Rata, L. Schultz, and K. Dörr, Phys. Rev. B **79**, 092409 (2009).

[23] D. Fuchs et al., Phys. Rev. B **77**, 014434 (2008).

[24] D. Fuchs et al., Phys. Rev. B **79**, 024424 (2009).

[25] V. V. Mehta et al., eScholarship Repository, University of California **LBNL-1528E** (2009).

[26] S. Park et al., Appl. Phys. Lett. **95**, 072508 (2009).

[27] D. G. Schlom et al., Annu. Rev. Mater. Res. **37**, 589 (2007).

[28] Q. Gan, R. A. Rao, C. B. Eom, J. L. Garrett, and M. Lee, Appl. Phys. Lett. **72**, 978 (1998).

[29] J. H. Haeni et al., Appl. Phys. Lett. , 758 (2004).

[30] C. J. Fennie and K. M. Rabe, Phys. Rev. Lett. **97**, 267602 (2006).

[31] C. J. Fennie and K. M. Rabe, Phys. Rev. Lett. **97**, 267602 (2006).

[32] N. C. Yeh et al., J. Appl. Phys. **81**, 5499 (1997).

[33] M. Rajesvari, Appl. Phys. Lett. **73**, 2672 (1998).

[34] N.K.Todd, N. Mathur, and M. Blamire, J. Appl. Phys. **89**, 6970 (2001).

[35] J. Coey, M. Viret, and S. von Molnar, Advances in physics **48**, 167 (1999).

[36] H. Ohno et al., Appl. Phys. Lett. **69**, 363 (1996).

[37] K. Steenbeck and R. Hiergeist, Appl. Phys. Lett. **75**, 1778 (1999).

[38] S. W. Cheong, T. Siegrist, Y. Suzuki, H. Y. Hwang, and R. B. van Dover, J. Appl. Phys. **83**, 7064 (1998).

[39] J. Lodder, R. Jansen, M. Mathews, and M. Postma, Appl. Phys. Lett. **87**, 242507 (2005).

[40] P. L. Trouilloud and P. Lecoeur, J. Appl. Phys. **82**, 3934 (1997).

[41] M. El-Hilo, S. H. Uren, K. O'Grady, and J. Popplewell, IEEE Trans. Mag. **26**, 244 (1990).

[42] S. T. Chui, J. Magn. Magn. Mater. **217**, 120 (2000).

[43] M. Sirena, L. B. Steren, and J. Guimpel, Phys. Rev. B **64**, 104409 (2001).

[44] G. Bayreuther, P. Bruno, G. Lugert, and C. Turtur, Phys. Rev. B **40**, 7399 (1989).

[45] S. Boukari, R. Allenspach, and A. Bischof, Phys. Rev. B **63**, 180402(R) (2001).

[46] N. D. Rizzo, T. J. Silva, and A. B. Kos, Phys. Rev. Lett. **83**, 4876 (1999).

[47] L. C. Sampaio, M. P. de Albuquerque, and F. S. de Menezes, Phys. Rev. B **54**, 6465 (1996).

[48] R. J. Cava et al., Phys. Rev. Lett. **58**, 1676 (1997).

[49] R. Helmolt, J. Wecker, B. Holzapfel, L. Schultz, and K. Samwer, Phys. Rev. Lett. **71**, 2331 (1993).

[50] A. P. Ramirez, J.Phys: Condens. Matter **9**, 8171 (1992).

[51] R. E. Cohen, Nature **358**, 136 (1993).

[52] V. M. Goldschmidt, Naturewissenschaften **14**, 477 (1926).

[53] M. Imada, A. Fujimori, and Y. Takure, Rev. Mod. Phys. **70**, 1039 (1998).

[54] G. Thornton, B. C. Tofield, and W. Hewat, J. Solid State Chem. **61**, 301 (1986).

[55] S. Blundell, *Magnetism in condensed matter*, Oxford University Press, Oxford, 2001.

[56] J. Q. Yan, J. S. Zhou, , and J. B. Goodenough, Phys. Rev. B **69**, 134409 (2003).

[57] D. Fuchs, P. Schweiss, P. Adelmann, T. Schwarz, and R. Schneider, Phys. Rev. B **72**, 014466 (2005).

[58] J. S. Zhou, J. Q. Yan, and J. B. Goodenough, Phys. Rev. B **71**, 220103(R) (2005).

[59] W. C. Koehler and E. O. Wollan, J. Phys. Chem. Solids **2**, 100 (1957).

[60] G. Thornton, B. C. Tofield, and A. W. Hewat, J. Solid State Chem. **61**, 301 (1987).

[61] T. Mizokawa and A. Fujimori, Phys. Rev. B **51**, 12880 (1995).

[62] J. B. Goodenough, Phys. Rev. **100**, 564 (1953).

[63] J. Kanamori, J. Phys. Chem. Solids **10**, 87 (1959).

[64] V. Eyert, *The Augment Spherical Wave Method: A Comprehensive treatment, Lecture Notes in Physics vol. 719*, Springer, Heidelberg, 2007.

[65] H. Brooks, Phys. Rev. **58**, 909 (1940).

[66] C. Kittel, Rev. Mod. Phys. **21**, 541 (1949).

[67] R. Wu, *First Principles determination of magnetic anisotropy and magnetostriction in transition metal alloys*, Springer, Berlin, 2001.

[68] T. Burkert, O. Eriksson, and J. M. Wills, Phys. Rev. Lett. **75**, 2871 (1995).

[69] D. Dander, Rep. Prog. Phys. **62**, 809 (1999).

[70] J. F. Nye, *Physical properties of crystals*, Oxford University Press, Oxford, 1985.

[71] L. Neèl, Physique Rad. **15**, 225 (1954).

[72] R. Chantrell, A. Lyberatos, M. El-Hilo, and K. O'Grady, J. Appl. Phys. **76**, 6407 (1994).

[73] R. V. Chamberlin and F. Holtzberg, Phys. Rev. Lett. **67**, 1606 (1991).

[74] G. Sinha, R. Chatterjee, M. Uehara, and A. K. Majumdar, J. Magn. Magn. Mater. **164**, 345 (1996).

[75] M. Ulrich, J. Garcia-Otero, J. Rivas, and A. Bunde, Phys. Rev. B **67**, 024416 (2003).

[76] W. Gotze and L. Sjoogren, Rep. Prog. Phys. **55**, 241 (1992).

[77] L. Cipelli and L. Ramos, J. Phys: Condens. Matter. **17**, R253 (2005).

[78] R. V. Chamberlin, G. Mozurkewich, and R. Orbach, Phys. Rev. Lett. **52**, 867 (1984).

[79] E. Fatuzzo, Phys. Rev. **127**, 1999 (1969).

[80] H. Xi, G. Kai-Zhong, J. Ouyang, Y. Shi, and Y. Yang, J. Phys.: Condens. Matter **20**, 295220 (2008).

[81] M. Labrune, S. Andrieu, F. Rio, and P. Bernstein, J. Magn. Magn. Mater. **80**, 211 (1989).

[82] M. El-Hilo, K. O'Grady, and R. Chantrell, J. Magn. Magn. Mater. **109**, 1992 (L164-L168).

[83] T. G. S. Pierre, N. T. Gorham, P. D. Allen, J. L. Costa-Ktamer, and K. V. Rao, Phys. Rev. B **65**, 024436 (2001).

[84] N. T. G. andR. C. Woodward, T. G. S. Pierre, B. D. Terris, and S. Sun, J. Mag. Mag. Mater. **295**, 174 (2005).

[85] J.-L. Tsai and C.-J. Hsu, J. Phys.: Condens. Matter **18**, 7729 (2006).

[86] G. Bottoni, D. Candolfo, and A. Cecchetti, J. Mag. Mag. Mater. **272**, 2271 (2004).

[87] A. N. Petrov, V. A. Cherepanov, E. M. Novitskii, and V. M. Zhukovitskii, Russian J. Phys. Chem. **58**, 1619 (1984).

[88] T. Schwarz, Kritisches Verhalten dünner ferromagnetischer $La_{0.7}Sr_{0.3}CoO_3$ Schichten **Ph.D thesis**, Fakultät für Physik der Universität Karlsruhe (TH) (2007).

[89] S. Goriglio, N. Stucki, and J. M. Friscone, Appl. Phys. Lett. **90**, 202905 (2007).

[90] K. Wiesauer and G. Sringholz, Phys. Rev. B **69**, 245313 (2004).

[91] P. communication.

[92] G. Fehringer, S. Janes, M. Wildersohn, and R. Clasen, J. Eur. Ceram. Soc. **24**, 705 (2004).

[93] J. Kerr, Rep. Brit. Ass. **85**, 1492 (1876).

[94] J. Kerr, Phil. Mag. **3**, 321 (1877).

[95] M. Faraday, Phil.Trans. Soc. **1**, 14338.

[96] W. Ann., Phys. Rev. Lett. **67**, 359 (1899).

[97] A. Cotton and H. Muoton, Compt. Rend. Acad. Sci. **145**, 229 (1907).

[98] H. Hulme, Proc. R. Soc. London, Ser. A **135**, 237 (1932).

[99] P. N. Argyres, Phys. Rev. **97**, 334 (1955).

[100] H. S. Bennett and E. A. Stern, Phys. Rev. **137**, A448 (1965).

[101] B. R. Cooper, Phys. Rev. **139**, A1505 (1965).

[102] J. L. Erskine and E. A. Stern, Phys. Rev. B **8**, 1239 (1973).

[103] R. P. Hunt, J. Appl. Phys. **38**, 1652 (1967).

[104] Y. J. Yang and M. R. Scheinfein, J. Appl. Phys. **74**, 6810 (1993).

[105] J. Z. andE. R. Mook, C. Liu, and S. Bader, J. Appl. Phys. **68**, 4203 (1990).

[106] W. Reim and J. Schönes, *Ferromagnetic Materials*, volume 5, North Holland, Amsterdam, 1990.

[107] C. Y. You and S. C. Shin, J. Appl. Phys. **84**, 541 (1998).

[108] J. A. C. Bland and B. Heindrich, *Ultrathin Magnetic Structures*, volume 1, Springer Verlag, 1994.

[109] K. Sato, Jap. J. Appl. Phys. **20**, 2403 (1981).

[110] K. Sato, Jpn. J. Appl. Phys. **32**, 989 (1992).

[111] S. N. Jasperson and S. E. Schnatterly, Rev. Sci. Instrum. **40**, 761 (1969).

[112] S. N. Jasperson, D. K. Burge, and R. C. O'Hsndley, Surface Sci. **37**, 548 (1973).

[113] W. B. Zeper, Thesis **University of Twente**.

[114] R. M. A. Azzam, *Ellipsometric and Polarized light*, North Holland, Amsterdam, 1977.

[115] R. Schaefer, *Handbook of Magnetism*, volume 3, Wiley, 2007.

[116] J. Giergiel and J. Kirschner, Rev. Sci. Instrum. **67**, 2937 (1996).

[117] M. Heidcamp and J. L. Erskine, Rev. Sci. Instrum. **71**, 3141 (2000).

[118] G. Meyer, T. Crecelius, G. Kaindl, and A. Bauer, J. Magn. Magn. Mater. **240**, 76 (2002).

[119] V. V. Protopopov, S. Lee, Y. Kwon, S. Cho, and H. Kim, Rev. Sci. Instrum. **77**, 73104 (2006).

[120] J. McCord, H. Brendel, A. Hubert, and S. Parkin, J. Magn. Magn. Mater. **148**, 244 (1995).

[121] A. Huber and R. Schaefer, *Magnetic Domains*, Springer.

[122] D. Treves, J. Appl. Phys. **32**, 358 (1961).

[123] A. Honda and K. Shirae, IEEE Trans. Magn. **17**, 3096 (1981).

[124] K. Shirae and K. Sugiyama, J. Appl. Phys. **53**, 8380 (1982).

[125] F. Schmidt, W. Rave, and A. Hubert, IEEE Trans. Magn. **21**, 1596 (1985).

[126] A. Smith and W. Goller, IEEE Trans. Magn. **26**, 1331 (1990).

[127] S. D. Bader and J. L. Erskine, *Magneto-optical effects in ultrathin magnetic structures(II)*, Spinger-Verlag, Berlin, 1994.

[128] W. J. M. de Jonge, P. J. H. Bloeman, and F. J. A. den Broeder, *Ultrathin magnetic structures (I)*, Spinger-Verlag, Berlin, 1994.

[129] M. T. Johnson, P. J. H. Bloeman, and F. J. A. den Broeder, Reports on Progress in Physics **59**, 1409 (1996).

[130] I. C. Infante, J. O. Osso, F. Sanchez, and J. Fontuber, Appl. Phys. Lett. **92**, 12508 (2008).

[131] K. Kniaek, P. Novak, and Z. Jirak, Phys. Rev. B **71**, 054420 (2005).

[132] P. Kozlenko et al., Phys. Rev. B **75**, 064422 (2007).

[133] M. Merz et al.

[134] S. Chikazumi, *Physics of magnetism*, Wiley, Newyork, 1964.

[135] L. Callegro and E. Pugin, Appl. Phys. Lett. **68**, 1279 (1995).

[136] J. Garshelis, J. Appl. Phys. **73**, 5629 (1993).

[137] M. J. Sablik et al., J. Appl. Phys. **74**, 480 (1993).

[138] S. Chikazumu, *Physics of Ferromagnetism*, Clarendon Press, Oxford, 1997.

[139] Y. Suzuki, H. Y. Hwang, S.-W. Cheong, T. Siegrist, and R. B. van Dover, J. Appl. Phys. **83**, 7064 (1998).

[140] F. Tsui, C. Smoak, T. K. Nath, and E. C. Eom, Appl. Phys. Lett. **76**, 2421 (1999).

[141] T. K. Nath, R. A. Rao, D. Lavric, and B. Eom, Appl. Phys. Lett. **74**, 1615 (1999).

[142] R. A. Rao, D. Lavric, T. K. Nath, and B. Eom, J. Appl. Phys. **85**, 4794 (1999).

[143] J. ODonnell, M. S. Rzchowski, J. N. Eckstein, and I. Bozobic, Appl. Phys. Lett. **72**, 1775 (1998).

[144] J.-L. Tsai and C.-J. Hsu, J. Phys.:Condes. Matter **18**, 7729 (2006).

[145] M. El-Hilo, K. O'Grady, R. Chantrell, and D. P. E. Dickson, J. Magn. Magn. Mater. **123**, 1993 (30-34).

[146] J. Mattsson, T. Jonsson, P. Nordblod, and P. Svandlindh, J. Magn. Magn. Mater. **168**, 269 (1997).

[147] G. Herzer, IEEE Trans. Magn. **26**, 1397 (1990).

[148] R. Street and J. C. Wooley, Proc. Phys. Soc. London, Sect. A **363**, 562 (1949).

[149] K. J. Lee and T. D. Lee, J. Appl. Phys. **85**, 5003 (1999).